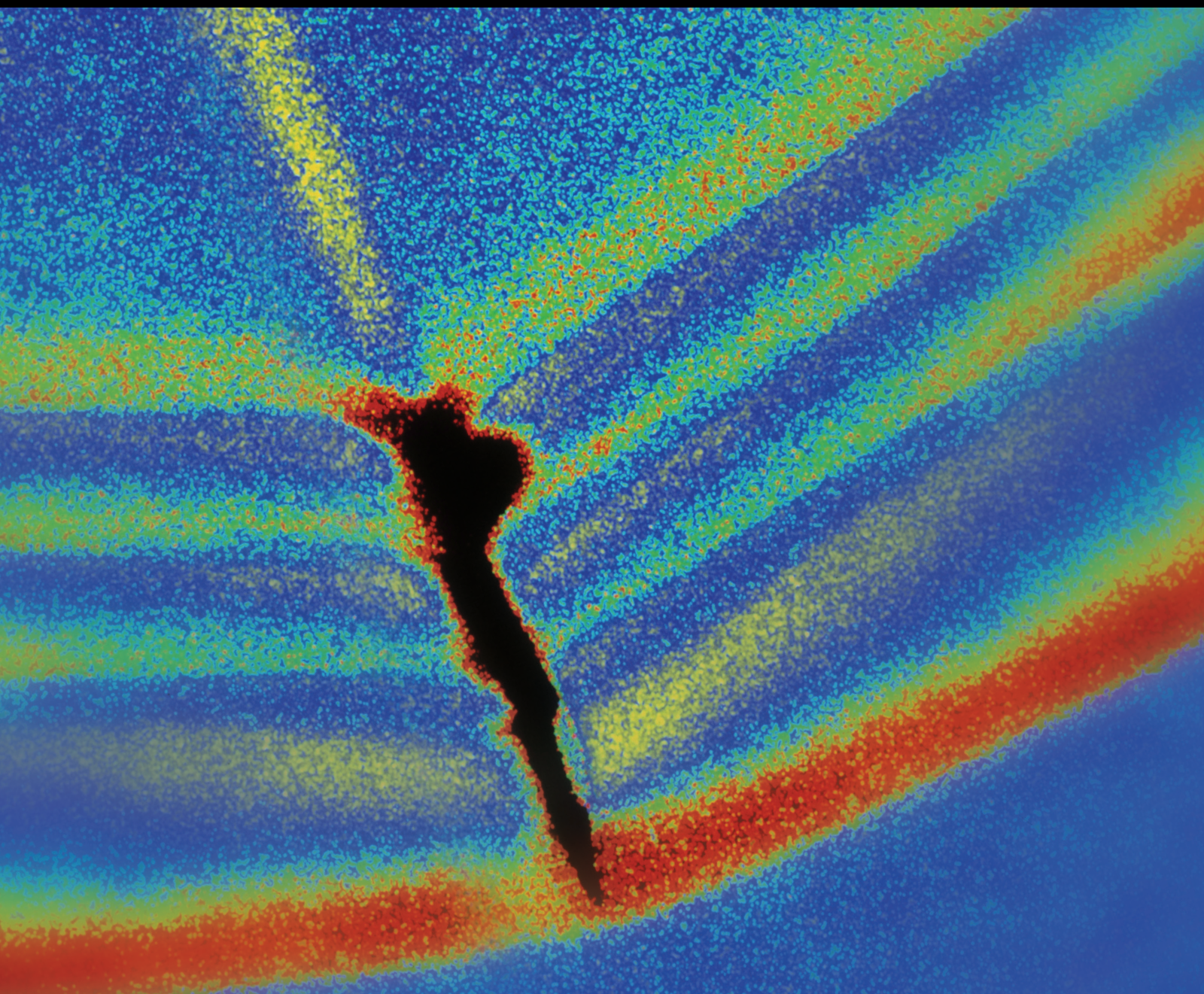


Shock and Vibration

Noncontact Measurements for Vibration-Based SHM and NDE

Lead Guest Editor: Piotr Kohut

Guest Editors: Alessandro Sabato, Elías López-Alba, Krzysztof Holak,
and Francisco A. Díaz





Noncontact Measurements for Vibration-Based SHM and NDE

Shock and Vibration

Noncontact Measurements for Vibration-Based SHM and NDE

Lead Guest Editor: Piotr Kohut

Guest Editors: Alessandro Sabato, Elías López-Alba,
Krzysztof Holak, and Francisco A. Díaz



Copyright © 2019 Hindawi. All rights reserved.

This is a special issue published in "Shock and Vibration." All articles are open access articles distributed under the Creative Commons Attribution License, which permits unrestricted use, distribution, and reproduction in any medium, provided the original work is properly cited.

Editorial Board

- Brij N. Agrawal, USA
Felix Albu, Romania
Marco Alfano, Italy
Sumeet S. Aphale, UK
Hassan Askari, Canada
Lutz Auersch, Germany
Matteo Aureli, USA
Mahmoud Bayat, USA
Marco Belloli, Italy
Giosuè Boscato, Italy
Francesco Braghin, Italy
RafaD Burdzik, Poland
Salvatore Caddemi, Italy
Ivo Caliò, Italy
Antonio Carcaterra, Italy
Dumitru I. Caruntu, USA
Cristina Castejón, Spain
Nicola Caterino, Italy
Gabriele Cazzulani, Italy
Noel Challamel, France
Athanasios Chasalevris, UK
Xavier Chiementin, France
Nawawi Chouw, New Zealand
Simone Cinquemani, Italy
Pedro A. Costa, Portugal
Alvaro Cunha, Portugal
Giorgio Dalpiaz, Italy
Farhang Daneshmand, Canada
Silvio L.T. de Souza, Brazil
Dario Di Maio, UK
Luigi Di Sarno, Italy
Longjun Dong, China
Lorenzo Dozio, Italy
Mohamed El Badaoui, France
Mohammad Elahinia, USA
Fiorenzo A. Fazzolari, UK
Matteo Filippi, Italy
Piotr Fol0ga, Poland
Paola Forte, Italy
Francesco Franco, Italy
Juan C. G. Prada, Spain
Pedro Galvín, Spain
Gianluca Gatti, Italy
Marco Gherlone, Italy
- Anindya Ghoshal, USA
Gilbert R. Gillich, Romania
Nere Gil-Negrete, Spain
Adam Glowacz, Poland
Itzhak Green, USA
Hassan Haddadpour, Iran
M. A. Hariri-Ardebili, USA
M.I. Herreros, Spain
Hamid Hosano, Japan
Reza Jazar, Australia
Sakdirat Kaewunruen, UK
Yuri S. Karinski, Israel
Jeong-Hoi Koo, USA
Georges Kouroussis, Belgium
Mickaël Lallart, France
Luca Landi, Italy
Marco Lepidi, Italy
Zhixiong Li, China
Manuel Lopez Aenlle, Spain
Nuno M. Maia, Portugal
Stefano Manzoni, Italy
Giuseppe Carlo Marano, Italy
Stefano Marchesiello, Italy
Francesco S. Marulo, Italy
Jean-Mathieu Mencik, France
Laurent Mevel, France
Fabio Minghini, Italy
Mahdi Mohammadpour, UK
Rui Moreira, Portugal
Emiliano Mucchi, Italy
Peter Múčka, Slovakia
Sara Muggiasca, Italy
Tony Murmu, UK
Pedro Museros, Spain
Roberto Nascimbene, Italy
Sundararajan Natarajan, India
Toshiaki Natsuki, Japan
Miguel Neves, Portugal
Nicola Nisticò, Italy
Roberto Palma, Spain
A. Papageorgiou, Greece
Francesco Pellicano, Italy
Paolo Pennacchi, Italy
Giuseppe Petrone, Italy
- Evgeny Petrov, UK
Giuseppe Piccardo, Italy
Antonina Pirrotta, Italy
Franck Poisson, France
Luca Pugi, Italy
Mohammad Rafiee, Canada
Carlo Rainieri, Italy
José J. Rangel-Magdaleno, Mexico
Didier Rémond, France
Francesco Ripamonti, Italy
Riccardo Rubini, Italy
Salvatore Russo, Italy
Giuseppe Ruta, Italy
Edoardo Sabbioni, Italy
Filippo Santucci de Magistris, Italy
Onome E. Scott-Emuakpor, USA
Roger Serra, France
Chengzhi Shi, USA
Vadim V. Silberschmidt, UK
Kumar V. Singh, USA
Jean-Jacques Sinou, France
Isabelle Sochet, France
Alba Sofi, Italy
Jussi Sopanen, Finland
Stefano Sorace, Italy
Andrea Spaggiari, Italy
Shuaishuai Sun, Australia
Chao Tao, China
Marco Tarabini, Italy
Gloria Terenzi, Italy
Mario Terzo, Italy
Huu-Tai Thai, Australia
Marc Thomas, Canada
Hamid Toopchi-Nezhad, Iran
Carlo Trigona, Italy
Federica Tubino, Italy
Nerio Tullini, Italy
Angelo Marcelo Tusset, Brazil
Jens Twiefel, Germany
Filippo Ubertini, Italy
Marcello Vanali, Italy
F. Viadero, Spain
M. Ahmer Wadee, UK
Jörg Wallaschek, Germany



Matthew J. Whelan, USA
Agnieszka Wylomanska, Poland

Davood Younesian, Iran
Enrico Zappino, Italy

Radoslaw Zimroz, Poland

Contents

Noncontact Measurements for Vibration-Based SHM and NDE

Piotr Kohut , Alessandro Sabato , Elías López-Alba , Krzysztof Holak , and Francisco A. Diaz 
Editorial (2 pages), Article ID 4175619, Volume 2019 (2019)

Model Updating Method Based on Kriging Model for Structural Dynamics

Hong Yin , Jingjing Ma , Kangli Dong , Zhenrui Peng , Pan Cui , and Chenghao Yang 
Research Article (12 pages), Article ID 8086024, Volume 2019 (2019)

Effective Processing of Radar Data for Bridge Damage Detection

Tomasz Owerko  and Przemysław Kuras 
Research Article (13 pages), Article ID 2621092, Volume 2019 (2019)

Operational Deflection Shape Extraction from Broadband Events of an Aircraft Component Using 3D-DIC in Magnified Images

Ángel J. Molina-Viedma , Elías López-Alba, Luis Felipe-Sesé , and Francisco A. Díaz 
Research Article (9 pages), Article ID 4039862, Volume 2019 (2019)

Rail Corrugation Detection of High-Speed Railway Using Wheel Dynamic Responses

Jianbo Li  and Hongmei Shi 
Research Article (12 pages), Article ID 2695647, Volume 2019 (2019)

Seismic Resistance and Displacement Mechanism of the Concrete Footing

Abdoullah Namdar  and Yun Dong 
Research Article (9 pages), Article ID 5498505, Volume 2019 (2019)

Estimation of Cement Asphalt Mortar Disengagement Degree Using Vehicle Dynamic Response

Hui Shi , Liqiang Zhu, Hongmei Shi , and Zujun Yu
Research Article (11 pages), Article ID 4281514, Volume 2019 (2019)

Visual Identity-Based Earthquake Ground Displacement Testing Method

Chen Su, Zhao Sicheng, Dai Zhijun , Li Xiaojun , and Zhou Yue
Research Article (10 pages), Article ID 2585423, Volume 2019 (2019)

Editorial

Noncontact Measurements for Vibration-Based SHM and NDE

Piotr Kohut ¹, **Alessandro Sabato** ², **Elías López-Alba** ³, **Krzysztof Holak** ¹,
and Francisco A. Diaz ³

¹AGH University of Science and Technology, Cracow, Poland

²University of Massachusetts, Lowell, MA, USA

³Universidad de Jaén, Jaén, Spain

Correspondence should be addressed to Piotr Kohut; pko@agh.edu.pl

Received 30 April 2019; Accepted 30 April 2019; Published 23 May 2019

Copyright © 2019 Piotr Kohut et al. This is an open access article distributed under the Creative Commons Attribution License, which permits unrestricted use, distribution, and reproduction in any medium, provided the original work is properly cited.

Noncontact technologies for measuring and analysing the dynamics of various engineering systems and employing structural health monitoring (SHM) and nondestructive evaluation (NDE) framework are becoming increasingly popular among the research community and the industry. A large number of experimental and modeling techniques have been developed and applied to monitor the structural response including vision- and radar-based approaches, model updating, structural self-excitation, numerical modelling, and soft computing methods. These approaches enable a straightforward assessment of the physical and dynamics condition of large-sized and real-world structural components. To accelerate the adoption of these new emerging applications, several important issues have been addressed such as deployment modalities, fusion, signal processing, as well as investigation in the theories, algorithms, and methods with emphasis on vibration analysis applications. In this special issue on noncontact vibration-based SHM and NDE, we have invited the following articles to address such issues.

In the first paper of this special issue, the combination of phase-based motion magnification and 3D-DIC has been employed to evaluate the modal behaviour of an aircraft cabin under random excitation. The study was focused on the passenger window area due to its significance to the structural integrity as a discontinuity of the peel. Operational deflection shapes at different resonances were characterised by magnifying a single resonance in the spectrum and then measuring with 3D-DIC. These measurements were validated with those obtained in forced normal mode tests.

The second paper proposes a computer vision-based method of displacement measurement for the field of earthquake engineering. The presented method makes use of

relative displacement data recorded by a vision sensor and numerical modeling for the absolute ground displacement estimation. The proposed system is capable of real-time ground deformation observation and provides valuable data for earthquake mechanics understanding.

The third paper presents the practical results of the evaluation of the data obtained by ground-based radar interferometer during measurements carried out on bridge structures. A comprehensive method of data analysis was proposed. The effective use of vehicles as a source of bridge excitation allowed to first develop a method for determining the damping parameters resistant to potentially occurring beating frequencies. As a result, it is possible to determine these subsets of data registered with radar, for which it is possible to assume compliance with linear systems.

The fourth paper investigates the Kriging model and updating strategy using frequency response function to the damage identification of a truss structure. To improve the Kriging model, new sample points are added according to mean square error criterion and the model is updated iteratively. Cuckoo algorithm is employed to optimize the parameters. The proposed method is applied to a plane truss model, and the results are compared with the second-order response surface model and the radial basis function model.

The fifth paper presents a numerical simulation of a concrete footing-soil foundation interaction under seismic conditions. Authors provide an analysis of displacement, stress and strain, and seismic acceleration load response at the base of the concrete footing. The results show how the height of embedded footing affects displacements of the concrete footing, strain energy, and stress paths.

The sixth paper addresses the possibility to use changes recorded in the dynamic response of a cement asphalt mortar track to evaluate the degree of disengagement of the system. The method hereby described relies on an improved genetic algorithm (i.e., Mortar Disengagement Degree Estimation Algorithm). The proposed method is compared with traditional genetic algorithms for validating its robustness under different operational conditions.

The last paper presents a novel method for detection of rail corrugation wavelength and depth. An ensemble empirical mode decomposition (EEMD) is employed to estimate the wavelength, and a support vector machine (SVM) is applied for depth classification based on bispectrum features extracted from the vibration signal. The numerical simulation is carried out to assess the accuracy of the method.

Hoping the issue findings are of interest for research scientists and technical community readers, we wish a fruitful reading.

Conflicts of Interest

The editors declare that they have no conflicts of interest.

Acknowledgments

We would like to express our deepest appreciation to all authors for their valuable contribution and the reviewers for their thorough assessment and constructive review comments. We express our sincere thanks to the Editorial Board of *Shock and Vibration* and the Editorial Team for their approval on this topic, guidance and continuous support in successful publication of this special issue. The Lead Guest Editor would like to express his gratitude to the Guest Editors for their efforts and invaluable cooperation.

Piotr Kohut
Alessandro Sabato
Eliás López-Alba
Krzysztof Holak
Francisco A. Díaz

Research Article

Model Updating Method Based on Kriging Model for Structural Dynamics

Hong Yin , Jingjing Ma , Kangli Dong , Zhenrui Peng , Pan Cui ,
and Chenghao Yang 

School of Mechatronic Engineering, Lanzhou Jiaotong University, Lanzhou 730070, China

Correspondence should be addressed to Zhenrui Peng; pengzr@mail.lzjtu.cn

Received 2 January 2019; Revised 12 March 2019; Accepted 9 April 2019; Published 23 April 2019

Guest Editor: Piotr Kohut

Copyright © 2019 Hong Yin et al. This is an open access article distributed under the Creative Commons Attribution License, which permits unrestricted use, distribution, and reproduction in any medium, provided the original work is properly cited.

Model updating in structural dynamics has attracted much attention in recent decades. And high computational cost is frequently encountered during model updating. Surrogate model has attracted considerable attention for saving computational cost in finite element model updating (FEMU). In this study, a model updating method using frequency response function (FRF) based on Kriging model is proposed. The optimal excitation point is selected by using modal participation criterion. Initial sample points are chosen via design of experiment (DOE), and Kriging model is built using the corresponding acceleration frequency response functions. Then, Kriging model is improved via new sample points using mean square error (MSE) criterion and is used to replace the finite element model to participate in optimization. Cuckoo algorithm is used to obtain the updating parameters, where the objective function with the minimum frequency response deviation is constructed. And the proposed method is applied to a plane truss model FEMU, and the results are compared with those by the second-order response surface model (RSM) and the radial basis function model (RBF). The analysis results showed that the proposed method has good accuracy and high computational efficiency; errors of updating parameters are less than 0.2%; damage identification is with high precision. After updating, the curves of real and imaginary parts of acceleration FRF are in good agreement with the real ones.

1. Introduction

The accurate finite element model (FEM) is the basis of reflecting structural dynamics characteristics and guiding the optimization design of the structure. However, due to the modelling error and other uncertain factors, there is always a certain discrepancy between the FEM and the accurate model. Difference always exists between the mathematical model and experimentally measured one. Therefore, it is a general practice to update the theoretical model by using experimental measurements in order to obtain a more accurate model. Finite element model updating (FEMU) can be defined as the process of tuning a FEM to minimize the discrepancy between the measured and computed responses of the structure [1]. FEMU has attracted significant attention from the structural engineering community because of its applications in structural dynamics [2]. The current mainstream FEMU methods can be divided into two categories: FEMU based on modal parameters and FEMU based on

frequency response function (FRF). The former needs modal parameter identification, which inevitably introduces the identification error, and requires that the measured degree of freedom (DOF) be consistent with the DOF of the analytical model [3]. FEMU based on FRF does not need to carry out modal analysis and mode matching, so it is suitable for structures with relatively dense modal distribution [4]. In addition, the FRF contains much information, which increases the available data and has a wider range of applications [5].

The results of structural model updating are important for engineers to accurately model similar types of structures in the future. Updated numerical models can be used in numerous engineering fields (e.g., structural vibration control, force identification, vehicle load identification of bridge systems, and structural damage detection) [6]. One of the main limitations of the FEMU in the engineering application is the computational efficiency. In theory, the higher the density of the finite element mesh, the higher the

accuracy of the structure response prediction and the more reliable the model updating result. However, a fine finite element mesh will result in a significant increase in the computational time of the individual theoretical model response. Methods for constrained nonlinear optimization are typically used to solve the inverse problem of FEMU considering an objective function describing the discrepancies between the predicted FEM response and the measured one. Complex relationship exists between the model parameters to be identified and the objective function. The objective function may include many local minima. Gradient-based methods are commonly used for FEMU [7]. However, they might be trapped in local minima and their solution heavily depends on the starting point (i.e., initial guess of the model parameters). In order to avoid this issue, different global optimization algorithms have been used for FEMU [2]. The computational costs of the above methods are high. Surrogate model can provide a cheaper but lower-fidelity solution. The surrogate model is gaining popularity as a way of fast developed approximation for time-consuming simulations [8].

The surrogate model does not need the complicated calculation as the FEM does. It is an approximate model constructed directly using the relationship between inputs (design parameters) and outputs (structural responses). The commonly used surrogate models include response surface method (RSM), neural network (NN), radial basis function (RBF), support vector regression (SVR), Kriging model, and so on [9–12]. Kriging model is an equivalent model based on Kriging interpolation. Unlike other surrogate models, Kriging model can not only give the prevaluation of unknown function but also get the error estimate of the prevaluation. Only a small number of samples can accurately describe the relationship between the inputs and outputs of the structure, which is widely used in the field of evaluation of machine tools [13], structural reliability analysis [14], and model updating [15]. In the field of FEMU, Zhang and Guo [16] applied Kriging theory to FEM confirmation to predict the response of the structure. Jensen et al. [17] integrated an adaptive metamodel into a FEMU using dynamic response data. The updating technique is combined with an adaptive surrogate model based on Kriging interpolation of the measure-of-fit function. Yang et al. [18] presented a new surrogate model-based FEMU taking advantage of the measured FRFs. To improve the accuracy of the surrogate model, Han et al. [19] proposed a novel formulation of gradient-enhanced surrogate model, called weighted gradient-enhanced Kriging, in combination with the adjoint method to ameliorate the curse of dimensionality for high-dimensional surrogate model and design optimizations. Leifsson et al. [20] presented a method for multiobjective design optimization with variable-fidelity models and response surface surrogates, and the underlying low-fidelity model is corrected using parameterized output space mapping.

However, most methods for constructing Kriging model need to take some samples and to build a Kriging model with certain precision based on the samples and their corresponding responses. Then, the Kriging model takes place of

the FEM to carry out iterative optimization. If the precision of the constructed Kriging model is too low, it may result in poor or even failed optimization results. In this case, samples must be reextracted and the Kriging model must be reconstructed. In addition, most of the methods have chosen the frequency as the response of the surrogate model. However, as an important part of model updating, FRF can provide more structural dynamic information. Unfortunately, FRF is rarely used as the response of surrogate model. Therefore, in this paper, the Kriging model with good simulation effect is applied to the model updating based on FRF data. The initial Kriging model is constructed by the parameters to be modified and the acceleration frequency response functions. In order to improve its accuracy, new sample points are added with the mean square error (MSE) criterion, and the Kriging model is updated iteratively. Then, the Kriging model which meets the accuracy requirement is applied to model updating of a truss structure. The Cuckoo algorithm with better global optimization ability is used to optimize the parameters. The numerical example verifies the effectiveness of the proposed method.

The remainder of this paper is organized as follows: Section 2 gives an overview of the Kriging model. Section 3 presents the model updating based on the Kriging model, including the MSE criterion, the objective function, and the model updating process. Section 4 provides case studies. Finally, Section 5 provides the conclusions.

2. Kriging Model

Kriging model is considered as the best linear unbiased estimation to the real computer model. It is a semiparametric interpolation technique which estimates the unknown information at one point according to the known information [21]. Nowadays, it has become a popular method for approximating deterministic computer model [22].

A Kriging model is a surrogate model based on a stochastic process. The model includes linear regression part and nonparametric part. And the latter can be considered as the realization of a stochastic process. For a given set of sample data (input) $\mathbf{X} = [x_1, x_2, \dots, x_n]^T$ and the observed response (output) $\mathbf{Y} = [y_1, y_2, \dots, y_n]^T$, the expression of Kriging model is

$$y(\mathbf{x}) = \sum_{l=1}^p \beta_l f_l(\mathbf{x}_i) + z(\mathbf{x}_i) = \mathbf{f}^T(\mathbf{x}_i) \boldsymbol{\beta} + z(\mathbf{x}_i), \quad i = 1, 2, \dots, n, \quad (1)$$

where $\boldsymbol{\beta} = [\beta_1, \beta_2, \dots, \beta_p]^T$ is the coefficient vector to be estimated; $\mathbf{f}(\mathbf{x}) = [f_1(\mathbf{x}), f_2(\mathbf{x}), \dots, f_p(\mathbf{x})]^T$ is the polynomial vector of the sample \mathbf{x} ; p is the number of $f_i(\mathbf{x})$; n is the number of sample points; and $z(\mathbf{x})$ represents error and is assumed to be a stochastic process that follows a normal distribution $N(0, \sigma^2)$ with a zero mean and standard deviation σ generally and has nonzero covariance estimated by

$$\text{Cov}[z(\mathbf{x}_i), z(\mathbf{x}_j)] = \sigma^2 R(\mathbf{x}_i, \mathbf{x}_j), \quad i, j = 1, 2, \dots, n, \quad (2)$$

where \mathbf{x}_i and \mathbf{x}_j are two sample points; σ^2 is the variance of $z(\mathbf{x})$; and $R(\mathbf{x}_i, \mathbf{x}_j)$ is the correlation function characterizing

the correlation between any two sample points. Different $R(\mathbf{x}_i, \mathbf{x}_j)$ may induce different approximation accuracy of the constructed Kriging model. To estimate the stochastic process $z(\mathbf{x})$, assuming that the true response surface of Kriging model is continuous, any two points will tend to have the same value as the distance approaches zero and it is the same for $z(\mathbf{x})$ of two points. Thus, the correlation between $z(\mathbf{x})$ of any two sample points can be expressed as a function of their spatial distance. The most widely used Gaussian correlation model is adapted [18]:

$$R(\mathbf{x}_i, \mathbf{x}_j) = \exp\left(-\sum_{k=1}^m \theta_k |x_i^k - x_j^k|^2\right), \quad (3)$$

where x_i^k and x_j^k are the k th components of the two sample points \mathbf{x}_i and \mathbf{x}_j , respectively; m denotes the number of design variables; and θ_k is the correlation coefficient which controls the decay rate of correlation on different dimensions. And then the matrix of correlation functions can be expressed as

$$\mathbf{R} = \begin{bmatrix} R(\mathbf{x}_1, \mathbf{x}_1) & \cdots & R(\mathbf{x}_1, \mathbf{x}_n) \\ \vdots & \ddots & \vdots \\ R(\mathbf{x}_n, \mathbf{x}_1) & \cdots & R(\mathbf{x}_n, \mathbf{x}_n) \end{bmatrix}. \quad (4)$$

When training the parameters in the Kriging model, the maximum likelihood estimation is usually used. The likelihood function of the sample point can then be expressed as

$$L = \frac{1}{(2\pi\sigma^2)^{n/2} |\mathbf{R}|^{1/2}} \exp\left[-\frac{(\mathbf{Y} - \mathbf{F}\boldsymbol{\beta})^T \mathbf{R}^{-1} (\mathbf{Y} - \mathbf{F}\boldsymbol{\beta})}{2\sigma^2}\right], \quad (5)$$

where $|\mathbf{R}|$ is the determinant of \mathbf{R} , which is a function of θ_k ; \mathbf{Y} is a column vector which is composed of the outputs (responses) of training samples; and \mathbf{F} is a matrix of vector $\mathbf{f}(\mathbf{x})$ from each sample point. The least squares estimations of $\boldsymbol{\beta}$ and σ^2 can be expressed as

$$\hat{\boldsymbol{\beta}} = (\mathbf{F}^T \mathbf{R}^{-1} \mathbf{F})^{-1} \mathbf{F}^T \mathbf{R}^{-1} \mathbf{Y}, \quad (6)$$

$$\hat{\sigma}^2 = \frac{(\mathbf{Y} - \mathbf{F}\hat{\boldsymbol{\beta}})^T \mathbf{R}^{-1} (\mathbf{Y} - \mathbf{F}\hat{\boldsymbol{\beta}})}{n}. \quad (7)$$

Substituting equation (6) and equation (7) in equation (5) and ignoring the constant term, the logarithmic form of the maximum likelihood function can be expressed as

$$\ln(L) \approx -\frac{n}{2} \ln(\hat{\sigma}^2) - \frac{1}{2} \ln|\mathbf{R}|. \quad (8)$$

Both $\hat{\sigma}$ and \mathbf{R} are the functions of θ_k . And they can be obtained from the maximum likelihood estimation of the response. So, by solving the maximum value of the above expression, the value of θ_k can be determined.

Stochastic distribution $z(\mathbf{x})$ (in equation (1)) is sufficient to indicate the changing trend of the function response, so the regression part $\mathbf{f}^T(\mathbf{x})$ is regarded as a constant term. Then, the unique unknown parameter in the Kriging model is θ_k , which can be obtained through optimization algorithm.

After the Kriging model is constructed, the next step is to predict the response value of the point to be measured. For

any point \mathbf{x}_0 to be measured, its response value $\hat{y}(\mathbf{x}_0)$ can be expressed as

$$\hat{y}(\mathbf{x}_0) = \mathbf{f}^T(\mathbf{x}_0) \hat{\boldsymbol{\beta}} + \mathbf{r}^T(\mathbf{x}_0) \mathbf{R}^{-1} (\mathbf{Y} - \mathbf{F}\hat{\boldsymbol{\beta}}). \quad (9)$$

The prediction accuracy can be evaluated by estimating MSE of the predicted value, which can be estimated as

$$\hat{s}^2(\mathbf{x}) = \sigma^2 \left[1 - \{\mathbf{f}^T(\mathbf{x}), \mathbf{r}^T(\mathbf{x})\} \begin{bmatrix} 0 & \mathbf{F}^T \\ \mathbf{F} & \mathbf{R} \end{bmatrix}^{-1} \begin{Bmatrix} \mathbf{f}(\mathbf{x}) \\ \mathbf{r}(\mathbf{x}) \end{Bmatrix} \right], \quad (10)$$

where $\mathbf{r}^T(\mathbf{x}_0)$ is the row vector of correlation function between each sample point and the point \mathbf{x}_0 to be measured:

$$\mathbf{r}^T(\mathbf{x}_0) = [R(\mathbf{x}_0, \mathbf{x}_1), R(\mathbf{x}_0, \mathbf{x}_2), \dots, R(\mathbf{x}_0, \mathbf{x}_n)]. \quad (11)$$

3. Kriging-Based Model Updating Method

3.1. Improvement of Kriging Model. The accuracy of Kriging model directly affects the results of model updating. Constructing a high-precision Kriging model requires a large number of sample points. However, the number of sample points is the key to restrict the computational efficiency of Kriging model. The prediction of each new point needs to compute the correlation between the new sample point and all sample points. Therefore, in order to ensure the computational efficiency, the number of sample points should not be too large. But small number of sample points may lead to low accuracy of the model. In order to make Kriging model have a good compromise between computational efficiency and accuracy, it is necessary to add new sample points in effective area according to certain rules (infill criteria).

At present, the infill criteria mainly include improved expectation criterion (EI criterion), improved probability criterion (PI criterion), confidence lower bound criterion (LCB criterion), and mean square error criterion (MSE criterion) [12]. In this paper, the MSE criterion is selected to add new sample points for updating the Kriging model. The estimation of root mean square error (RMSE) provided by the Kriging model is used to guide the addition of new sample points, thereby improving the global accuracy of the model. Relative to the optimization of model updating, the optimization here is referred as suboptimization. In short, it is to use a reasonable optimization algorithm to solve the following optimization problem so as to get a new sample point:

$$\text{Max MSE}(\hat{y}(\mathbf{x})), \quad \mathbf{x}_1 \leq \mathbf{x} \leq \mathbf{x}_u,$$

$$\text{MSE}(\hat{y}(\mathbf{x})) = s^2(\mathbf{x}) = \sigma^2 \left(1 - \mathbf{r}^T \mathbf{R}^{-1} \mathbf{r} + \frac{(1 - \mathbf{F}^T \mathbf{R}^{-1} \mathbf{r})^2}{\mathbf{F}^T \mathbf{R}^{-1} \mathbf{F}} \right), \quad (12)$$

where \mathbf{x}_1 is the lower bound of design parameters; \mathbf{x}_u is the upper bound of design parameters; $\hat{y}(\mathbf{x})$ is the predicted response of the Kriging model at the sample point; $s^2(\mathbf{x})$ denotes the MSE estimation of the Kriging model; σ is the variance of the stochastic process; \mathbf{R} is the matrix of correlation functions between sample points; \mathbf{R}^{-1} is the inverse

of \mathbf{R} ; \mathbf{r} is a correlation vector, consisting of correlation functions between unknown points and all known sample points; \mathbf{F} is a matrix of polynomial vector for each sample point; and \mathbf{F}^T is the transpose of \mathbf{F} .

It is necessary to choose a suitable convergence criterion to terminate the surrogate infill process. Here, the maximum number of new samples is taken as the termination criterion. The solution for the location of the maximum RMSE is finished by Cuckoo algorithm.

The main steps of updating the Kriging model can be described as follows:

- (1) Construct the initial Kriging model according to the theory in Section 2.
- (2) Compute the maximum RMSE value of the current Kriging model by the Cuckoo algorithm and add it into the set of sample points.
- (3) Run the finite element analysis program to compute the responses of the new sample points and update the initial Kriging model until the set termination condition is reached.

The RMSE distribution of one-dimensional Schwefel function is shown in Figure 1. As shown in Figure 1(a), the sample point corresponding to the maximum RMSE is around 0.8. Figure 1(b) is obtained after adding this sample point; it can be seen that the precision of the surrogate model is greatly improved. Therefore, it is an effective method to update the Kriging model by using the optimization algorithm step by step to select the point with the largest RMSE as the new sample point.

3.2. Objective Function. Essentially, model updating is an optimization problem. Minimizing the objective function, the modified values of design parameters are obtained by solving the optimization problem. In this paper, the objective function is established based on the differences of the acceleration frequency response function between the experimental model and Kriging model.

In the frequency domain, the general mathematical representation of n DOFs system is expressed as

$$(-\omega^2\mathbf{M} + i\omega\mathbf{C} + \mathbf{K})\mathbf{X}(\omega) = \mathbf{F}(\omega), \quad (13)$$

where \mathbf{M} , \mathbf{K} , and \mathbf{C} are $n \times n$ matrices of mass, stiffness, and damping, respectively. $\mathbf{X}(\omega)$ is $n \times 1$ displacement response vector subjected to the applied force vector of $\mathbf{F}(\omega)$. ω is the excitation frequency. The displacement vector $\mathbf{X}(\omega)$ can be achieved by

$$\mathbf{X}(\omega) = \mathbf{H}(\omega)\mathbf{F}(\omega), \quad (14)$$

where $\mathbf{H}(\omega)$ is a $n \times n$ FRF matrix defined as

$$\mathbf{H}(\omega) = \left[\mathbf{M} - \frac{i\mathbf{C}}{\omega} - \frac{\mathbf{K}}{\omega^2} \right]^{-1}. \quad (15)$$

The objective function here is defined as

$$\text{Obj} = \sum_{i=1}^{\max F} |\hat{y}(\omega_i) - \log_{10} H(\omega_i)|, \quad (16)$$

where $\hat{y}(\omega_i)$ represents the prediction response of the updated Kriging model at ω_i ; $\max F$ denotes the maximum observation frequency; and $H(\omega_i)$ represents the response of the structure at ω_i . The peak value of the FRF is usually large at some frequency points, which will affect the prediction accuracy of the Kriging model, so the logarithmic (\log (FRF)) is taken as the response.

Many optimization algorithms can be used to solve equation (17). The Cuckoo algorithm [23] has strong global search ability due to its unique Lévy performance. Moreover, it has the advantages of less parameters, simple operation, easy implementation, and good optimization performance. Therefore, the Cuckoo algorithm is used to solve the parameters to be modified.

3.3. Process of Model Updating. As mentioned above, when the Kriging model is introduced into the structural FEMU, the Kriging model replaces the FEM to participate in optimization, and thus FRF model updating is fulfilled.

The main steps of model updating method based on Kriging model can be summarized as follows:

Step 1: select the excitation point and measurement point and determinate the parameters to be modified.

Step 2: generate initial sample points of the modified parameters by design of experiment (DOE).

Step 3: run the finite element analysis program to compute the response of the sample points and construct the initial Kriging model.

Step 4: find the point with the maximum RMSE of the current Kriging model by the Cuckoo algorithm and add it into the set of sample points.

Step 5: compute the responses of the new sample points and update the initial Kriging model.

Step 6: check whether the maximum number of new samples is satisfied. If it is, go to Step 7. Otherwise, go back to Step 4 and continue adding new points.

Step 7: take equation (17) as the target; the updated Kriging model is used to replace the FEM to participate in optimization, and the modified values of parameters are obtained by the Cuckoo algorithm.

The flow chart of model updating is shown in Figure 2.

4. Numerical Example

A plane truss structure (Figure 3) is taken as an example to verify the model updating method. The truss has 14 nodes and 25 DOFs. The elasticity modulus of each bar element is 210 GPa and the density is $7850 \text{ kg}\cdot\text{m}^{-3}$. Select the first fourth modes as the modes of interest.

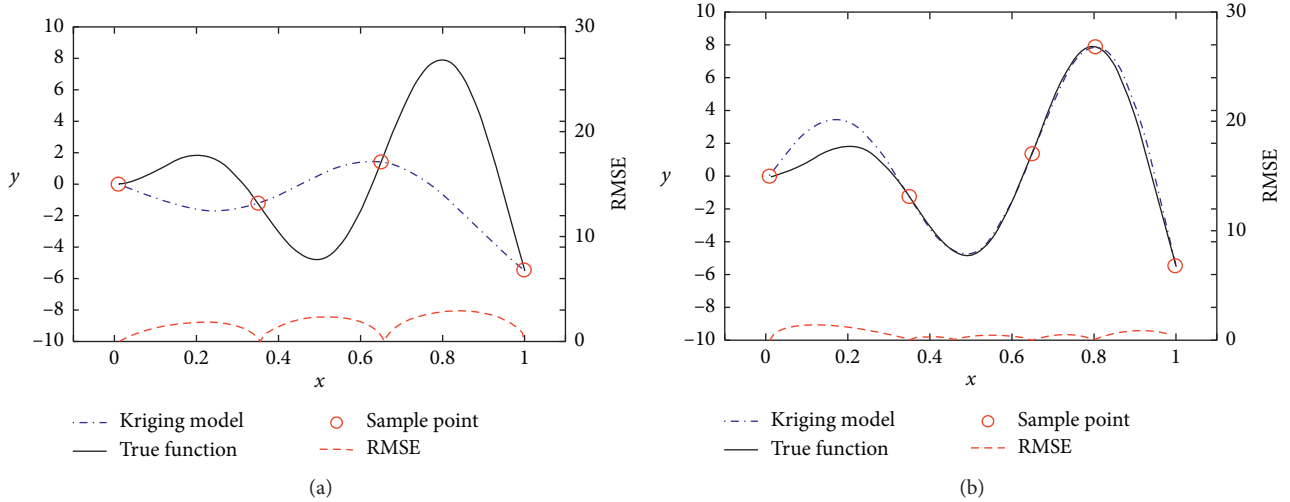


FIGURE 1: RMSE distribution of Schwefel function. (a) Before adding point. (b) After adding point.

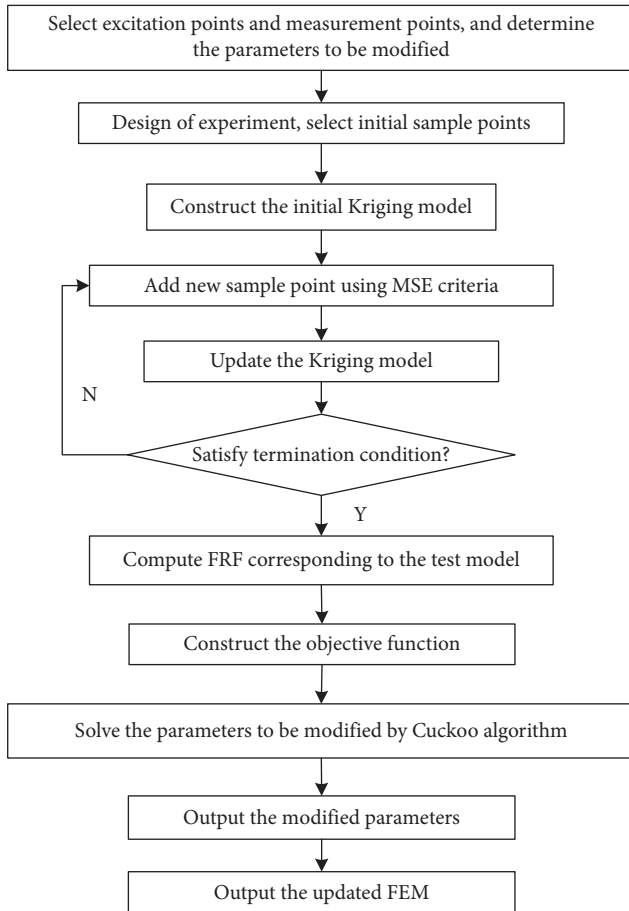


FIGURE 2: Flow chart of model updating.

4.1. Selection of Excitation Points and Measurement Points. Modal participation criterion is used for selecting excitation points. Modal participation [24] is applied to evaluate the contribution of each DOF to the excitation modes of the structure. Modal participation can be expressed as

$$W_{qi} = \sum_{p=1}^{N_0} |A_{pqi}|, \quad q = 1, 2, \dots, N_0, i = 1, 2, \dots, r, \quad (17)$$

where subscripts p and q denote the output DOFs and input DOFs, respectively; r represents number of modes; N_0 represents the number of DOFs; and A_{pqi} represents the residue.

Assuming that the structure is proportional damping, the FRF can be expressed as

$$H_{pq}(\omega) = \sum_{i=1}^m \frac{\phi_{pi}\phi_{qi}}{\omega_i^2 - \omega^2 + 2i\xi_i\omega_i\omega}, \quad (18)$$

where ϕ_{pi} and ϕ_{qi} represent the (i, p) th and (i, q) th elements the modal matrix, respectively; ω_i denotes the undamped natural frequency at the i th order mode; and ξ_i represents the damped coefficient at the i th order mode. A_{pqi} in equation (7) can be expressed as

$$A_{pqi} = \phi_{pi}\phi_{qi}. \quad (19)$$

The contribution of the q th DOF to the excitation of all modes of interest can be expressed as

$$W_q = \sum_{i=1}^r W_{qi}, \quad q = 1, 2, \dots, N_0. \quad (20)$$

In single-input and single-output modal response test, structural DOF with maximum W_q can be selected as the optimal excitation point. W_{qi} and W_q of each DOF of the structure are shown in Figure 4. The maximum W_q is at the 20th DOF in the Y-direction of node 11. So, the 20th DOF is chosen as the best excitation point in the test. The DOFs in the Y-direction make the most important contribution to the first four modes of excitation. This is consistent with the characteristics of the plane truss structure.

There are also many methods for selecting measurement points, but most of them are multipoint selection. According to the characteristics of the model, a DOF in the Y-direction should be selected as the sensor measurement point. The

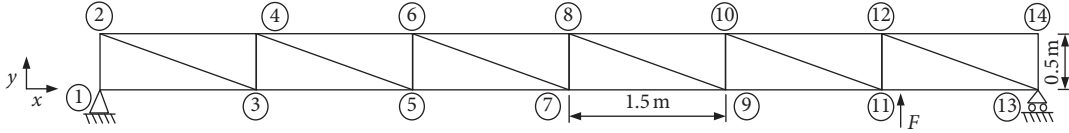
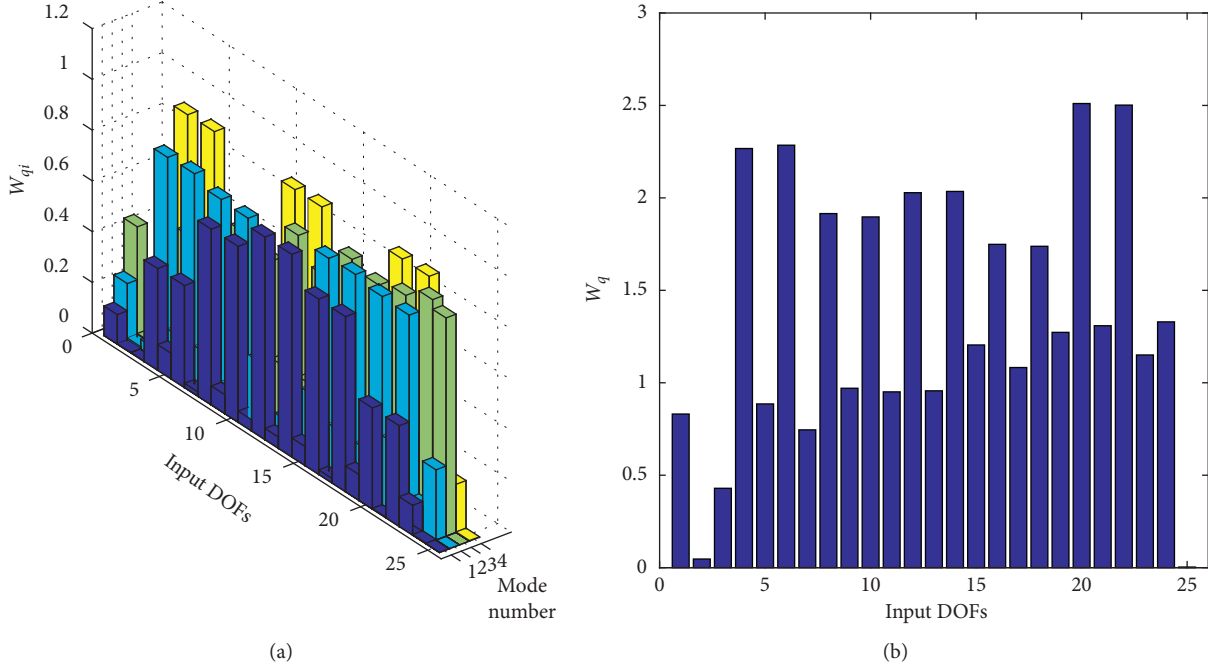


FIGURE 3: Plane truss model.

FIGURE 4: Value of modal participation. (a) W_{qi} . (b) W_q .

fourth DOF in the Y-direction at the 3rd node is chosen as the measurement point.

4.2. Test Design and Initial Sample Selection. In this paper, the FEM shown in Figure 3 is used as the test model, and the corresponding FEM is obtained by deviating from the values of the parameters to be modified in the test model. Considering that the test data will be affected by noise in the actual data measurement, 5% random noise is added to the response of the test model. The elasticity modulus and material density are chosen as parameters to be modified and their values are deviated. The elasticity modulus is increased by 10%. The material density is reduced by 10%. The FEM parameters are shown in Table 1.

Before constructing the surrogate model, selecting the sample points is the first step. For the global optimization problem, a better method is to select a set of sample points through DOE. The method proposed in this paper has no strict requirements for the number of initial sample points, which is different from the traditional Kriging model. Considering the efficiency of adding new sample points, the number of initial samples should not be too small. In other words, the optimization efficiency of the improved Kriging model based on our method is not obviously dependent on the number of initial sample points. Here, the Latin

TABLE 1: Parameters of test model and FEM.

Parameters	Test value	Initial error (%)	FEM value
Elasticity modulus (GPa)	210	10	231
Material density ($\text{kg}\cdot\text{m}^{-3}$)	7850	-10	7065

hypercube sampling (LHS) is used to sample the two parameters (elasticity modulus and material density). Finally, 40 samples are extracted.

4.3. Construction and Verification of Kriging Model. On the basis of the 40 extracted samples and their corresponding acceleration FRFs, the initial Kriging model is constructed. Then, the new samples are added according to the MSE criterion introduced in Section 3, and the maximum number of additional sample points is 40. Then, the improved Kriging model is built. The FRFs at the fourth DOF of the FEM are predicted by using Kriging model and the improved Kriging model, respectively. The results are shown in Figure 5 (RMSE1 denotes RMSE of Kriging model; RMSE2 denotes RMSE of the improved Kriging model). Both the Kriging model and the improved Kriging model have good prediction accuracy. However, the improved Kriging model performs better in predicting the peak value of the curve, and

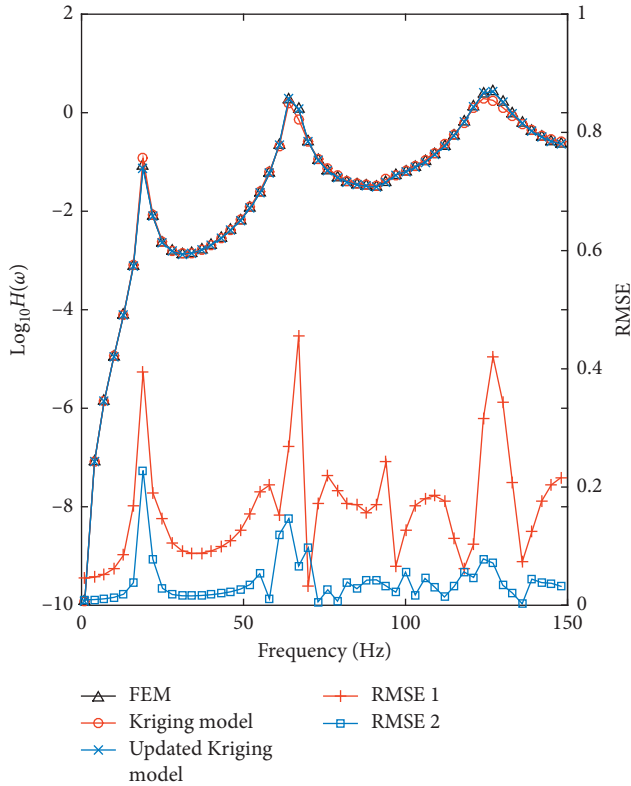


FIGURE 5: Log(FRF) of FEM.

the RMSE value of the improved Kriging model is smaller than that of the Kriging model.

The fitting response surface and RMSE surface obtained by updating the Kriging model at the 50th frequency point are shown in Figure 6. The overlap between the sample response and the predicted response from the improved Kriging model is good, and the maximum RMSE is less than 0.05. The improved Kriging model has good approximation accuracy to the FEM.

4.4. Model Updating. The improved Kriging model mentioned above is used to substitute the FEM to optimize iteratively. Assume that the test parameters are within the interval of finite element parameter values. The Cuckoo algorithm is used to find the optimum iteratively. The number of nests is 40, and the maximum number of iterations is 100. In order to prove the stability of the algorithm, the iterative convergence curve is shown in Figure 7 when the algorithm runs 100 times. The Cuckoo algorithm is stable and converges before the number of iterations reaches 60. The difference between the optimal value and the worst value is also very small.

In order to compare with the optimization effect of the updated Kriging model, the second-order RSM and the RBF are constructed based on the same sample points. The average values and average errors of the modified parameters are shown in Table 2. Except for the second-order RSM, all the other three methods obtain good results, but the

parameter values by the improved Kriging model are more accurate, and the average error is the smallest.

All the algorithms are coded in Matlab 2014b. The operating system is Windows 10. Simulation hardware is a PC with 3.50 GHz Intel Pentium (R) G4560 and 12.00 GB memory, and all the algorithms are repeated 5 times. The total computation time of model updating using these surrogate models is counted, and the average time is shown in Table 3. The RSM takes the least time. The RBF needs the longest time. And the Kriging model needs longer time than RSM, but its computational efficiency is much higher than RBF.

In summary, the Kriging model has the best accuracy and needs less time. The accuracy of RSM is too poor. The computation time of RBF is too long. RSM and RBF cannot be compromised between accuracy and time. This shows that the proposed method can improve the computational efficiency while satisfying the accuracy and has little dependence on the number of sample points. It is noted that there are some errors between the Kriging model and the improved Kriging model, which are not caused by the insufficient optimization ability of the optimization algorithm, but by the prediction error of the Kriging model itself. So, only if the Kriging model is accurate enough, it can be used to modify the structure model to reduce the computational cost and get the accurate updating results.

The FRFs predicted by the Kriging model, the updated Kriging model, RBF, and RSM are shown in Figure 8. Comparison of updated Kriging model with Kriging model, RSM, and RBF is shown in Figures 8(a) and 8(b), respectively (RMSE1 denotes RMSE of Kriging model; RMSE2 denotes RMSE of the updated Kriging model; RMSE3 denotes RMSE of RSM; RMSE4 denotes RMSE of RBF). The prediction value of the updated Kriging model is more accurate than others. The form of FRFs of the test model and the FEM does not change, and the peak values are very close, only causing movement along the frequency axis.

The FEM is updated with the average modified values obtained from the updated Kriging model. By comparing the real and imaginary FRF curves before and after modification at the measurement points, the updating effect of the proposed method is further verified. The comparison curve between real and imaginary parts of FRF before and after updating is shown in Figure 9. The FRFs of the updated FEM (whether real or imaginary part), can coincide well with the FRFs of the test model.

4.5. Damage Identification. In order to further verify the proposed method, the above mentioned truss structure elements 8, 12, 15, 17, 21, and 25 are assumed to be damage elements. Their stiffness of the elements is reduced by 10%, 10%, 20%, 20%, 30%, and 30%, respectively. The elasticity modulus of each damaged unit is identified. The number of samples is set to 500. The maximum number of new additional sample points is 100. The maximum number of iterations of the Cuckoo algorithm is 300. The damage identification errors by the Kriging model, the updated Kriging model, the second-order RSM, and RBF under

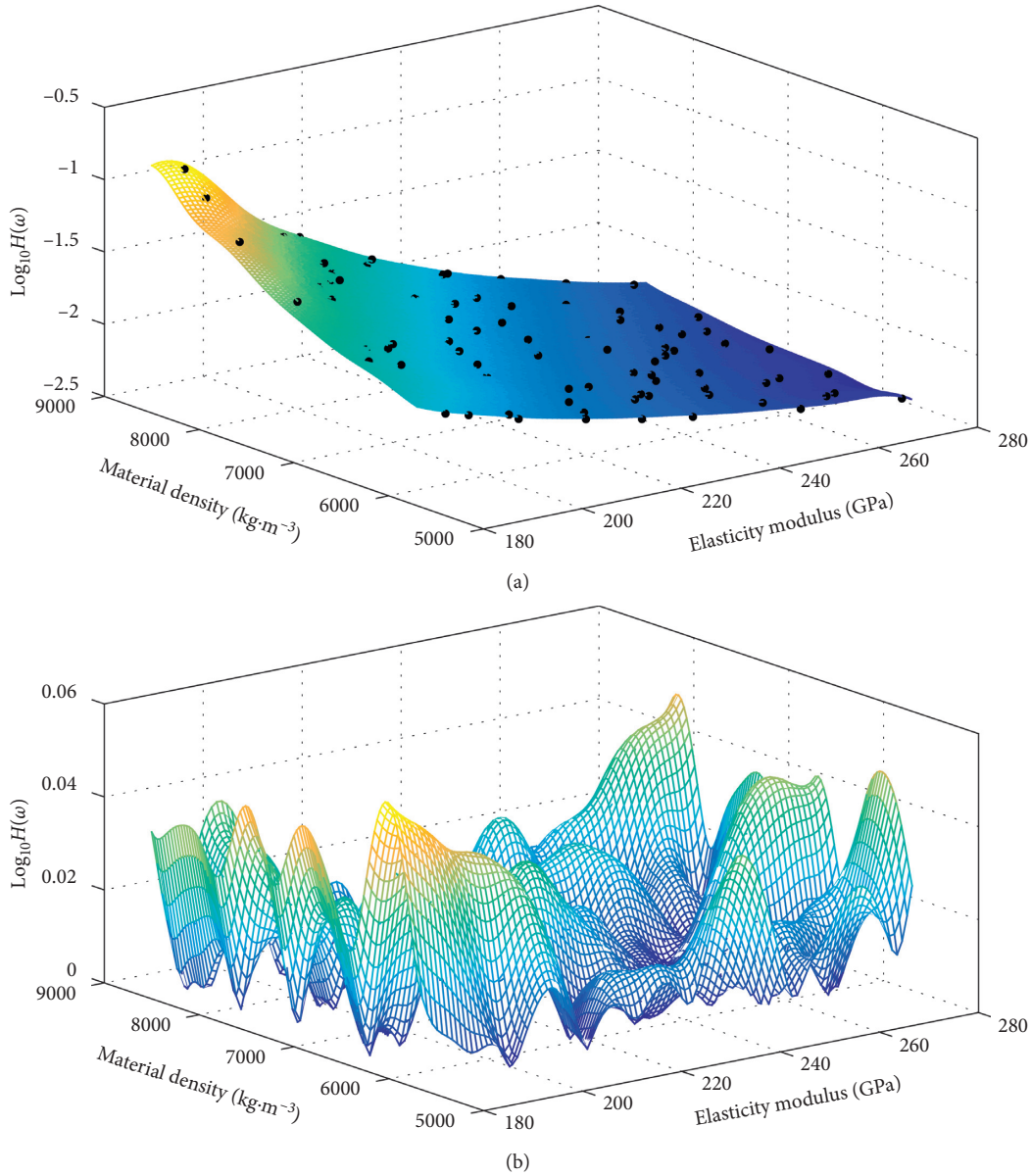


FIGURE 6: Prediction values of the improved Kriging model. (a) Response values. (b) RMSE values.

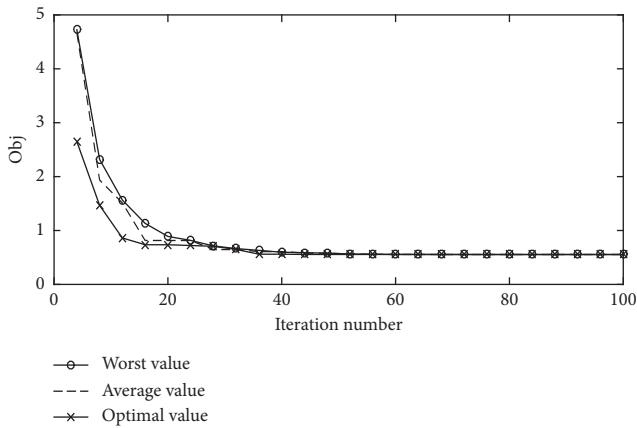


FIGURE 7: Iterative curve.

different measurement points are shown in Table 4. The effects of different measurement points on damage identification accuracy are different. When sensors are evenly arranged at all Y-direction DOFs, 4 surrogate models have better identification accuracy. The identification error of the updated Kriging model is less than 0.5%. For a single measurement point, except for 14-Y measurement point, the identification accuracy of the four methods for unit 12 at other measurement points is poor; at 5-Y measurement point, the surrogate models have larger identification error. The identification accuracy of the updated Kriging model is better than that of the other surrogate models on the whole. For the identification of elasticity modulus of the truss damage elements, the computation time of the Kriging model is about twice that of RBF and 0.04 times that of RSM.

TABLE 2: Parameters and errors of model updating.

		Elasticity modulus (GPa)	Material density ($\text{kg}\cdot\text{m}^{-3}$)
Values by different methods	Test	210.000	7850.000
	K	211.273	7891.508
	U-K	210.005	7863.081
	RBF	211.285	7903.145
	RSM	210.945	8052.001
Average errors by different methods (%)	K	0.606	0.529
	U-K	0.002	0.167
	RBF	0.612	0.677
	RSM	0.450	2.573

Note. K represents the Kriging model; U-K represents the updated Kriging model.

TABLE 3: Computation time.

Surrogate model	Kriging	RBF	RSM
Average time (s)	13.949	695.802	3.837

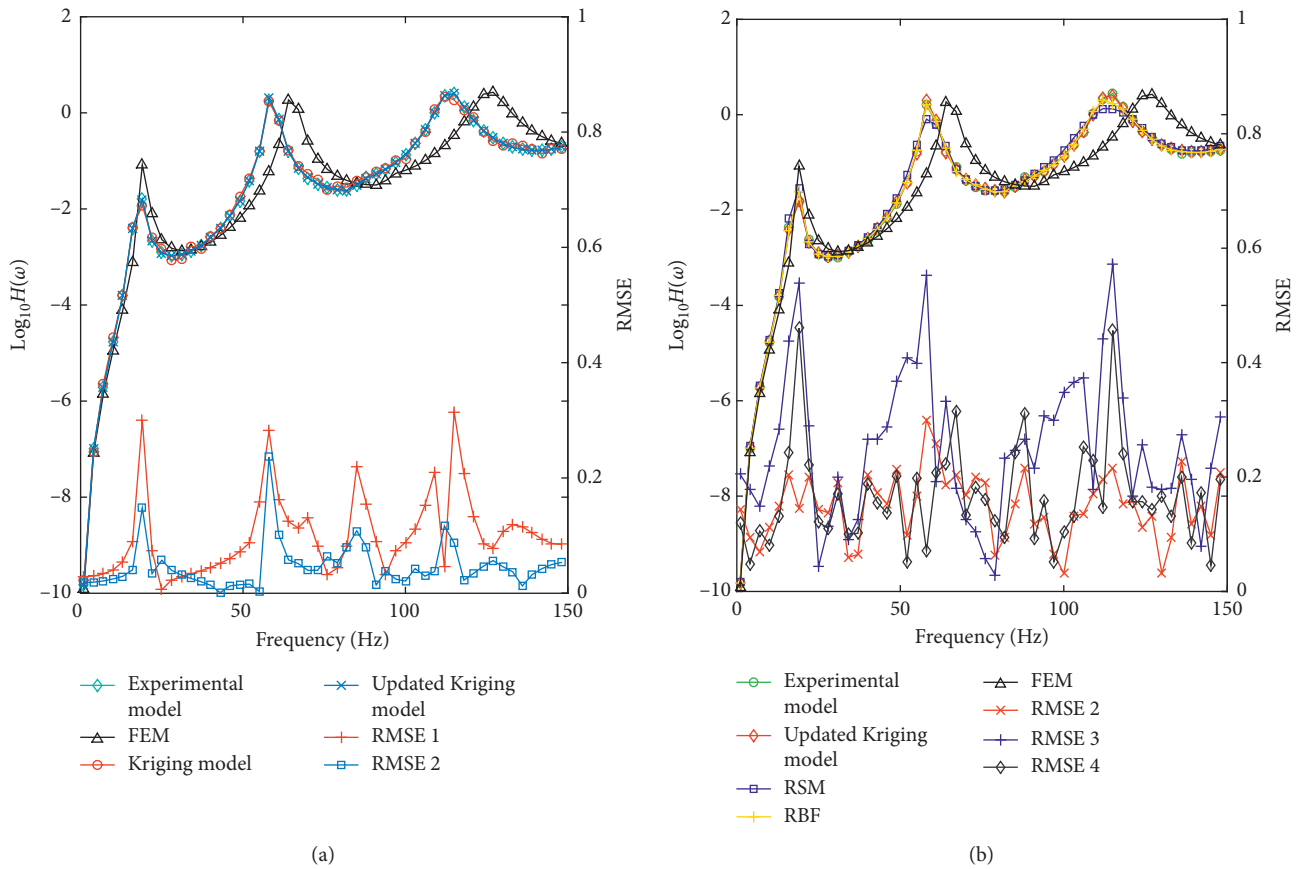


FIGURE 8: Log(FRF) of experimental model. (a) Comparison of the updated Kriging model with the Kriging model. (b) Comparison of the updated Kriging model with RBF and RSM.

FEMU based on Kriging model can make a good compromise between computational accuracy and time. The accuracy of damage identification is not only affected by the surrogate models but also affected by the selection of measurement points.

5. Conclusions

In this paper, the updated Kriging model is used to modify the parameters and to identify the damage of the structure. The conclusions are as follows:

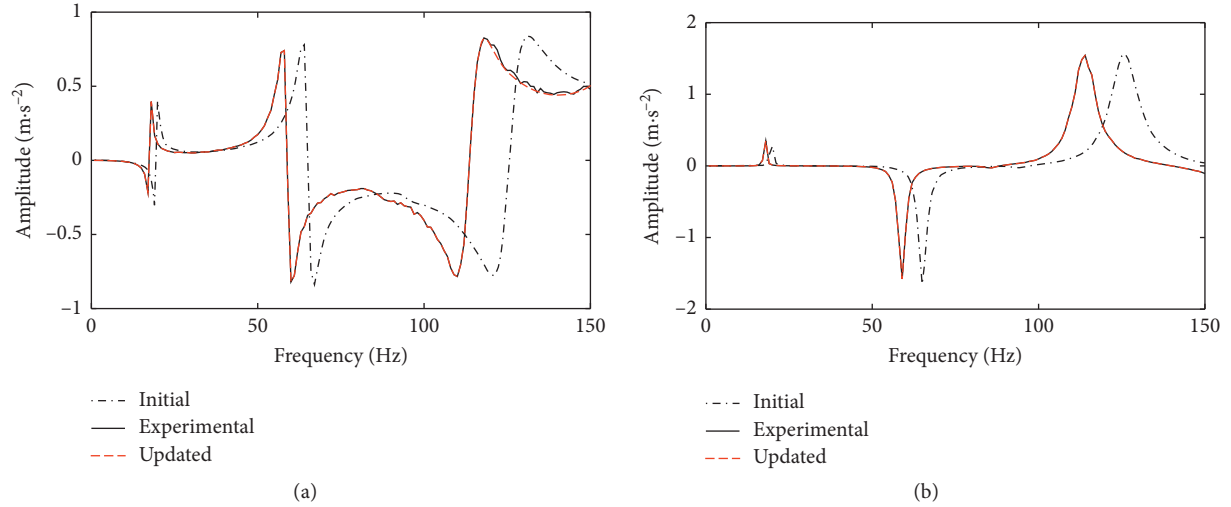


FIGURE 9: FRFs before and after being updated. (a) Real part. (b) Imaginary part.

TABLE 4: Identification error of elasticity modulus of each damage unit.

Measurement location	Method	Identification errors of damage units (%)					
		8	12	15	17	21	25
3-Y	K	1.594	5.125	6.225	0.504	0.098	0.946
	U-K	1.315	3.812	4.334	0.490	0.099	0.622
	RBF	0.487	2.339	1.750	0.577	0.006	0.234
	RSM	1.064	8.371	6.323	0.229	0.342	1.064
5-Y	K	0.722	8.359	8.830	1.372	0.492	1.815
	U-K	0.431	6.488	6.261	1.253	0.340	1.406
	RBF	0.090	21.078	20.502	11.459	1.653	5.297
	RSM	3.882	11.270	5.399	6.676	0.588	1.499
7-Y	K	0.890	7.373	0.768	6.824	0.557	0.280
	U-K	0.897	3.470	0.054	2.850	0.108	0.017
	RBF	3.718	6.606	1.231	8.987	0.055	0.904
	RSM	4.663	1.201	0.324	2.165	0.202	0.337
9-Y	K	0.982	2.746	0.028	1.506	0.332	0.073
	U-K	0.685	2.160	0.030	1.126	0.183	0.025
	RBF	3.469	1.720	0.096	1.606	0.081	0.161
	RSM	4.522	1.879	0.627	0.626	0.492	0.743
11-Y	K	0.554	1.918	0.021	1.276	0.435	0.304
	U-K	0.552	0.916	0.031	0.327	0.087	0.132
	RBF	2.088	2.970	0.275	2.269	0.093	0.277
	RSM	5.810	2.018	0.578	1.424	0.625	0.862
14-Y	K	0.226	0.648	0.084	0.271	0.546	0.260
	U-K	0.167	0.783	0.084	0.268	0.125	0.075
	RBF	1.587	1.197	0.830	2.244	0.021	0.574
	RSM	4.519	1.752	0.639	0.631	0.478	0.634
All measurement points of Y-direction	K	0.170	0.020	0.232	0.676	0.287	0.189
	U-K	0.197	0.010	0.010	0.423	0.140	0.163
	RBF	0.244	0.486	0.468	0.155	0.301	0.289
	RSM	1.284	1.176	0.184	0.188	0.319	0.586

Note. K represents the Kriging model; U-K represents the updated Kriging model; 3-Y represents the measurement points arranged in the Y direction at the 3rd node.

(1) For modal response test, the selection of excitation point and measurement point is very important. For single-input and single-output test, modal

participation criterion can be used to select the excitation point, and the response point can be selected according to the structural characteristics.

- (2) The updated Kriging model obtained by using the MSE criterion has better accuracy than the Kriging model, and the accuracy of the model is more stable.
- (3) Compared with the second-order RSM and RBF, the updated Kriging model can improve the computational efficiency while satisfying the computational accuracy and has less dependence on the number of sample points.
- (4) The parameter errors of the updated model are less than 0.2%. When there are enough measurement points, the parameter errors of damage identification are less than 0.5%.
- (5) When the optimization algorithm has enough optimization performance, the parameter modification errors often depend on the accuracy of the surrogate models, which are independent of the optimization algorithm, and when the surrogate models are accurate enough, the parameter modification errors will tend to zero.

Further research is needed on the selection of multiple measurement points for model updating. In the following research, modal response test will be carried out.

Data Availability

The data used to support the findings of this study are available from the corresponding author upon request.

Conflicts of Interest

The authors declare no conflicts of interest.

Acknowledgments

This research was funded by the Natural Science Foundation of China (no. 51768035), Collaborative Innovation Team Project of Universities in Gansu Province (no. 2018C-12), Talent Project of Lanzhou City (no. 2017-RC-66), and Foundation of a Hundred Youth Talents Training Program of Lanzhou Jiaotong University.

References

- [1] M. I. Friswell and J. E. Mottershead, *Finite Element Model Updating in Structural Dynamics*, Kluwer Academic Publishers, Dordrecht, Netherlands, 1995.
- [2] R. Astroza, L. T. Nguyen, and T. Nestorović, "Finite element model updating using simulated annealing hybridized with unscented Kalman filter," *Computers & Structures*, vol. 177, pp. 176–191, 2016.
- [3] J. W. Zhan, M. Li, Y. Lu et al., "Dynamic evaluation method for damage of simply-supported beams based on model updating theory and FRF signature assurance criterion," *China Civil Engineer Ring Journal*, vol. 8, pp. 49–58, 2017.
- [4] H. H. Khodaparast, J. E. Mottershead, and K. J. Badcock, "Interval model updating with irreducible uncertainty using the Kriging predictor," *Mechanical Systems and Signal Processing*, vol. 25, no. 4, pp. 1204–1226, 2011.
- [5] J. L. Hu, Q. S. Yan, H. B. Zheng et al., "CFST arch/continuous beam bridge FEM model updating based on Kriging model," *Journal of Vibration and Shock*, vol. 33, no. 14, pp. 33–39, 2014.
- [6] H.-F. Lam, J. Hu, and J.-H. Yang, "Bayesian operational modal analysis and Markov chain Monte Carlo-based model updating of a factory building," *Engineering Structures*, vol. 132, pp. 314–336, 2017.
- [7] A. Teughels and G. De Roeck, "Structural damage identification of the highway bridge Z24 by FE model updating," *Journal of Sound and Vibration*, vol. 278, no. 3, pp. 589–610, 2004.
- [8] D. Huang, T. T. Allen, W. I. Notz, and R. A. Miller, "Sequential Kriging optimization using multiple-fidelity evaluations," *Structural and Multidisciplinary Optimization*, vol. 32, no. 5, pp. 369–382, 2006.
- [9] W.-X. Ren and H.-B. Chen, "Finite element model updating in structural dynamics by using the response surface method," *Engineering Structures*, vol. 32, no. 8, pp. 2455–2465, 2010.
- [10] R. I. Levin and N. A. J. Lieven, "Dynamic finite element model updating using neural networks," *Journal of Sound and Vibration*, vol. 210, no. 5, pp. 593–607, 1998.
- [11] Y. Zhang, Z. C. Hou, and Y. L. Zhao, "Finite element model updating based on response surface of the truncated singular values of frequency response functions," *Journal of Vibration Engineering*, vol. 30, no. 3, pp. 341–348, 2017.
- [12] Z. H. Han, "Kriging surrogate model and its application to design optimization: a review of recent progress," *Acta Aeronautica et Astronautica Sinica*, vol. 37, no. 11, pp. 3197–3225, 2016.
- [13] C. Deng, J. Miao, B. Wei, Y. Feng, and Y. Zhao, "Evaluation of machine tools with position-dependent milling stability based on Kriging model," *International Journal of Machine Tools and Manufacture*, vol. 124, pp. 33–42, 2018.
- [14] J. Vahedi, M. R. Ghasemi, and M. Miri, "An adaptive divergence-based method for structural reliability analysis via multiple Kriging models," *Applied Mathematical Modelling*, vol. 62, pp. 542–561, 2018.
- [15] J. T. Wang, C. J. Wang, and J. P. Zhao, "Frequency response function-based model updating using Kriging model," *Mechanical Systems and Signal Processing*, vol. 87, pp. 218–228, 2017.
- [16] D. D. Zhang and Q. T. Guo, "Application of Kriging response surface in finite element model validation," *Journal of Vibration and Shock*, vol. 32, no. 9, pp. 187–204, 2013.
- [17] H. A. Jensen, C. Esse, V. Araya, and C. Papadimitriou, "Implementation of an adaptive meta-model for Bayesian finite element model updating in time domain," *Reliability Engineering & System Safety*, vol. 160, pp. 174–190, 2017.
- [18] X. Yang, X. Guo, H. Ouyang, and D. Li, "A Kriging model based finite element model updating method for damage detection," *Applied Sciences*, vol. 7, no. 10, p. 1039, 2017.
- [19] Z.-H. Han, Y. Zhang, C.-X. Song, and K.-S. Zhang, "Weighted gradient-enhanced kriging for high-dimensional surrogate modeling and design optimization," *AIAA Journal*, vol. 55, no. 12, pp. 4330–4346, 2017.
- [20] L. Leifsson, S. Koziel, and Y. A. Tesfahunegn, "Multiobjective aerodynamic optimization by variable-fidelity models and response surface surrogates," *AIAA Journal*, vol. 54, no. 2, pp. 531–541, 2016.
- [21] J. D. Tesfahunegn and T. W. Simpson, "Use of Kriging models to approximate deterministic computer models," *AIAA Journal*, vol. 43, no. 4, pp. 853–863, 2005.
- [22] W. Hao, W. Shaoping, and M. M. Tomovic, "Modified sequential Kriging optimization for multidisciplinary complex

- product simulation,” *Chinese Journal of Aeronautics*, vol. 23, no. 5, pp. 616–622, 2010.
- [23] X. S. Yang and S. Deb, “Cuckoo Search via lévy flights,” in *Proceedings of the 2009 World Congress on Nature & Biologically Inspired Computing (NaBIC)*, pp. 210–214, IEEE, Coimbatore, India, December 2010.
- [24] W. Heylen, S. Lammens, and P. Sar, *Modal Analysis Theory and Testing*, Katholieke Univ Leuven, Department Werktuigkunde Press, Leuven, Belgium, 2nd edition, 1998.

Research Article

Effective Processing of Radar Data for Bridge Damage Detection

Tomasz Owerko  and **Przemysław Kuras** 

Department of Surveying Engineering and Civil Engineering, AGH University of Science and Technology, Kraków 30-059, Poland

Correspondence should be addressed to Tomasz Owerko; owerko@agh.edu.pl

Received 4 January 2019; Revised 12 March 2019; Accepted 20 March 2019; Published 17 April 2019

Guest Editor: Elías López-Alba

Copyright © 2019 Tomasz Owerko and Przemysław Kuras. This is an open access article distributed under the Creative Commons Attribution License, which permits unrestricted use, distribution, and reproduction in any medium, provided the original work is properly cited.

This paper presents the practical results of the evaluation of the data obtained by using ground-based radar interferometer during measurements carried out on bridge structures. Due to the nature of the objects studied, the authors proposed a comprehensive method of data analysis, which identifies whether the passage of the vehicle did not damage the bridge. The effective use of vehicles as a source of bridge excitation allowed us to first develop a method for determining the damping parameters resistant to potentially occurring beating frequencies. As a result, it is possible to determine these subsets of data registered with radar, for which it is possible to assume compliance with linear systems. This type of data, often omitted in other works, forms the basis for the second important element of the research—an algorithm based on the ARMA model supporting defect detection. The optimization of the performed calculations, in particular the proposed optimal ARMA model order, the method of fault identification based on the DSF parameter, or fault identification based on a nonmetrical Cook's distance leads to a robust and scalable method. The method's low computational complexity allows for implementation in real-time solutions. In addition, the distribution of errors and the sensitivity of classifiers based on the DSF parameter and Cook's distances leaving them will enable the automation of the classification process using machine learning. The proposed method is universal; in particular, it can be used for radar interferometry methods because it is resistant to potentially variable environmental conditions.

1. Introduction

The inspection measurements of important and non-standard engineering structures and related studies are the basis for assessing their safety. In the group of objects that must be monitored during load tests and require monitoring are, among others, bridge structures and buildings exposed to the influence of seismic factors. The monitoring of such facilities and their examination under test loads should provide a basis for assessing the safety of the structure at the time of its commissioning and in the future.

Many failures can be identified based on the analysis of observations carried out using various measuring devices. In this group, attention should be paid to the radar interferometry technique that allows simultaneous observation of many elements representing the tested structure. Its important advantage is the ability to conduct measurements in a noncontact manner and that there is no requirement to install any devices on the object.

The use of radar observations of many points on the site to analyze the health of the structure is quite wide. This type of research is carried out for both bridge and high-rise buildings by determining the vibration parameters based on dynamic displacement monitoring [1]. Gentile and Bernardini [2] describe the application of the radar sensor to vibration full-scale measurements of a bridge in relation to the time series recorded by the conventional accelerometers. In this research, the application of the radar sensor to vibration full-scale measurements of a bridge in relation to the time series recorded by the conventional accelerometers is presented. As a result, the resonant frequencies and mode shapes of the bridge that were identified from the radar signals are compared to the corresponding quantities estimated from the data recorded by the conventional sensors. Moreover, Barros and Paiva [3] present many different types of bridge structures on which radar measurements were performed as a part of SHM. For each case study, the comparison with the akin results obtained for the same case

studies either by structural computational modeling or by other intrusive SHM techniques is described, in order to ascertain the accuracy of this nonintrusive radar interferometry. In turn, Diaferio et al. [4] focus on operational modal analysis (OMA), which is extensively used as a tool for the modal identification and the SHM of civil engineering constructions. They analyze the capability and the possibly needed improvements of the ground-based radar interferometric experimental set-up applied to a railway viaduct, as an alternative to classical experimental techniques based on the use of accelerometers, which involve high costs and long times for performing measurements and often interrupt the service of a construction. Another example of the application of radar measurements in relation to the alternative observational method, which is a vision-based measurement system based on the digital image correlation coefficient, is presented by Kohut et al. [5]. This research was carried out to assess the behavior of the tram viaduct as a result of operational loads.

Research on the condition of structures based on radar observations has also been carried out for high objects. Hu et al. [6] use radar measurements to high-rise building observations. They established a sequential quadratic programming-genetic algorithm to identify the dynamic vibration characteristics of buildings under natural environment excitation. This method not only accurately identifies resonance frequencies but also directly extracts the amplitudes of the sine and cosine components of the building vibration signals under the resonance frequencies response compared with the traditional spectrum analysis based on the fast Fourier transform.

Another example is a historic masonry bell tower examined by Castellano et al. [7]. The proposed approach exploits the extraction of modal parameters to define mechanical features of the structure such as mass, damping and stiffness matrices by means of operational modal analysis, starting from measurements performed by a very promising, expeditious, and contactless experimental technique based on radar interferometry. This approach may be very effective for structural health monitoring purposes. A different application is presented by Ochieng et al. [8]. They used a noncontact radar observation for structural health monitoring of infield wind turbine blades. Radar sensor helps the monitoring of blades during design, testing, and operation. Furthermore, it supports the determination of damage detection for infield wind turbine blades within a 3-tier SHM framework especially for those made of composite materials by way of condition parameter residuals of extracted modal frequencies and deflection.

Damage detection is one of the most important applications of SHM systems and algorithms. Modern computational technologies based on digital signal processing, the evaluation of patterns by means of machine learning, or the evaluation of patterns by the analysis of statistical characteristics of signals can be used to assess the safety of building objects [9, 10].

Recently, an important trend in this field is the use of machine learning to identify potential problems. While the use of AI methods is widely known for systems based on the

analysis of dynamic data, it is also worth noting that it is possible to effectively analyze data from high-resolution measurement systems using deep machine learning methods [11]. The use of photogrammetric systems and computer vision systems can also successfully include dynamic measurements. This type of work encompasses many research directions, among which the following should be mentioned: different template matching techniques for tracking targets, coordinate conversion methods for determining calibration factors to convert image pixel displacements to physical displacements, measurements by tracking artificial targets vs. natural targets, and many others.

Finally, the applications of the measured displacement data for SHM are reviewed, including examples of structural modal property identification, structural model updating, damage detection, and cable force estimation [12]. An important element of SHM systems is not only to identify the damage but also to give such information an adequate weight. In particular, research work may include the provision of information on the SHM system including the number of sensors and sensor locations [13]. The complexity of SHM systems and a large number of sensors do not remain indifferent to the possibilities of the efficient use of systems.

As important as research work that focuses on system reliability, there are those that aim to reduce computational complexity while maintaining damage detection efficiency. In particular, unlike conventional strategies employing a frequency response function or response data, a damage detection methodology is addressed by employing transmissibility functions that retain a strong interrelation with structural damage or deterioration in order to avoid the measurement of excitation, together with the principal component analysis that leads to a reduction in computational costs [14].

Studies on SHM algorithms concern, just like in this paper, the identification of damages occurring on bridge structures. These tests, which are crucial for practical applications, must also include an analysis of the interaction between the bridge and the vehicles that constitute the source of disturbances and vibrations [15]. Long-term monitoring of objects is inherently subject to changing environmental conditions, in particular to changing weather conditions. Such changes affect both the measurement system and the behavior of the object itself. Huang et al. [16] address this problem by indicating that, in practical applications, time-varying environmental and operational conditions, such as temperature and external loadings, often overwhelm the subtle changes caused by damage. It is therefore of great significance to remove those structural changes (damage features) caused by external influences from actual structural damage. The authors present a new damage identification method based on the Kalman filter and cointegration (KFC). As a result, the environmental effects on a damage indicator are removed, thanks to the cointegration process of the Kalman filtered coefficients. Bhowmik et al. [17] show that most work to date deal with algorithms that require windowing of the gathered data that

render them ineffective for online implementation. Algorithms focused on mathematically consistent recursive techniques in a rigorous theoretical framework of structural damage detection are missing. This motivates the development of the present framework. As a solution, a baseline-free approach for continuous online damage detection of multidegree of freedom vibrating structures using recursive singular spectral analysis in conjunction with time-varying autoregressive modeling is presented. Besides, the problem of long-term monitoring is also considered by Roy et al. [18]. The authors draw attention to the fact that a direct comparison of the vibration signals or modal properties at different periods of time may not be sufficient to identify the damages and their locations. Therefore, it is important to analyze the vibration signals to extract the morphologies of the changes in these response signals and correlate them with the types, location, and magnitude of structural damage.

An interesting solution, presented by Krishnan et al. [19], successfully eliminates the need for offline post-processing and facilitates online damage detection especially when applied to streaming data without requiring any baseline data. This is a novel baseline-free approach for the continuous online damage detection of multidegree of freedom vibrating structures using recursive principal component analysis (RPCA) in conjunction with time-varying autoregressive (TVAR) modeling. In this method, the acceleration data are used to obtain recursive proper orthogonal components online using the rank-one perturbation method, followed by TVAR modeling of the first transformed response, to detect the change in the dynamic behavior of the vibrating system from its pristine state to contiguous linear/nonlinear states that indicate damage.

On the contrary, the health analysis of the structure based on data representing the stationary parts of measurement signals has been presented, among others, by Sohn et al. and Nair et al. [20, 21]. They are an important element in the proposed solution.

This work presents an algorithm for conducting research under testing or operational load that allows simultaneous observation which will allow for identifying any structural damage that may occur during testing and are the basis for building a reference database of the system based on SHM.

An algorithm for detecting and automatically identifying the defects of buildings and structures is applied. It is particularly useful for engineering structures susceptible to dynamic excitations such as bridges, viaducts, flyovers, masts, and towers, as well as free-standing chimneys (single and multi-flue) based on tests carried out under testing or operational load.

2. Proposition of the Damage Detection Algorithm

2.1. Overview. The computational technique is that the measurement signals, which are variable in time, are

measured, and the results are delivered to the computing unit in the form of time series and spectrograms, and analyses are carried out for the stationary fragments of the time series.

In the first stage, when measuring a given structure, measuring devices, such as the accelerometers, interferometric radar, or GNSS receivers, are positioned in such a way that the following can be performed:

- (a) It is possible to accurately identify the mode shapes resulting from the modal analysis of the structure
- (b) They are located in the places that are subject to damage during tests under test loads and operational loads

In the second stage, the values of the identified amplitudes obtained from those parts of the time series, which represent free vibrations, are compared with the results of the modal analysis in the range of values in the frequency domain and in the range of the logarithmic decrement of damping calculated from the Hilbert transform of free vibration [22].

Then, in the parts of the time series that represent the stationary signal, the ARMA model is fitted (a linear model of autoregressive moving average) [23]. On this basis, the damage sensitive feature (DSF), introduced by Nair et al. [21], is calculated as the normalized value (the first coefficient is divided by the square root of the sum of the squares of the first three coefficients).

In the third stage, it is calculated if the distance of the given calculated coefficient, on the basis of the given time series after the crossing of a vehicle, changes the coefficients of the regressive lines fitted into the previous realizations of the DSF with the use of Cook's distance. In this way, the dynamic behavior of the bridge, which deviates from the norm, is identified.

The signal recorded during the load testing can be divided into three parts in the time domain (Figure 1):

- (1) The data represent the stationary signal. This is the basis for finding the structure's features representing its condition prior to possible damage and in the parts representing the condition of the object after free vibration has expired. The second part is the basis for evaluating whether or not the force damaged the object.
- (2) The data represent the deflection of the construction. The standard procedure may be used to calculate other parameters such as the coefficients of the dynamic amplification factor (DAF).
- (3) The data represent the free vibration. The correctly filtered and standardization process allows for the calculation of an amplitude spectrum and also may determine if the design is acting in accordance with the damping based on the values of the logarithmic decrement of damping.

2.2. Estimation of the Structure Damping. It is common practice to use free-damping data to verify FEA (finite

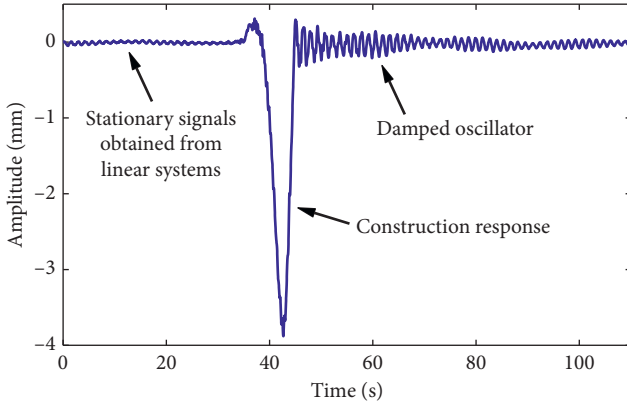


FIGURE 1: The decomposition of the measurement signal (reproduced from [24], under the Creative Commons Attribution-NonCommercial 4.0 International License).

element analysis) models. Usually, data are used to obtain information about the amplitude spectra (Figure 2). In order to correctly establish an amplitude spectrum, the incoming signal must be processed with a band-pass filter supported by data and a precalculated modal analysis based on the finite elements analysis method. The interval representing free vibration may be presented as follows:

$$x(t) = Ae^{-Bt} \cos(\omega t + \varphi), \quad (1)$$

where A is the amplitude, B is the damping coefficient, ω is the frequency, φ is the phase, and t is the time.

If a Hilbert transform was calculated for such a signal, the envelope of the damped oscillator was obtained as a result (Figure 3).

Taking into account equation (1), the estimated parameter B may be calculated in the following two ways:

- (i) Directly from the definition by fitting the exponential function into the result of the Hilbert transform
- (ii) By fitting the linear function into the logarithm of the Hilbert transform

A classic logarithmic decrement of damping is calculated upon the basis of the following equation:

$$\delta = \ln \frac{A_n}{A_{n+1}}, \quad (2)$$

where δ is the logarithmic decrement of damping and A_n and A_{n+1} are the consecutive amplitudes.

The direct use of equation (2) does not solve the problem, which is illustrated in Figure 3. Although the band-pass filter is used, the signal, which registers the free vibration, is affected by two very similar frequencies because the phenomenon of beat frequencies occurs in bridge structures while being tested. Such a situation is found on bridge structures, especially for cable bridges [10, 25, 26]. The proposed solution of this occurrence is superior to the classical method based upon the definition of the logarithmic decrement of damping that, in the submitted example, the estimation of the damping coefficient is not

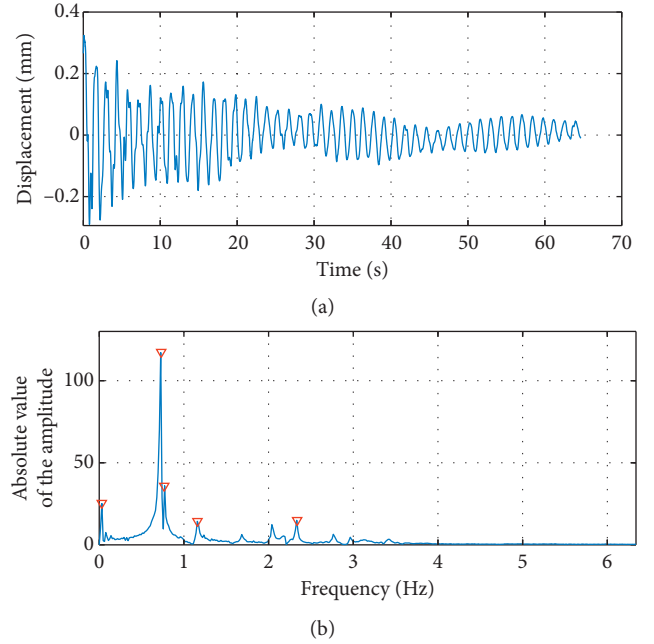


FIGURE 2: Example of time series and its amplitude spectrum (reproduced from [24], under the Creative Commons Attribution-NonCommercial 4.0 International License).

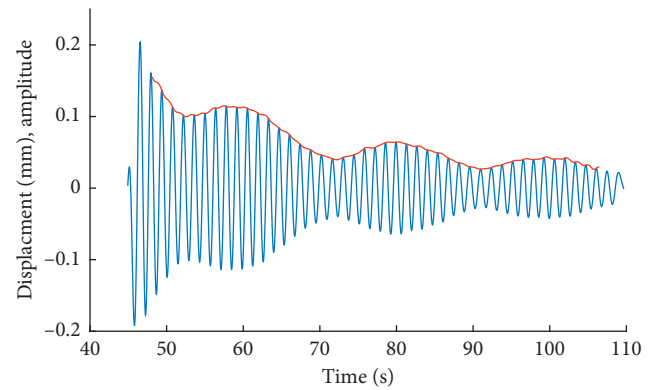


FIGURE 3: Hilbert transform calculated for signal obtained from damping vibrations with beat frequencies (reproduced from [24], under the Creative Commons Attribution-NonCommercial 4.0 International License).

hampered by the errors occurring from the number of frequency components (Figure 4).

The standard equation describing the vibration is exponential. It is by its nature difficult to be analyzed by regression algorithms. The proposed solution is based on linearizing the equation before estimating the parameters. The logarithmic representation of the Hilbert transform can be easily estimated using linear regression or generalized linear regression with selected cost function (the authors present the use of LSF as a cost function). It is a more effective way and a more robust solution.

Such an approach allows for the estimation of the damping coefficients to be based on a robust estimation. In addition, while the estimation is being determined, the entire

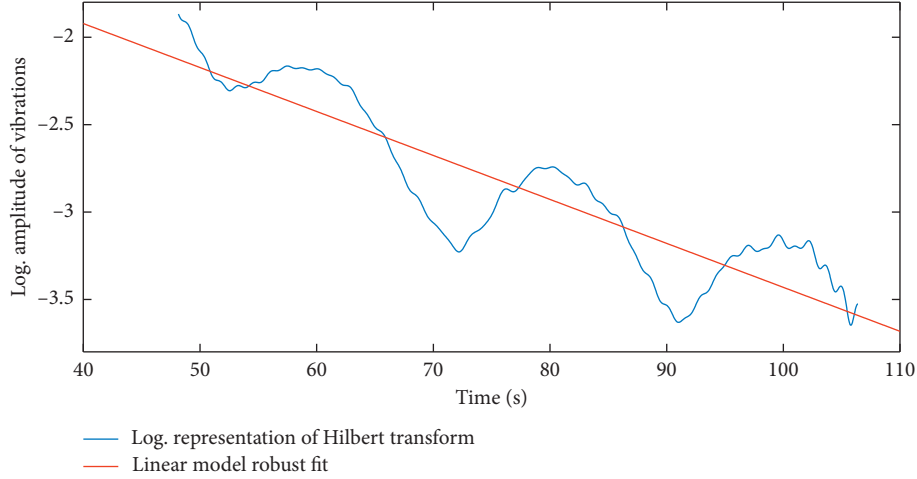


FIGURE 4: Logarithmic representation of Hilbert transform (blue) and linear estimation (red) (reproduced from [24], under the Creative Commons Attribution-NonCommercial 4.0 International License).

data acquisition of the measuring signal is being utilized, rather than an arbitrarily chosen amplitude (Figure 4). Therefore, after determining the linear estimation,

$$y = Bx + C, \quad (3)$$

$$\delta = B \cdot T, \quad (4)$$

where T is the period of the dampened vibration and C is the constant.

2.3. Structural Health Estimation and Damage Detection. If during a load test, damage to the construction occurred, it would change the statistical characteristics of the measured data. There exists a group of methods which has been developed for the identification of the damage. They are based on the congruency of the ARMA (autoregressive moving average) models into the given data. The general form is as follows:

$$x_{ij}(t) = \sum_{k=1}^p a_k x_{ij}(t-k) + \sum_{k=1}^q b_k \varepsilon_{ij}(t-k) + \varepsilon_{ij}(t), \quad (5)$$

where $x_{ij}(t)$ is the normalized measurement signal, a_k and b_k are the k -th AR and MA coefficients, p and q are the model orders of the AR and MA processes, and $\varepsilon_{ij}(t)$ is the residual term.

The algorithms of the group are discussed in detail [10, 19, 20]. In particular, the modified and implemented algorithm adapts to the structure in Figure 5.

The structure of the proposed algorithm is discussed in more detail below. The assumption is to answer the question whether the condition of the structure before the vehicle's approach during the loading of the bridge structure and after that has changed. The algorithm operates on data portions—called batch or data intervals. Batch data processing is an efficient way of processing high volumes of data where a group of transactions is collected over a period of time. Data are collected, entered, and processed, and then the results are produced. Since we would like to be able to compare the

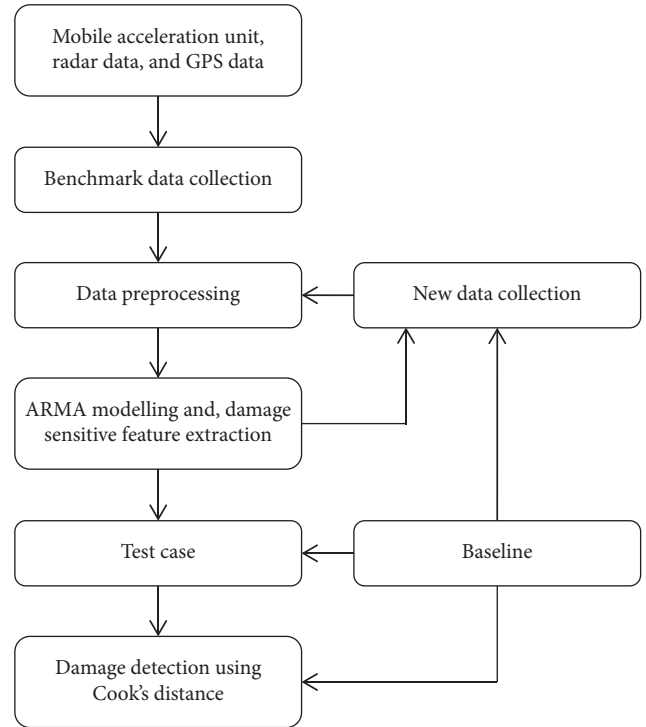


FIGURE 5: Selected and implemented ARMA algorithm framework.

results between measurements, the intervals of the data must be standardized in the beginning of the process, as is shown in Figure 5. A practical way of doing this is as follows:

$$\bar{x}(t) = \frac{(x(t) - m)}{\sigma}, \quad (6)$$

where $x(t)$ is the analyzed interval (batch of data), m is the mean value, and σ is the standard deviation.

After the standardization, the time series is entered into the model of ARMA in accordance with equation (5). Taking into consideration the different types of engineering structures, the rank of the coefficients AR (p) and MA (q), in the proposed solution, is subject to estimation.

Therefore, the effect of the action of the algorithm will be the result of the damage sensitive feature of the DSF parameters calculated for the specific data vectors representing the engineering structure before and after the potential damage (Figure 6):

$$\text{DSF} = \frac{a_1}{\sqrt{a_1^2 + a_2^2 + a_3^2}}, \quad (7)$$

where a_i is the coefficients obtained from equation (5).

The classical approach to identify the damage in a given structure is that one must take all the obtained DSF coefficients prior to the test (marked in Figure 6 as circles) and use this as a basis to calculate the estimated value. The next step would be an analogical procedure for the entire interval representing the structure behavior after the excitation has been applied to the construction (the result is marked in Figure 6 as plus signs).

Hence, for both groups of data, the mean values have to be estimated. Upon this basis, it may be concluded that there will be a substantial difference between the groups, using the standard t -test for this aim.

This type of approach has two characteristic shortcomings:

- (1) It is crucial to take a sufficient number of samples representative of the structures behavior after force has been applied to the construction, in order for the statistical significance from the given test to be properly kept at accordingly a high level.
- (2) Limiting the possibility of using the calculation techniques of bridge structures while under operation being subjected to continual use, there may not be a suitable length of time between the impact of the structure to gather the proper amount of data to run a t -test determining the DFS coefficients.

2.4. Reducing the Amount of the Necessary Data. The abovementioned limitations may be solved by using a different criterion than the statistical difference estimated between the two groups of data. A dataset was considered in which after the excitation and damping of the object and before the next excitation, a limited amount of data can be registered. It means that two consecutive forces are applied to the structure in a short time. In the case of such data, it is possible to calculate a limited number of the DSF coefficients (in Figure 7 marked with an arrow).

Such a situation may be encountered when research is being carried out in bridge structures that are in current use, especially those with a large variety of vehicles that are not standard and are oversized. The question at hand is whether or not a given vehicle may be the cause of damage to a structure even during minimal intervals between the impacts.

In order to verify whether the limited number of DSF parameters that were registered are significantly different from the average realization, the formula that may be used in such a regression analysis is based upon Cook's distance given by the following equation:

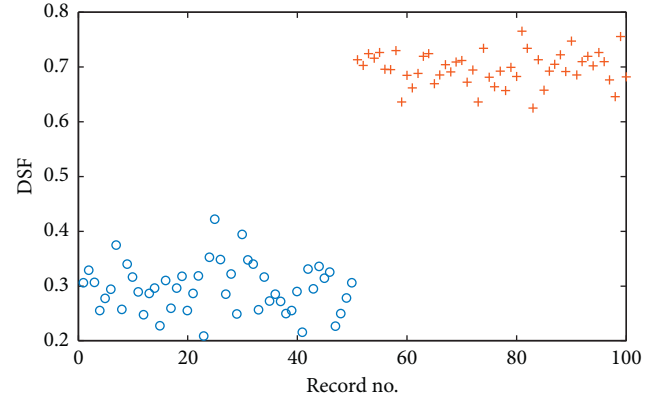


FIGURE 6: DSF obtained from example data (reproduced from [24], under the Creative Commons Attribution-NonCommercial 4.0 International License).

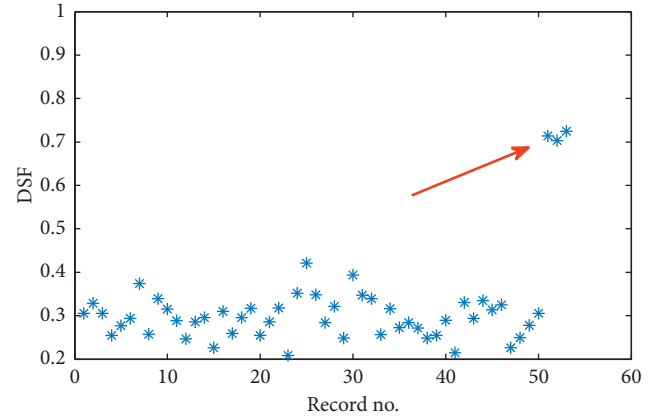


FIGURE 7: DSF obtained from object with limited data after extraction (reproduced from [24], under the Creative Commons Attribution-NonCommercial 4.0 International License).

$$D_i = \frac{\sum_{j=1}^n (y_j - y_{j(i)})^2}{p \cdot \text{MSE}}, \quad (8)$$

where y_j is the j -th fitted response value, $y_{j(i)}$ is the j -th fitted response value where the fit does not include observation i , MSE is the mean squared error, and p is the number of coefficients in the regression model.

There are several reasons why Cook's distance has been chosen as a tool to detect changes in the DSF coefficients value. First of all, the use of this method allows for the diagnosis of the object's state immediately after the load has been removed which is crucial for the algorithm. Thus, the potential damage to a bridge object can be detected on the basis of a small amount of data. Second, there are unambiguous, objective criteria for assessing whether Cook's persistence is statistically significant [27]. Thirdly, it is not necessary to perform recursive statistical significance tests of the DSF coefficients, which significantly reduces computational complexity.

Figure 8 presents Cook's distances calculated for the example dataset. It is easy to see that all of the captured DSF

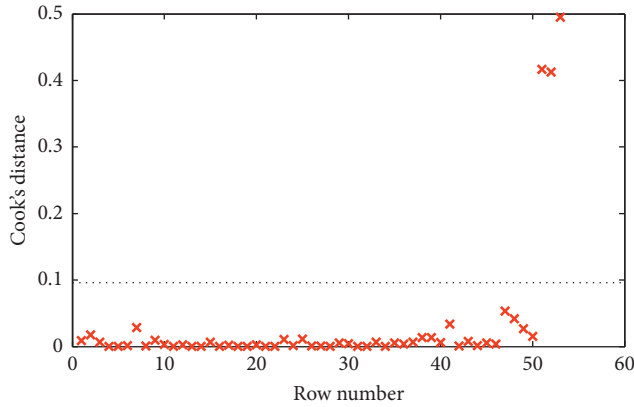


FIGURE 8: Cook's distance calculated for the linear model of DSF coefficients [24] (reproduced from [24], under the Creative Commons Attribution-NonCommercial 4.0 International License).

coefficients for the vectors of the data representing a damaged structure are assigned a value above line.

The dashed line in Figure 8 corresponds to the recommended threshold value of three times the mean of Cook's distance. The plot has observations with Cook's distance values which are greater than the threshold value. In particular, the DSF obtained for vector numbers 51, 52, and 53 have Cook's distance values that are relatively higher than the others, which exceed the threshold value. Usually you might want to find and omit these from your data and rebuild your model, but in our case, this information is used to answer the question if extraction (for example, a vehicle) caused damage to the tested bridge. It is important to keep in mind that this is not the value of Cook's distance, but the change in the value of the DSF coefficient is the basis for identifying the damage to the object. Cook's distance is only a tool that allows you to objectively and efficiently find changes in the DSF value.

3. Bridge Test Results

3.1. Acquisition of the Observation Data. The object on which the test was carried out was a tram viaduct. The ground-based interferometric radar IBIS-S was used to acquire the data (Figure 9). The displacements of a dozen points representing the bridge span were the subject of measurement; however, the observations of one point, located in the span half-length, were used for further analyzes. The sampling frequency was set as 100 Hz.

The design specifications on the phase accuracy applied on the radar system, which was used in the presented research, are suitable for measuring short-term displacements with a range accuracy better than 0.1 mm [28]. Moreover, the radar manufacturer claims that displacement surveying accuracy is at the level of 0.01 mm. This value is confirmed by the analyses carried out by Rödelsperger [29], who consider the relationship between the SNR (signal to noise ratio) and the displacement measurement error. The SNR value depends on the intensity of the radar signal reflected by the observed object. For an SNR of 40 dB, the displacement measurement error is 0.03 mm and decreases with a further



FIGURE 9: IBIS-S radar unit under the tested bridge span.

increase of SNR. The time series subjected to further analysis was recorded for one of the 7 points observed on the bridge span, and for all of them, the SNR was greater than 65 dB.

In the conducted research, it was assumed that the impact of the atmospheric disturbance and the multipath signal effect is negligible. This is possible because, during the observation, the atmospheric conditions did not change and the configuration of the measurement system and the object remained unchanged. In addition, taking into account the fact that the precision of the measurement result is more important to the performed tests than its accuracy, it may be assumed that the record of 0.01 mm displacement is an actual observation.

The time series subjected to further analysis is shown in Figure 10. The data representing the stationary signal are marked in red. They provide input data for the proposed algorithm for potential damage detection. With the use of arrows, the intervals of clear excitation of the free vibrations are marked, which will be used to determine the frequency spectrum of the construction vibrations and the logarithmic decrement of damping.

In the proposed algorithm, the frequency spectrum analysis is not a key but an auxiliary element of the solution. The essence of the algorithm is based on the transformations of stationary signals. However, the proposed application of the method is monitoring bridges that will be subjected to vehicle traffic. Therefore, in order to correctly analyze the data, it is necessary to verify when after the excitation the construction vibration has been damped.

To determine the parameters of damping the structure, the observation intervals marked with arrows were used (Figure 10). The selected observation intervals were subjected to FFT analysis. Both of the analyzed cases showed a dominant frequency of value $2.95 \text{ Hz} \pm 0.01 \text{ Hz}$. This means that the natural vibration period of the tested bridge span is $T = 0.34 \text{ s}$.

According to the proposed algorithm, the Hilbert transform was used to determine the damping of the structure. The signal from the observation is marked in blue, while the envelope of the vibration (i.e., the graph of the Hilbert transform) is shown in red (Figure 11).

Then, in the logarithmic representation of the Hilbert transform, the linear function was fitted (Figure 12). The determined value of parameter B defined in equation (3) is

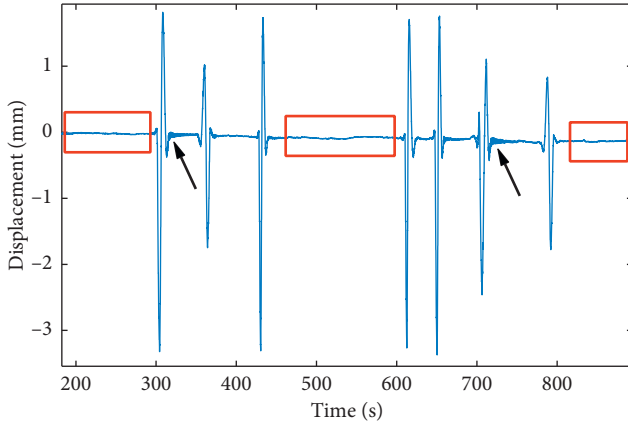


FIGURE 10: Data input for time-series-based damage detection algorithm (searching for stationary signals using selected parameters of object damping).

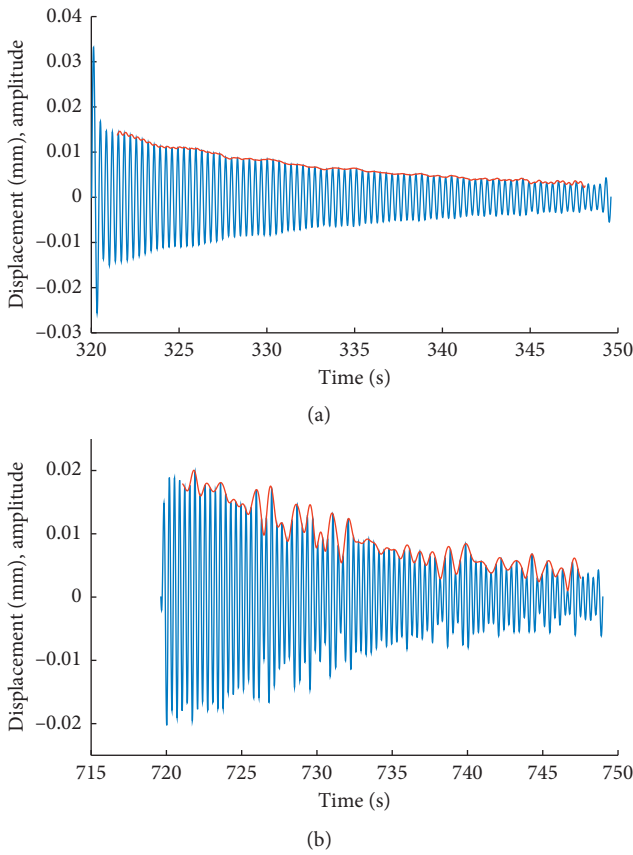


FIGURE 11: Hilbert transform of selected intervals.

0.0572 and 0.0646 for the analyzed cases. This means that the logarithmic decrement of damping equals 0.019 and 0.022, respectively.

3.2. Optimization of Algorithm Parameters. The algorithm of the structure damage detection based on the autoregressive moving average model has several parameters that can be adjusted adequately to the analyzed building objects. Among

them are the p and q values, that is, the model orders of the AR and MA processes can be pointed out. In addition, the length of the vector containing the data to determine the DSF parameter is also not strictly defined, the same as the number of these vectors. Hence, for the analyzed case, an attempt was made to determine the optimal AR and MA values (Figures 13 and 14, respectively).

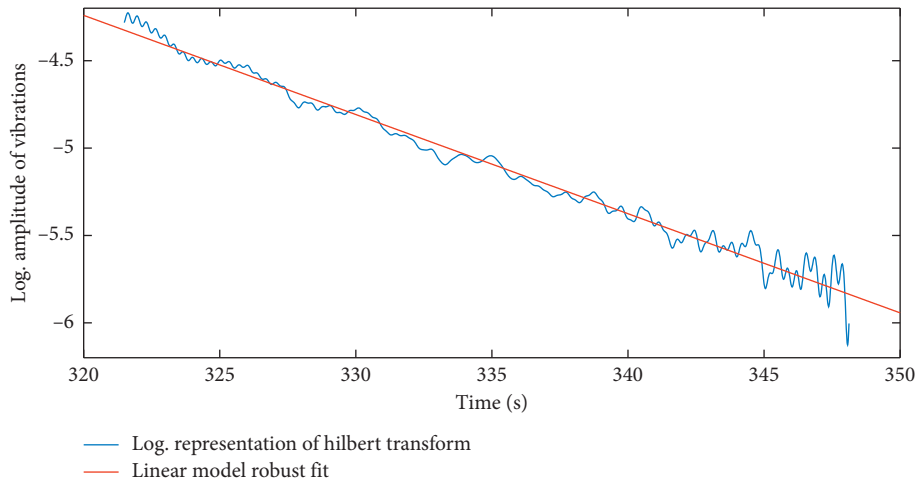
In the following figures, different symbols were used for marking the DSF values obtained as a result of the analysis of the signal recorded before the occurrence of the load and after the load termination and related effects (like the damped vibrations). The solid lines in the corresponding colors represent the regression lines fitted into the set of DSF values determined for the adopted number of the analyzed data vectors.

The values of the model orders of the AR and MA processes have a range that makes them appropriate for the analysis [21]. The presented variants allow the choice of $p = 4$ and $q = 3$ as optimal for further analysis. And while the q parameter does not significantly affect the DSF values ($q = 3$ was chosen for further analysis), in the case of parameter p , the differences are significant. The choice of $p = 4$ for further analysis is due to the smallest variability of the DSF value (the black markers in Figure 13) in relation to the time series from the observation of the structure before the load occurrence, i.e., the potential damage.

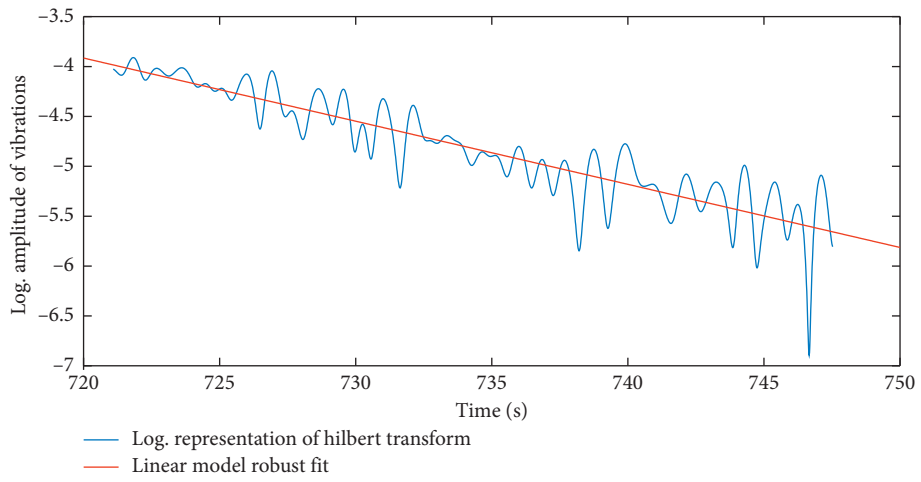
In the next stage, the effect of the length of the vector containing the data to determine the DSF parameter and the number of analyzed vectors was verified. Observation data were divided into two ways: (1) 21 vectors with 200 elements and (2) 11 vectors with 400 elements (Figure 15). The results indicate a higher sensitivity of the variant (1); however, the variant (2) also reveals that the values are significantly different from the average. This is important in the process of detecting changes in the state of the structure. The advantage of variant (2) is the higher calculation speed.

3.3. Application of Cook's Distance. In the proposed algorithm, Cook's distance was used to determine if the implementation of a limited number of DSF parameters are significantly different from the average realization. The analyses were made on the basis of the DSF datasets, as shown in Figure 15. The effect is shown in Figure 16. The DSF values exceeding the adopted threshold (the dashed lines in Figure 16), i.e., the outliers, are marked with red circles.

It should be noted that the DSF values that would indicate a change of the structure state (vectors no. 9–13 in Figure 15(a) or vector no. 6 in Figure 15(b)) are not confirmed by the calculated Cook's distance. On the contrary, there can also occur outliers (the black cross in Figure 16(b)) which do not indicate damage on the basis of the DSF. This leads to the conclusion that the detection of structural damage should be based not only on the DSF coefficient but also on Cook's distance, which is its valuable complement in the proposed algorithm. The proposed algorithm has an advantage over a standard solution because it is not based on simple statistical significance testing of the DSFs. As a result, the size of the sample before and after the load can vary.



(a)



(b)

FIGURE 12: Logarithmic representation of Hilbert transform.

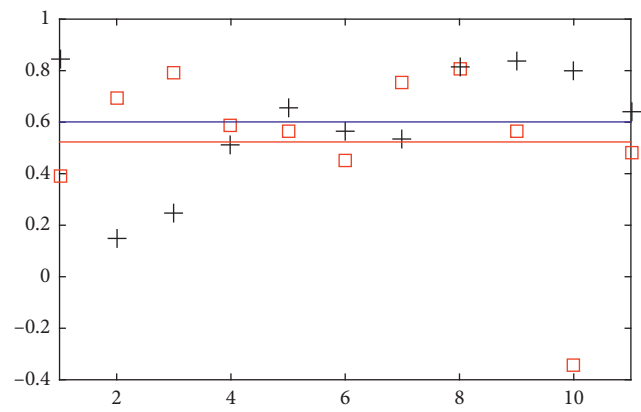
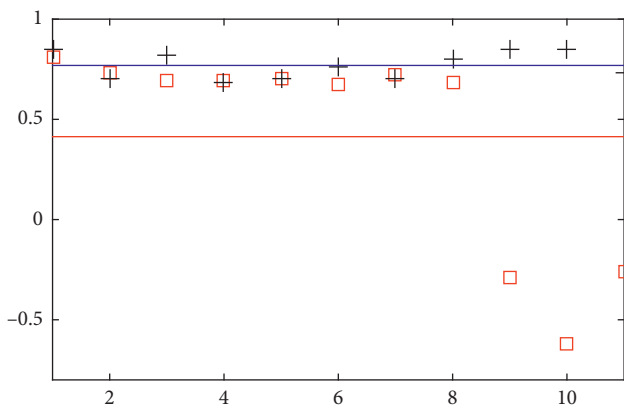


FIGURE 13: Continued.

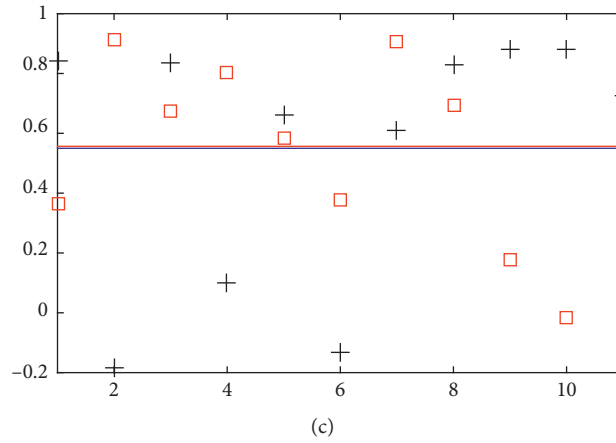


FIGURE 13: Distribution of DSF values depending on the AR process order: (a) version order of AR = 4, order of MA = 3; (b) version order of AR = 5, order of MA = 3; (c) version order of AR = 6, order of MA = 3.

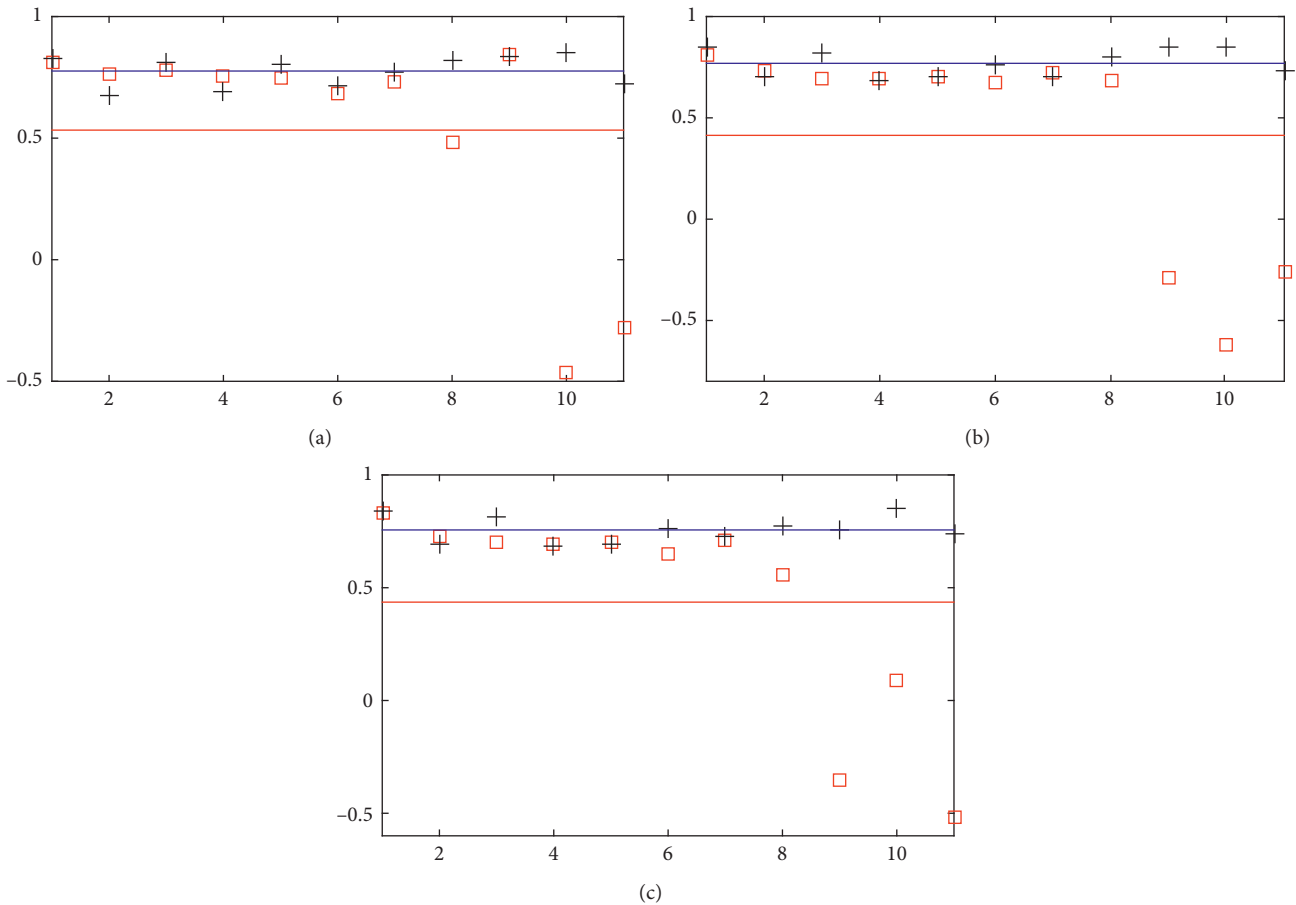


FIGURE 14: Distribution of DSF values depending on the MA process order: (a) version order of AR = 4, order of MA = 2; (b) version order of AR = 4, order of MA = 3; (c) version order of AR = 4, order of MA = 4.

It also does not matter what the distribution of the residuals is (there is no need to meet the assumptions related to a formal significance test). In the examples discussed, the values of the DSF coefficients signaling object damage are unlikely to be detected by another method. Thanks to this, the proposed method is not only faster but also more sensitive.

4. Conclusions

The presented algorithm comprehensively discusses the methods of prototyping engineering structures, in particular, examining bridges under testing and operational loads. Its basic assumptions and features are the following:

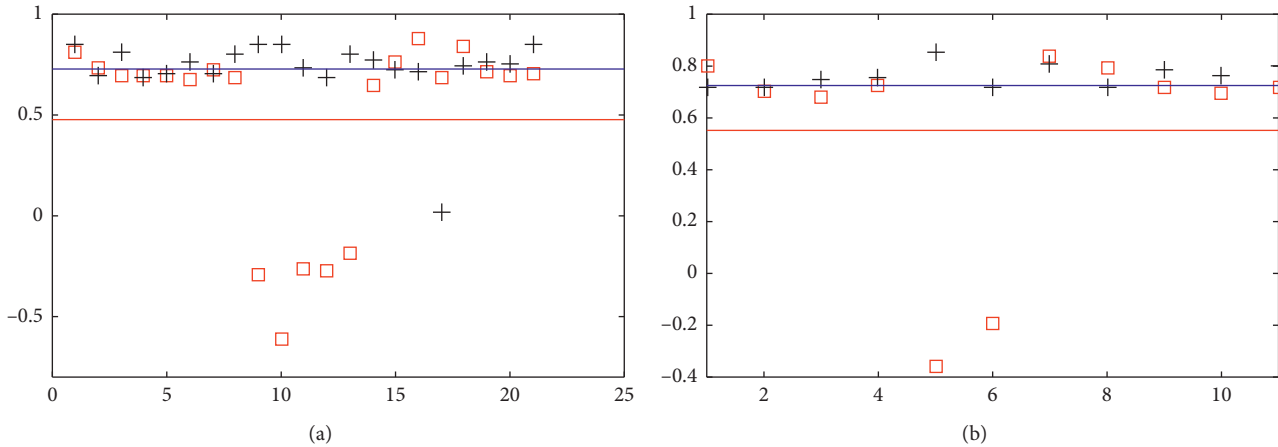


FIGURE 15: Analyzed cases of vector length: (a) version order of AR=4, order of MA=3; (b) version order of AR=4, order of MA=3.

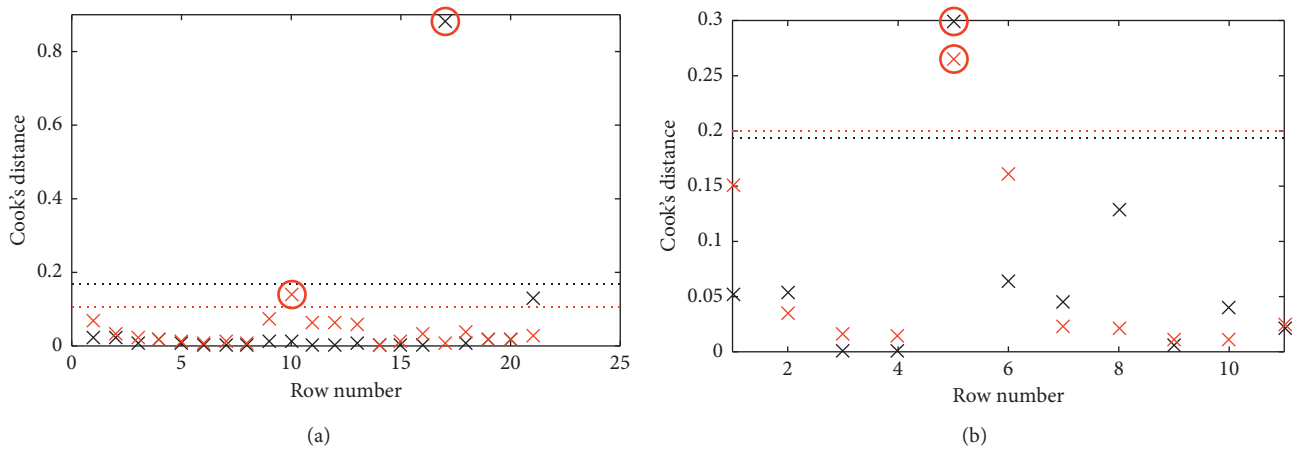


FIGURE 16: Distribution of the DSF values depending on the order of the MA process.

- (1) The decomposition of the recorded signal represents the vibration of a given bridge structure into three groups in the time domain. The first group contains data before an impact and after free vibration, and technically, it is the group of stationary signals of linear systems. The second group is the response of the construction (i.e., the deflection of the span occurred). The third group is the part of the signal which represents the free vibration in a structure that is excited.
- (2) The decomposition of a signal in a frequency spectrum, especially with band-pass filters, allows for the more effective spectral analysis. The band width is the results of the FEM analysis.
- (3) The amplitude spectrum is comparable to the analysis made with the finite elements method through the calculation of the fast Fourier transform.
- (4) Construction damping of an object is represented by the logarithmic decrement. The calculation of its values is not dependent upon the implementation of the direct definition but on the calculation of the

Hilbert transform. Furthermore, for the logarithm of the envelope, the linear regression with the robust least squares fitting method is calculated. The calculated coefficients of the linear estimation allow for an estimation of logarithmic decrement of damping in the entire signal, even when the structure experiences beat frequencies.

- (5) The identification of the potential damage to a structure as a result of impact is based on the DSF coefficients. The answer to the question if the damage occurred is based on Cook's distance rather than the comparison of the average values of the tests is obtained as follows: the effect of such an examination is when in real time the conclusion may be drawn whether or not the data from the tested object indicate the damage, even in the cases when the damage occurs during the operation of the tested object.

It is of utmost importance that the data supporting the algorithm in the field of stationary signals are analyzed properly. The important parameters are as follows: the order

of the ARMA model, the length of the data windows, and the test if the residuals obtained are normal, impeded, and identically distributed. Verification of the construction condition has to be based on the proper baseline (the same environmental conditions). In addition, the proposed solution presents current and modern approaches to solving the problem. In particular, it offers the following:

- (i) The effective separation of stationary and non-stationary signals
- (ii) Optimal ARMA model parameters
- (iii) Implementation possibilities supporting online solutions by limiting computational complexity
- (iv) Effective input data for the analyzes conducted using the AI method, in particular for classifying the DSF parameters and Cook's distances assigned to them
- (v) A methodology of using Hilbert transforms for oversize excitations
- (vi) The use of observation methods based on interferometric radars, which facilitate the location of potential damage, because the input data are uniform in the time domain and strictly defined to the location; due to the easy coverage of the tested object with multiple observations, the analysis of data, and consequently the location of the damage, is easier
- (vii) Input data from radar systems which allow, due to the frequency and accuracy of the displacement measurements, the use of the most algorithms that were developed for the analysis of the measurements performed with the accelerometers
- (viii) No influence of weather conditions variability on the possibility of inference about the state of the object for the dynamic issues.

Further research is the technological implementation of machine learning which will allow for the automatic classification of the DSF coefficients.

Data Availability

The PDF data used to support the findings of this study are included within the supplementary information file(s).

Conflicts of Interest

The authors declare that there are no conflicts of interest regarding the publication of this paper.

Acknowledgments

This publication was prepared within statutory research fund no. 11.11.150.005 of the Department of Engineering Surveying and Civil Engineering, Faculty of Mining Surveying and Environmental Engineering of AGH University of Science and Technology in Kraków.

Supplementary Materials

Raw radar measurement data have been provided as a supplementary material in the form of a PDF file. (*Supplementary Materials*)

References

- [1] V. Gikas, "Ambient vibration monitoring of slender structures by microwave interferometer remote sensing," *Journal of Applied Geodesy*, vol. 6, no. 3-4, pp. 167–176, 2012.
- [2] C. Gentile and G. Bernardini, "Output-only modal identification of a reinforced concrete bridge from radar-based measurements," *NDT & E International*, vol. 41, no. 7, pp. 544–553, 2008.
- [3] R. C. Barros and F. M. Paiva, "On the use of radar interferometry for the structural monitoring of bridges," in *Proceedings of the 6th International Conference Integrity-Reliability-Failure (IRF2018)*, pp. 1287–1300, Lisbon, Portugal, July 2018.
- [4] M. Diaferio, A. Fraddosio, M. D. Piccioni, A. Castellano, L. Mangialardi, and L. Soria, "Some issues in the structural health monitoring of a railway viaduct by ground based radar interferometry," in *Proceedings of the IEEE Workshop on Environmental, Energy, and Structural Monitoring Systems (EESMS)*, pp. 1–6, IEEE, Milan, Italy, July 2017.
- [5] P. Kohut, K. Holak, T. Uhl et al., "Monitoring of a civil structure's state based on noncontact measurements," *Structural Health Monitoring: An International Journal*, vol. 12, no. 5-6, pp. 411–429, 2013.
- [6] J. Hu, J. Guo, L. Zhou, S. Zhang, M. Chen, and C. Hang, "Dynamic vibration characteristics monitoring of high-rise buildings by interferometric real-aperture radar technique: laboratory and full-scale tests," *IEEE Sensors Journal*, vol. 18, no. 15, pp. 6423–6431, 2018.
- [7] A. Castellano, A. Fraddosio, F. Martorano, G. Mininno, F. Paparella, and M. D. Piccioni, "Structural health monitoring of a historic masonry bell tower by radar interferometric measurements," in *Proceedings of the IEEE Workshop on Environmental, Energy, and Structural Monitoring Systems (EESMS)*, pp. 1–6, IEEE, Salerno, Italy, June 2018.
- [8] F. X. Ochieng, C. M. Hancock, G. W. Roberts, and J. Le Kernec, "A review of ground-based radar as a noncontact sensor for structural health monitoring of in-field wind turbines blades," *Wind Energy*, vol. 21, no. 12, pp. 1435–1449, 2018.
- [9] C. R. Farrar and K. Worden, *Structural Health Monitoring. A Machine Learning Perspective*, John Wiley & Sons, Chichester, UK, 2013.
- [10] H. Wenzel, *Health Monitoring of Bridges*, John Wiley & Sons, Chichester, UK, 2009.
- [11] A. Vetrivel, M. Gerke, N. Kerle, F. Nex, and G. Vosselman, "Disaster damage detection through synergistic use of deep learning and 3D point cloud features derived from very high resolution oblique aerial images, and multiple-kernel-learning," *ISPRS Journal of Photogrammetry and Remote Sensing*, vol. 140, pp. 45–59, 2018.
- [12] D. Feng and M. Q. Feng, "Computer vision for SHM of civil infrastructure: from dynamic response measurement to damage detection—a review," *Engineering Structures*, vol. 156, pp. 105–117, 2018.
- [13] L. Long, S. Thöns, and M. Döhler, "The effects of SHM system parameters on the value of damage detection information," in

- Proceedings of the 9th European Workshop on Structural Health Monitoring (EWSHM)*, pp. 1–10, Manchester, UK, July 2018.
- [14] Y.-L. Zhou, N. M. Maia, and M. Abdel Wahab, “Damage detection using transmissibility compressed by principal component analysis enhanced with distance measure,” *Journal of Vibration and Control*, vol. 24, no. 10, pp. 2001–2019, 2018.
- [15] B. Zhang, Y. Qian, Y. Wu, and Y. B. Yang, “An effective means for damage detection of bridges using the contact-point response of a moving test vehicle,” *Journal of Sound and Vibration*, vol. 419, pp. 158–172, 2018.
- [16] J. Huang, D. Li, H. Li, G. Song, and Y. Liang, “Damage identification of a large cable-stayed bridge with novel cointegrated Kalman filter method under changing environments,” *Structural Control Health Monitoring*, vol. 25, no. 5, article e2152, 2018.
- [17] B. Bhowmik, M. Krishnan, B. Hazra, and V. Pakrashi, “Real-time unified single- and multi-channel structural damage detection using recursive singular spectrum analysis,” *Structural Health Monitoring*, vol. 18, no. 2, pp. 536–589, 2018.
- [18] T. B. Roy, S. Banerji, S. K. Panigrahi, A. Chourasia, L. Tirca, and A. Bagchi, “A novel method for vibration-based damage detection in structures using marginal Hilbert spectrum,” in *Recent Advances in Structural Engineering, Vol 1*, A. Rao and K. Ramanjaneyulu, Eds., vol. 11, pp. 1161–1172, Lecture Notes in Civil Engineering, Springer, Berlin, Germany, 2019.
- [19] M. Krishnan, B. Bhowmik, B. Hazra, and V. Pakrashi, “Real time damage detection using recursive principal components and time varying auto-regressive modeling,” *Mechanical Systems and Signal Processing*, vol. 101, pp. 549–574, 2018.
- [20] H. Sohn, C. Farrar, H. Hunter, and K. Worden, “Applying the LANL statistical pattern recognition paradigm for structural health monitoring to data from a surface-effect fast patrol boat,” Technical Report LA-13761-MS, Los Alamos National Laboratory, Los Alamos, NM, USA, 2001.
- [21] K. K. Nair, A. S. Kiremidjian, and K. H. Law, “Time series-based damage detection and localization algorithm with application to the ASCE benchmark structure,” *Journal of Sound and Vibration*, vol. 291, no. 1-2, pp. 349–368, 2006.
- [22] K. Shin and J. K. Hammond, *Fundamentals of Signal Processing for Sound and Vibration Engineers*, John Wiley & Sons, Chichester, England, 2008.
- [23] G. E. P. Box and D. A. Pierce, “Distribution of residual autocorrelations in autoregressive-integrated moving average time series models,” *Journal of the American Statistical Association*, vol. 65, no. 332, pp. 1509–1526, 1970.
- [24] T. Owerko, “Method of prototyping sensitive dynamic engineering structures supporting automatic information identification regarding a structure’s condition,” *Journal of Civil Engineering and Architecture*, vol. 10, no. 8, pp. 912–918, 2016.
- [25] Ž. Nakutis and P. Kaškonas, “Bridge vibration logarithmic decrement estimation at the presence of amplitude beat,” *Measurement*, vol. 44, no. 2, pp. 487–492, 2011.
- [26] T. Owerko, “Beat frequency detection of bridges using ground-based radar interferometry,” *Measurement Automation Monitoring*, vol. 60, no. 11, pp. 1065–1068, 2014.
- [27] R. D. Cook, “Influential observations in linear regression,” *Journal of the American Statistical Association*, vol. 74, no. 365, pp. 169–174, 1979.
- [28] M. Pieraccini, M. Fratini, F. Parrini, G. Macaluso, and C. Atzeni, “High-speed CW step-frequency coherent radar for dynamic monitoring of civil engineering structures,” *Electronics Letters*, vol. 40, no. 14, pp. 907–908, 2004.
- [29] S. Rödelsperger, “Real-time processing of ground based synthetic aperture radar (GBSAR) measurements,” in *Schriftenreihe Fachrichtung Geodäsie*, no. 33, Fachbereich Bauingenieurwesen und Geodäsie, Technische Universität Darmstadt, Darmstadt, Germany, 2011.

Research Article

Operational Deflection Shape Extraction from Broadband Events of an Aircraft Component Using 3D-DIC in Magnified Images

Ángel J. Molina-Viedma ¹, Elías López-Alba,¹ Luis Felipe-Sesé ²,
and Francisco A. Díaz ¹

¹Departamento de Ingeniería Mecánica y Minera, Campus Las Lagunillas, Universidad de Jaén, 23004 Jaén, Spain

²Departamento de Ingeniería Mecánica y Minera, Campus Científico Tecnológico de Linares, Universidad de Jaén, 23700 Linares, Spain

Correspondence should be addressed to Ángel J. Molina-Viedma; ajmolina@ujaen.es

Received 30 November 2018; Revised 12 February 2019; Accepted 5 March 2019; Published 9 April 2019

Academic Editor: Nuno M. Maia

Copyright © 2019 Ángel J. Molina-Viedma et al. This is an open access article distributed under the Creative Commons Attribution License, which permits unrestricted use, distribution, and reproduction in any medium, provided the original work is properly cited.

Recently, many works have shown the capabilities of noninterferometric optical techniques, such as digital image correlation, to characterise modal behaviour. They provide a global insight into the structure or component behaviour which implies massive spatial information, unaffordable by traditional sensor instrumentation. Moreover, phase-based motion magnification (PMM) is a methodology which, based on a sequence of images, magnifies a periodic motion encoded in phase time-domain signals of the complex steerable pyramid filters employed to decompose the images. It provides a powerful tool to interpret deformation. However, the interpretation is just qualitative and should be avoided if out-plane motion is recorded as only one camera is employed. To overcome this issue, 3D digital image correlation (3D-DIC) has been linked with PMM to provide measurements from stereoscopic sets of images, providing full-field displacement maps to magnified images. In this work, the combination of PMM and 3D-DIC has been employed to evaluate the modal behaviour of an aircraft cabin under random excitation. The study was focused on the passenger window area due to its significance to the structural integrity as a discontinuity of the peel. Operational deflection shapes at different resonances were characterised by magnifying a single resonance in the spectrum and then measuring with 3D-DIC. These measurements were validated with those obtained in forced normal mode tests. Motion and displacement videos improved the understanding of the identified resonance deformation. Actually, a relevant behaviour was noticed in the window's frame, a quite narrow area where using traditional sensors would not provide such a detailed 3D information.

1. Introduction

Structural integrity of aircraft is a vital issue. These structures undergo strict controls under severe conditions to provide safety and excellent dynamic performance. Many efforts are taken during design and validation stages in prediction with powerful numerical simulations and expensive, challenging experimental measurements, respectively. Modal parameter inspection is a typical way to detect damage or abnormal behaviour and also to characterise the generated noise inside the cabin. Experimentally, the instrumentation of big

structures is usually sparse to prevent the cost increasing. Hence, low spatial resolution provides a rough characterisation regarding mode shapes or even missed due to spatial aliasing. Especially, the resolution is not enough to understand the behaviour of small critical areas. In this sense, full-field optical techniques offer an ultrahigh spatial resolution compared to pointwise methods and, thanks to high speed cameras, represent an interesting alternative for modal identification. Digital image correlation (DIC) [1] is one of the most popular methods due to its robustness, well-developed methodology, and user-friendly commercial

software. But the main advantage over most of the techniques is the possibility of performing 3D measurements by setting up a calibrated stereovision system of two or more cameras. Different studies have explored 3D-DIC for modal identification [2–5]. In a previous work, the authors evaluated the effect of differential pressure on the modal behaviour of aircraft using 3D-DIC [6]. These studies proved the capabilities of the technique to determine full-field mode shapes, avoiding any spatial aliasing.

An interesting methodology recently developed is phase-based motion magnification (PMM). It is a new Eulerian approach to motion processing developed by Wadhwa et al. [7]. It is intended to reveal subtle motion in videos by obtaining a magnified version. The video signals are decomposed using complex steerable pyramid filters [8–10]. This is an overcomplete transform based on complex sinusoids modulated by a Gaussian window function at different spatial scales, orientations, and positions. The time-domain local phase at every spatial scale and orientation of a steerable pyramid, where the motion is encoded, is temporally band-pass filtered and amplified by a magnification factor. When images are reconstructed back, the result is the magnification of the harmonic motion in that frequency band. This method is advantageous over the previous linear amplitude-based Eulerian magnification method [11] since it is possible to achieve larger amplitudes without distortion. Moreover, it provides substantially better noise performance since there is no increment of spatial noise amplitude. This methodology has been employed by Chen et al. to describe operational deflection shapes (ODS) under forced normal mode tests using the edge detection algorithm to highlight the magnified shapes [12]. Sarrafi et al. [13] also employed the edge detection on magnified images for damage detection by noticing changes in natural frequencies and ODSs. PMM has also been employed to develop an autonomous methodology for experimental modal analysis with a little user supervision [14, 15]. Natural frequency and damping are determined from phase signals under random excitation, whereas mode shapes were magnified and highlighted using the edge detection. This methodology has been employed for damage detection localisation using fractal dimension [16].

That is very valuable; however, numerical information or quantifying the motion in terms of displacement is not available. To achieve this, the authors developed a methodology to measure the magnified images using 2D-DIC under sinusoidal excitation to determine displacements in the sensor plane [17]. This demonstrated to be beneficial to provide a full-field measurement to magnified images. In addition, it improved the quality of the ODSs measurement due to the larger motion, considering the typical limitations of DIC for low-amplitude vibrations. Nevertheless, the mentioned phase-based methodologies and also the combination with 2D-DIC employ a system with a single camera. It is only suitable to visualise in-plane motions and, thus, only for 2D displacements. Considering that, the authors evaluated the validity of the measurement on magnified images from a stereoscopic system using 3D-DIC [18]. Under analogous conditions, the obtained ODSs were

compared with numerical simulations for a cantilever beam and it was demonstrated that no distortion occurred as a consequence of separate magnification of the images from each camera. This methodology was then performed on a large aeronautical panel where 3D-DIC measurements provided out-of-plane information that could not be assessed by simple visual inspection despite magnification.

In this study, the capabilities of the combination of 3D-DIC and PMM are explored during random excitation to enable multiple mode evaluation in a single test. In a previous study on stereophotogrammetry and magnification in random tests, Poozesh et al. [19] employed 3D-DIC to reveal one low response mode of a simple cantilever beam. Here, the passenger window of a full-scale aircraft demonstrator is evaluated. Multiple modes have been magnified to reveal the shape after a previous identification in a stabilisation diagram. ODSs have been obtained in a full-field manner with negligible presence of noise or other modes. The results have been validated using the mode shapes from forced normal mode tests. Videos of the naked motion and also including the displacement maps allowed an intuitive interpretation of the deformation. That allowed behaviour characterisation of the window frame, what is of significant interest for the structure integrity.

2. Experimental Tests

The methodology for ODSs evaluation using PMM and 3D-DIC was performed in Clean Sky GRA MT2 Cockpit Demonstrator shown in Figure 1. The demonstrator consisted in a cabin fixed to a bulkhead and was fully instrumented to characterise and evaluate the behaviour under different force and environmental conditions. However, these sensors are not employed in this study. This work is focused on a specific part of the demonstrator, the passenger window, highlighted in Figure 1, which involves a discontinuity in the composite peel. Hence, this part plays a critical role in noise generation and keeping the airtightness.

An electrodynamic shaker model LDS V450 was employed to generate noise random excitation in the spectrum 40–300 Hz. This study investigated the local behaviour of the window, and hence, lower frequencies were avoided as they involve global structure deformation or any other rigid body behaviour. The vibration was transmitted to the cabin lateral through a stinger as seen in Figure 1(b). An accelerometer was placed in the shaker's armature to record the excitation.

Two high-speed cameras, model Photron FastCam SA4 (1 megapixel full resolution), were employed to record the response on the inner surface of the window under excitation, as observed in Figure 2. Both cameras were supported on a rigid aluminium structure which was fixed to the bulkhead in order to isolate them from the vibration. The event was recorded at 2000 fps according to the Nyquist criterion and the shutter speed was 0.1 ms, short enough to avoid blurring. Two light sources were also employed to generate clear, high-contrast images. The accelerometer signal was synchronised with both cameras through a DAQ device model NI USB-6251.



FIGURE 1: (a) Full-scale aircraft demonstrator and (b) the lateral excitation configuration using (i) a shaker with (ii) a stinger to measure on (iii) the passenger window.



FIGURE 2: Stereoscopic setup composed by (i) two high-speed cameras and (ii) light sources recording on (iii) the passenger window from inside.

Two additional forced normal mode tests were performed to validate the ODSs obtained from magnified images using the same setup and recording parameter as described in Figure 2.

3. Image Processing

3.1. Phase-Based Motion Magnification. In this study, the phased-based motion magnification methodology developed by Wadhwa et al. [7] was employed. This algorithm exploits the phase signals of the complex steerable pyramids, consisting in Gabor wavelets, at different positions and orientations to identify the local motions in spatial subbands of an image. The concept is analogous to Fourier shift theorem for sine function transforms. For instance, a generic 1D spatial-domain intensity profile, $I(x)$, that is moved according to a time-domain function, $\delta(t)$, can be described by a Fourier series decomposition as follows:

$$I(x + \delta(t)) = \sum_{\omega_s=-\infty}^{\infty} C_s e^{i\omega_s(x+\delta(t))}, \quad (1)$$

where ω_s is the frequency and C_s the amplitude of the sinusoid. Phase shifting of a hypothetical single sinusoid fringe image is shown in Figure 3 when motion occurs along the x direction. As can be observed, the phase is encoded as a phase shifting, $x + \delta(t)$, with respect to the initial position. Considering this analogy, the phase signal of each pyramid is then band-pass filtered and multiplied by a factor. The

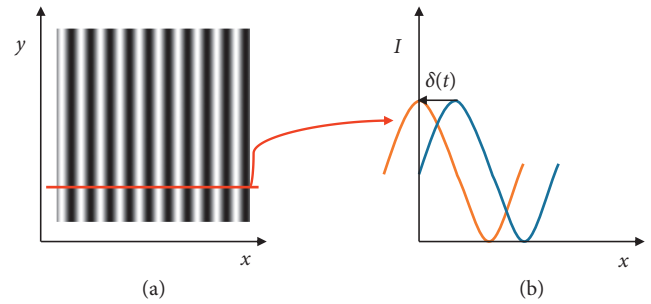


FIGURE 3: (a) Sinusoidal fringe image and (b) the effect of x -motion in a 1D intensity profile.

video reconstruction would show a magnified version of the motion present in that frequency band, previously imperceptible. Hence, the algorithm inputs are the image sequence, the desired frequency band, and the magnification factor.

For subsequent measurements using 3D-DIC, the sequence from each camera must be magnified using the same parameters [18]. Unlike sinusoidal excitation, many significant modes are now present in the images simultaneously. Therefore, magnification factors were chosen so that the responses of the nonmagnified modes were negligible in comparison with the magnified one.

Considering the random nature of the recorded vibration, the larger is the sequence, the better are the results. However, phase-based motion magnification is highly memory demanding, and this limits the sequence length. In this occasion, a computer with 32 GB RAM was employed allowing 1000 image sequences of 1 megapixel.

3.2. 3D Digital Image Correlation. Digital image correlation is an optical technique based on intensity field correlation to perform displacement and strain measurements in images [1]. For 3D-DIC, images from a stereoscopic system composed by using two cameras are employed. The calibration of the stereovision consisted in determining both extrinsic parameters, which define the relative position of the cameras and establish the relation of the coordinate systems, and intrinsic parameters, related to the position of the sensor, the lenses, and the light. An area of interest is identified in the

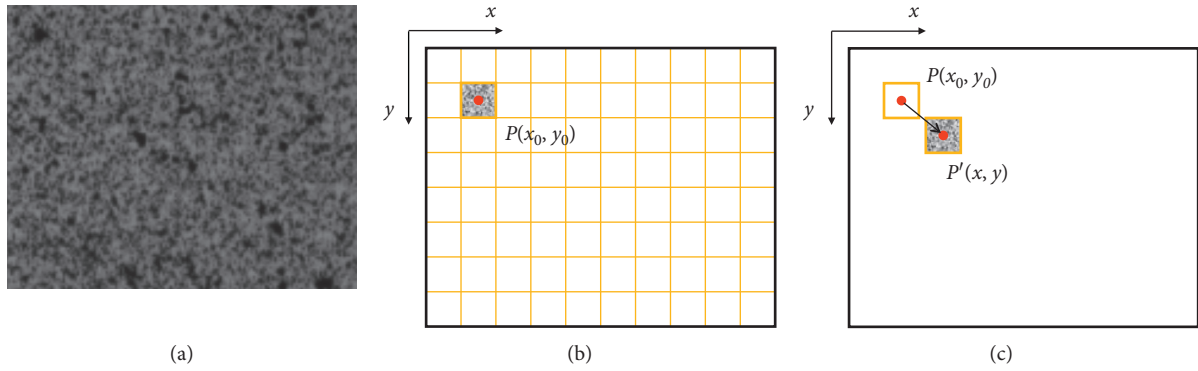


FIGURE 4: (a) Example of a grey-scale speckle pattern on the surface of interest. (b) Facet grid generation in the reference image highlighting that whose central pixel P . (c) Position of the pixel P after deformation, P' , to determine the displacement vector.

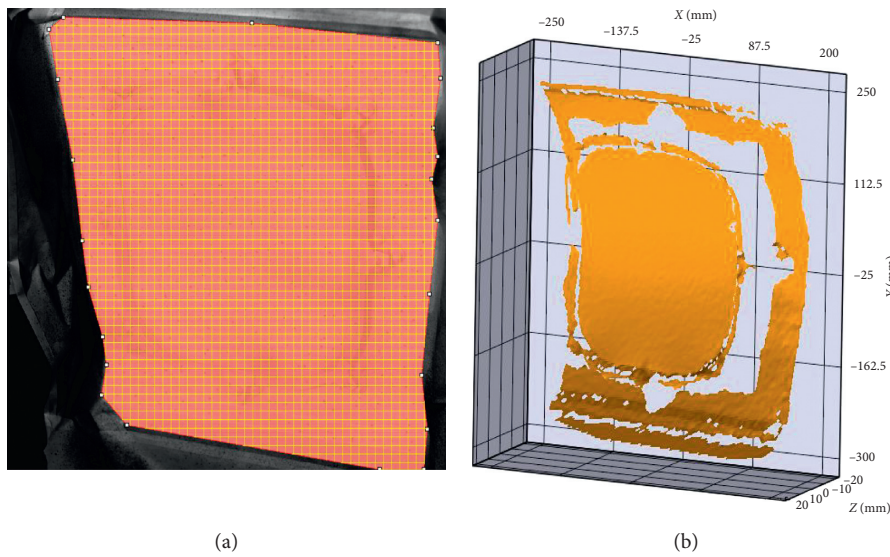


FIGURE 5: (a) Region of interest and facet size and (b) 3D digitalisation using 3D-DIC.

reference image from one camera and divided into squared subregions of pixels called facets or subsets. To make every facet unique, the surface is typically treated to generate a grey-scale speckle pattern as shown in Figure 4(a). The size of the facets is an odd number of pixels ($2M+1$), where M is an integer number, so that the facet central pixel is P at the position (x_0, y_0) [20], as shown in Figure 4(b). The central pixel of every facet is initially identified in the second camera as the most similar intensity area. With this first identification, it is possible to determine the spatial position of the central pixel of every facet, i.e., every measurement point and hence a digitalisation of the specimen surface. Performing the correlation in the subsequent deformed states, the displacement of every facet is determined, as shown in Figure 4(c).

In the present case, the window and the surrounding peel was coated with white paint and then sprayed with black paint to create the random speckle pattern. The correlation analysis was performed with Vic 3D software from Correlated Solutions Inc. using 19-pixel facet and 5-pixel overlap step. That generated a full-field measurement equivalent to 23000 3D sensors in this surface. Facet size can be compared

with the image size in Figure 5(a), and the resulting surface digitalisation is shown in Figure 5(b).

4. Results and Discussion

As a broadband event, the expected response of the window to such excitation is a combination of the modes in this spectrum. Therefore, an instantaneous out-of-plane displacement, W , in Figure 6 shows that no clear mode shape extraction could be done by visualising the time-domain response. Actually, a significant amount of noise was also expected and found due to the low sensitivity of non-interferometric techniques in comparison with traditional pointwise sensors such as accelerometers or even laser vibrometry [21, 22]. Therefore, PMM was employed in this study to highlight individual ODSs, making both other modes and noise negligible [7, 14].

Before performing the magnification, some modes had to be identified. The full-field transfer functions were obtained from the 3D-DIC and the accelerometer measurements under the same noise excitation. The excitation

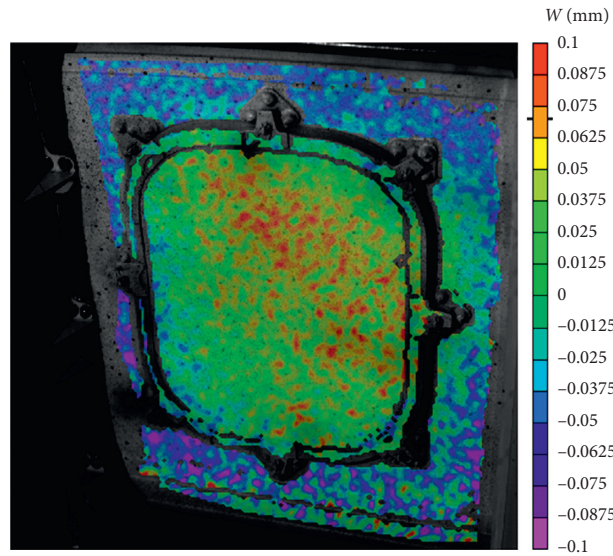


FIGURE 6: Instantaneous out-of-plane displacements, W , measured by 3D-DIC under random excitation.

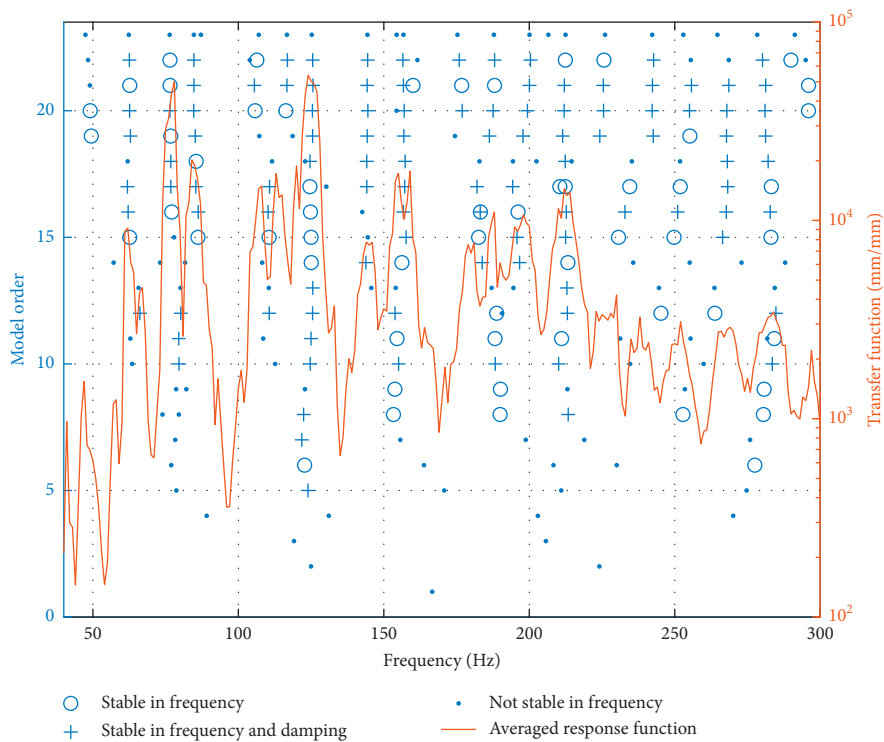


FIGURE 7: Stabilisation diagram obtained from the least squares complex exponential method applied to the full-field transfer functions.

displacement amplitudes were obtained by accelerometer signal double integration. As RAM was not a limitation for 3D-DIC processing but only for PMM, 5400 frame sequences were considered for this estimation that eventually yielded 1 Hz frequency resolution. The stabilisation diagram corresponding to the least squares complex exponential method was chosen to highlight modes. This diagram is represented in Figure 7 and shows the averaged transfer function. Multiple peaks were observed, many of which can be attributed to global structural modes that do not show the

local behaviour of the region. These modes were not of interest in this study. The selected local modes for magnification were found at the peaks 124 Hz, 155 Hz, 215 Hz, and 268 Hz. In fact, these had the highest stabilisation trend and the selection is also supported by the previous study results [6]. Then, magnification was performed in a narrow band for each one. The magnification factors were 50x for 124 Hz and 100x for the rest. Those values were determined according to the level of response to yield clear displacement maps without producing blurring derived from excessive magnification.

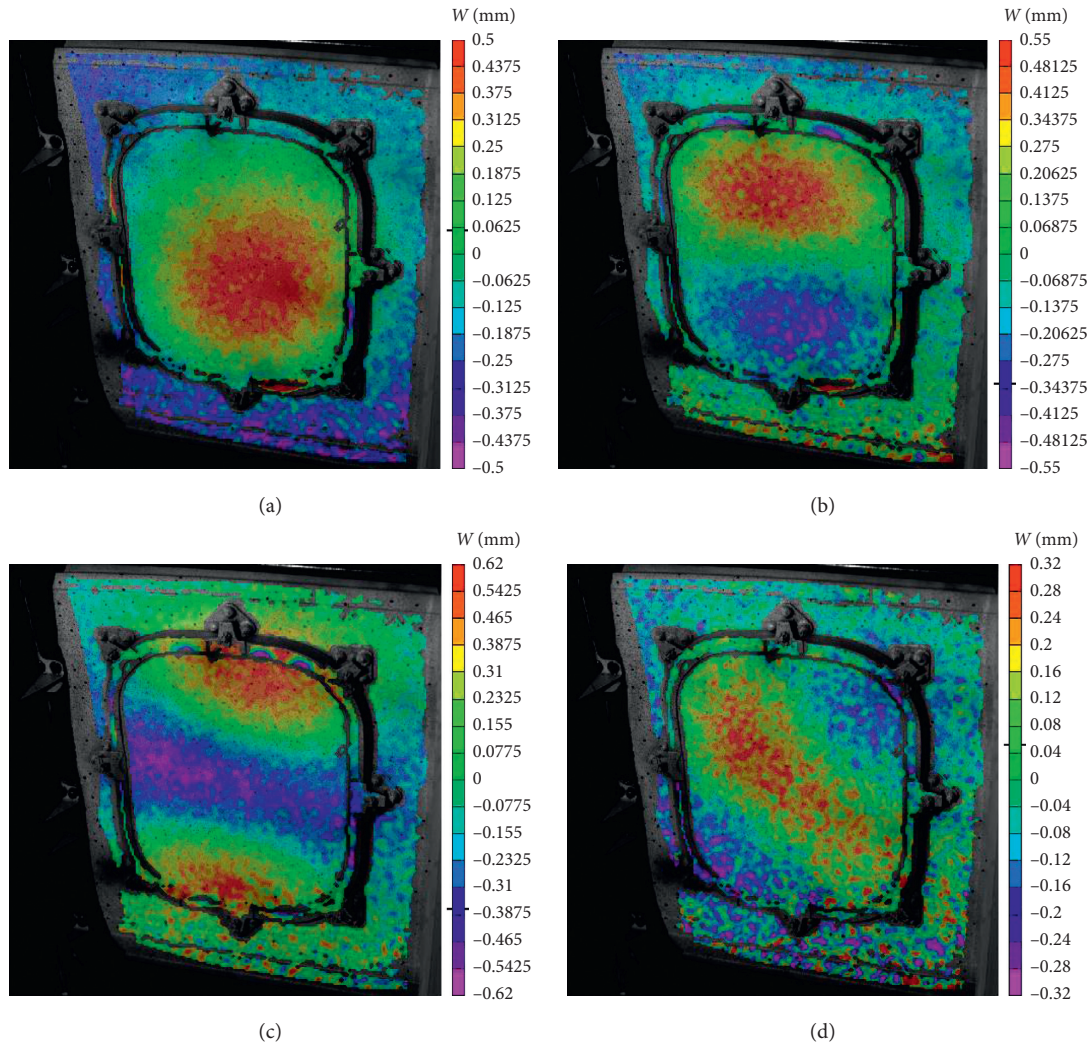


FIGURE 8: ODSs of the window in the out-of-plane direction, W , obtained with 3D-DIC after magnifying the resonances: (a) 124 Hz, (b) 155 Hz, (c) 215 Hz, and (d) 268 Hz.

As a result, videos were obtained showing a clear motion for the naked eye. The videos corresponding to the right-hand side camera can be found as Videos 1–4 in supplementary material for each respective mode. As can be seen, these videos describe the local behaviour of the window and the surrounding aircraft's peel. Comparing them, different deformations are noticed from one mode to another, and the complexity is increasing for higher frequency modes, as expected. This makes the interpretation of the motion difficult for the naked eye. Under this limitation, 3D-DIC measurements were performed in the magnified sequences. Taking into account that bending is mainly described by out-of-plane displacements, called as W , focus was placed on this direction. Four respective videos were obtained that included the displacement maps evolution (Videos 5–8). The instantaneous W maps at the signal crest are shown in Figure 8. The measurement allowed the quantification of the virtual motion of these images and improved the interpretation of the deformation. It is also worth mentioning the capabilities of the methodology to extract ODSs from a random event where just a combination of noise and modes was obtained. They all

correspond to bending modes of increasing order mainly produced in the window itself. They can be checked against the ODSs obtained from forced normal mode tests. A quick identification of two resonances at 124 Hz and 215 Hz was performed with an impact hammer test. Hence, the ODSs for these frequencies under sinusoidal excitation are shown in Figure 9. Magnified ODSs from random tests show the same behaviour what proves they are actual ODSs and the influence of the remaining modes is negligible.

Overall, both sorts of video provide a meaningful insight of the behaviour of the window. For instance, the travelling wave effect produced by different phase lag along the surface is evidenced. For the first mode, the phase lag is more homogeneous, but this effect is especially relevant for the three higher frequency modes. However, there is an additional behaviour that might be of major importance for the integrity of the joint with the peel and hence for the airtightness. In all the analysed resonances, the frame experienced deformation in certain zones with the highest amplitudes of the whole surface. By observing the displacement maps in Figure 8 (more notorious in Videos 5–8),

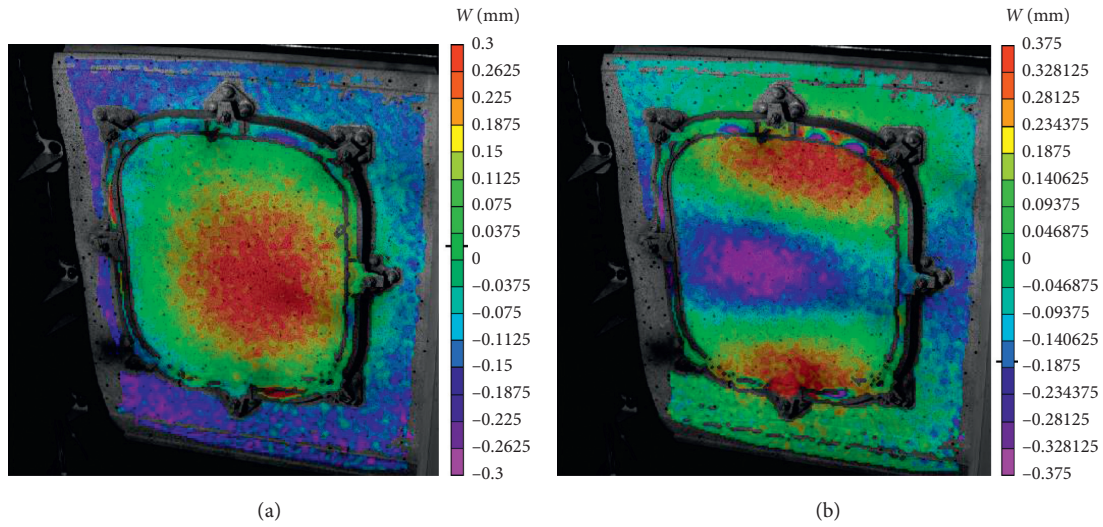


FIGURE 9: ODSs of the window in the out-of-plane direction, W , obtained with 3D-DIC in forced normal mode tests for the resonances: (a) 124 Hz and (b) 215 Hz.

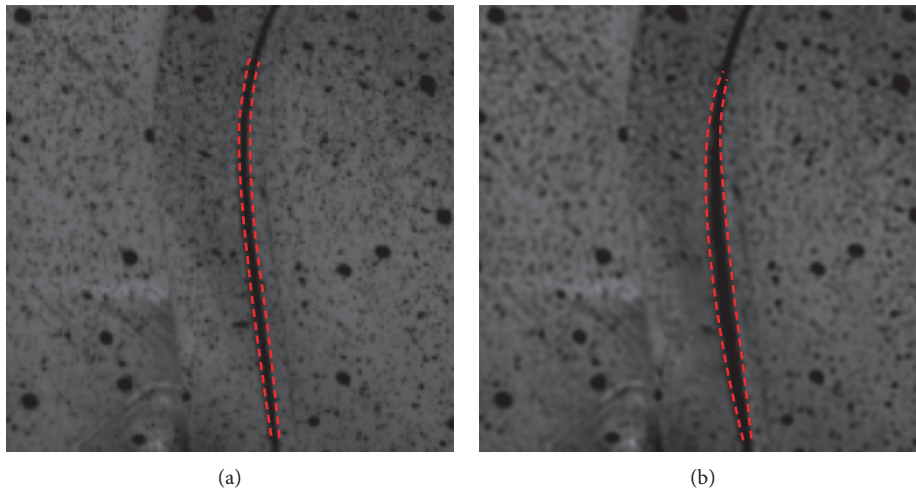


FIGURE 10: Window's frame upper right corner in the nonloaded state (a) and at maximum deformation (b) for the magnified resonance 124 Hz.

this deformation can be localised. The motion may be intuited in the motion Videos 1–4, but zoom-in videos are provided for detailed inspection. In the first mode, large amplitudes are detected on the left part of the frame and also close to the right lower corner. They can be observed, respectively, in zoom-in Videos 9–10. Namely, the maximum deformation of the left part is compared with the nonloaded state in Figure 10. Blurring appeared in the frame as a consequence of the large displacements after magnification. Since the displacement in the window was smaller, the magnification factor was chosen to provide good displacement fields for the window despite the little blurring of the frame. As observed, maximum displacements for the second resonance mainly occur in the upper and lower parts, shown the former in Video 11. It is worthy to note that the third mode shows higher order deformation, especially close to the right upper corner as seen in Video 12. A particular case

is the last mode as no deformation was detected in the frame in the W direction. However, vertical displacements, V , shown in Figure 11 revealed a significant deformation in the upper region of the frame. This vertical motion can be confirmed watching the zoom Video 13.

5. Conclusions

This study shows the benefits of the combination of phase-based motion magnification and 3D-DIC, especially for evaluating the complex structures where no conclusive information can be obtained from a single camera. Multiple ODSs of the passenger window of a full-scale aircraft demonstrator were deduced, visualized, and quantitatively measured from a single random excitation test. The magnification of an individual resonance from a broadband response makes it predominant against the other and its only

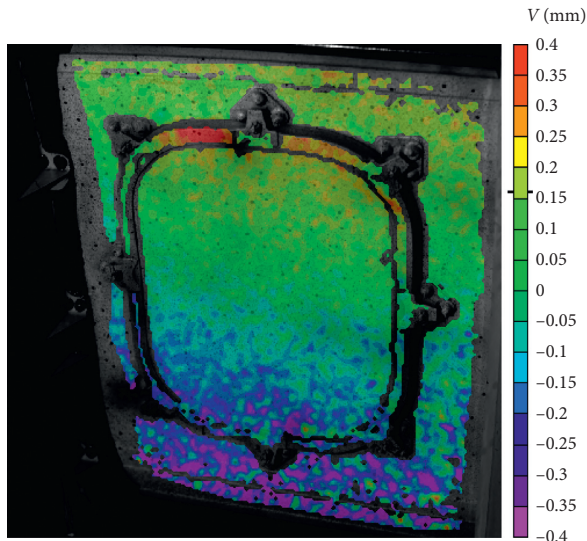


FIGURE 11: ODSs of the window in the vertical direction, V , obtained with 3D-DIC in forced normal mode tests for the resonance 268 Hz.

presence can be assumed. Larger amplitude motion achieved by magnification allowed clearer 3D-DIC displacement maps to be obtained which was little influenced by noise. On the contrary, 3D measurement provided the necessary information to understand the motion of the magnified videos. These measurements agreed with the ODSs obtained in forced normal mode tests. As a conclusion, visual and quantitative information proved to be complementary and provided a deep insight into an intuitive interpretation and understanding of the deformation.

Furthermore, this is a powerful tool for such big structures since it is able to give high-density information in critical parts which could not be achieved by using spaced sensors, being possible to lose localised effects. This paper has demonstrated the potential when detecting significant deformation of the window's frame. This provides relevant information and feedback to improve the union of the window and the peel that ensures the integrity and airtightness.

Data Availability

The data used to support the findings of this study are available from the corresponding author upon request.

Disclosure

Activities reported in this paper were developed in the frame of the European Community Seventh Framework Program, where Airbus Defence and Space S.A.U. was a partner of the Clean Sky Green Regional Aircraft Integrated Technology Demonstrator. The University of Jaén (Spain) participated under contract with Airbus Defence and Space S.A.U. in the field of testing technologies.

Conflicts of Interest

The authors declare that there are no conflicts of interest regarding the publication of this paper.

Supplementary Materials

A description of the videos supplied as supplementary materials is here provided. They can be found in the online version of the present paper.

Supplementary 1. Video 1: naked motion of the window ODS at 124 Hz using 50x magnification factor from the right-hand side camera viewpoint.

Supplementary 2. Video 2: naked motion of the window ODS at 155 Hz using 100x magnification factor from the right-hand side camera viewpoint.

Supplementary 3. Video 3: naked motion of the window ODS at 215 Hz using 100x magnification factor from the right-hand side camera viewpoint.

Supplementary 4. Video 4: naked motion of the window ODS at 268 Hz using 100x magnification factor from the right-hand side camera viewpoint.

Supplementary 5. Video 5: ODSs of the window in the out-of-plane direction, W , obtained with 3D-DIC after magnifying the resonance 124 Hz with 50x factor.

Supplementary 6. Video 6: ODSs of the window in the out-of-plane direction, W , obtained with 3D-DIC after magnifying the resonance 155 Hz with 100x factor.

Supplementary 7. Video 7: ODSs of the window in the out-of-plane direction, W , obtained with 3D-DIC after magnifying the resonance 215 Hz with 100x factor.

Supplementary 8. Video 8: ODSs of the window in the out-of-plane direction, W , obtained with 3D-DIC after magnifying the resonance 268 Hz with 100x factor.

Supplementary 9. Video 9: naked motion of the window ODS at 124 Hz using 50x magnification factor zooming at the left part of the frame from the right-hand side camera viewpoint.

Supplementary 10. Video 10: naked motion of the window ODS at 124 Hz using 50x magnification factor zooming at the right lower corner of the frame from the right-hand side camera viewpoint.

Supplementary 11. Video 11: naked motion of the window ODS at 155 Hz using 100x magnification factor zooming at the upper part of the frame from the left-hand side camera viewpoint.

Supplementary 12. Video 12: naked motion of the window ODS at 215 Hz using 100x magnification factor zooming at the upper part of the frame from the left-hand side camera viewpoint.

Supplementary 13. Video 13: naked motion of the window ODS at 268 Hz using 100x magnification factor zooming at the upper part of the frame from the left-hand side camera viewpoint.

References

- [1] H. Schreier, J.-J. Orteu, and M. A. Sutton, *Image Correlation for Shape, Motion and Deformation Measurements*, Springer, Boston, MA, USA, 2009.

- [2] R. Huñady and M. Hagara, "A new procedure of modal parameter estimation for high-speed digital image correlation," *Mech. Syst. Signal Process.*, vol. 93, pp. 66–79, 2017.
- [3] D. A. Ehrhardt, M. S. Allen, S. Yang, and T. J. Bebernis, "Full-field linear and nonlinear measurements using continuous-scan laser Doppler vibrometry and high speed three-dimensional digital image correlation," *Mechanical Systems and Signal Processing*, vol. 86, pp. 82–97, 2017.
- [4] P. L. Reu, D. P. Rohe, and L. D. Jacobs, "Comparison of DIC and LDV for practical vibration and modal measurements," *Mechanical Systems and Signal Processing*, vol. 86, pp. 2–16, 2017.
- [5] T. J. Bebernis and D. A. Ehrhardt, "High-speed 3D digital image correlation vibration measurement: recent advancements and noted limitations," *Mechanical Systems and Signal Processing*, vol. 86, pp. 35–48, 2017.
- [6] Á. Molina-Viedma, E. López-Alba, L. Felipe-Sesé, F. Díaz, J. Rodríguez-Ahlquist, and M. Iglesias-Vallejo, "Modal parameters evaluation in a full-scale Aircraft demonstrator under different environmental conditions using HS 3D-DIC," *Materials*, vol. 11, no. 2, p. 230, 2018.
- [7] N. Wadhwa, M. Rubinstein, F. Durand, and W. T. Freeman, "Phase-based video motion processing," *ACM Transactions on Graphics*, vol. 32, no. 4, p. 1, 2013.
- [8] E. P. Simoncelli, W. T. Freeman, E. H. Adelson, and D. J. Heeger, "Shiftable multiscale transforms," *IEEE Transactions on Information Theory*, vol. 38, no. 2, pp. 587–607, 1992.
- [9] E. P. Simoncelli and W. T. Freeman, "The steerable pyramid: a flexible architecture for multi-scale derivative computation," in *Proceedings of the International Conference on Image Processing*, vol. 3, pp. 444–447, Washington, DC, USA, October 1995.
- [10] J. Portilla and E. P. Simoncelli, "A parametric texture model based on joint statistics of complex wavelet coefficients," *International Journal of Computer Vision*, vol. 40, no. 1, pp. 49–70, 2000.
- [11] H.-Y. Wu, M. Rubinstein, E. Shih, J. Guttag, F. Durand, and W. Freeman, "Eulerian video magnification for revealing subtle changes in the world," *ACM Transactions on Graphics*, vol. 31, no. 4, pp. 1–8, 2012.
- [12] J. G. Chen, N. Wadhwa, Y.-J. Cha, F. Durand, W. T. Freeman, and O. Buyukozturk, "Modal identification of simple structures with high-speed video using motion magnification," *Journal of Sound and Vibration*, vol. 345, pp. 58–71, 2015.
- [13] A. Sarrafi, Z. Mao, C. Niezrecki, and P. Poozesh, "Vibration-based damage detection in wind turbine blades using Phase-based Motion Estimation and motion magnification," *Journal of Sound and Vibration*, vol. 421, pp. 300–318, 2018.
- [14] Y. Yang, C. Dorn, T. Mancini et al., "Blind identification of full-field vibration modes from video measurements with phase-based video motion magnification," *Mechanical Systems and Signal Processing*, vol. 85, pp. 567–590, 2017.
- [15] Y. Yang, C. Dorn, T. Mancini et al., "Blind identification of full-field vibration modes of output-only structures from uniformly-sampled, possibly temporally-aliased (sub-Nyquist), video measurements," *Journal of Sound and Vibration*, vol. 390, pp. 232–256, 2017.
- [16] Y. Yang, C. Dorn, T. Mancini et al., "Reference-free detection of minute, non-visible, damage using full-field, high-resolution mode shapes output-only identified from digital videos of structures," *Structural Health Monitoring*, vol. 17, no. 3, pp. 514–531, 2017.
- [17] A. J. Molina-Viedma, L. Felipe-Sesé, E. López-Alba, and F. Díaz, "High frequency mode shapes characterisation using Digital Image Correlation and phase-based motion magnification," *Mechanical Systems and Signal Processing*, vol. 102, pp. 245–261, 2018.
- [18] A. J. Molina-Viedma, L. Felipe-Sesé, E. López-Alba, and F. A. Díaz, "3D mode shapes characterisation using phase-based motion magnification in large structures using stereoscopic DIC," *Mechanical Systems and Signal Processing*, vol. 108, pp. 140–155, 2018.
- [19] P. Poozesh, A. Sarrafi, Z. Mao, P. Avitabile, and C. Niezrecki, "Feasibility of extracting operating shapes using phase-based motion magnification technique and stereo-photogrammetry," *Journal of Sound and Vibration*, vol. 407, pp. 350–366, 2017.
- [20] B. Pan, K. Qian, H. Xie, and A. Asundi, "Two-dimensional digital image correlation for in-plane displacement and strain measurement: a review," *Measurement Science and Technology*, vol. 20, no. 6, p. 062001, 2009.
- [21] M. N. Helfrick, C. Niezrecki, P. Avitabile, and T. Schmidt, "3D digital image correlation methods for full-field vibration measurement," *Mechanical Systems and Signal Processing*, vol. 25, no. 3, pp. 917–927, 2011.
- [22] C. Warren, C. Niezrecki, P. Avitabile, and P. Pingle, "Comparison of FRF measurements and mode shapes determined using optically image based, laser, and accelerometer measurements," *Mechanical Systems and Signal Processing*, vol. 25, no. 6, pp. 2191–2202, 2011.

Research Article

Rail Corrugation Detection of High-Speed Railway Using Wheel Dynamic Responses

Jianbo Li ^{1,2} and Hongmei Shi ^{1,2}

¹School of Mechanical, Electronic and Control Engineering, Beijing Jiaotong University, Beijing 100044, China

²Key Laboratory of Vehicle Advanced Manufacturing, Measuring and Control Technology (Beijing Jiaotong University), Ministry of Education, Beijing 100044, China

Correspondence should be addressed to Hongmei Shi; hmshi@bjtu.edu.cn

Received 4 January 2019; Accepted 11 February 2019; Published 25 February 2019

Guest Editor: Krzysztof Holak

Copyright © 2019 Jianbo Li and Hongmei Shi. This is an open access article distributed under the Creative Commons Attribution License, which permits unrestricted use, distribution, and reproduction in any medium, provided the original work is properly cited.

Rail corrugation often occurs on the high-speed railway, which will affect ride comfort and even the train operation safety in severe condition. Detection of rail corrugation wavelength and depth is absolutely essential for maintenance and safety. A novel method using wheel vibration acceleration is proposed in this paper, in which ensemble empirical mode decomposition (EEMD) is employed to estimate the wavelength, and bispectrum features are extracted to recognize the depth with support vector machine (SVM). Firstly, a vehicle-track coupling model considering the rail corrugation of high-speed railway is established to calculate the wheel vibration acceleration. Secondly, the estimation algorithm of wavelength is studied by analyzing the main frequency with EEMD. The optimal parameters of EEMD are selected according to the orthogonal coefficient of decomposition results and the distribution of the extreme points of signal. The depth detection is transformed to a classification problem with SVM. Bispectrum features, which are extracted from the reconstructed signal using the high-frequency components of wheel vibration acceleration, combining with train speed and corrugation wavelength are input into SVM to recognize the rail corrugation depth. Finally, numerical simulation is carried out to verify the accuracy of the proposed estimation method. The simulation results show that the proposed detection algorithm can accurately identify rail corrugation, the estimation error of rail corrugation wavelength is less than 0.25%, and the classification accuracy of rail corrugation depth is more than 99%.

1. Introduction

Rail corrugation is a type of wavy wear formed longitudinally along the top of the rail, which appears in all types of rail systems [1]. With the rapid development of high-speed railway, rail corrugation has been found everywhere, especially with a fixed rail corrugation wavelength due to the same train operation speed and vehicle type. The results of field tests on a high-speed railway in China [2] show that rail corrugation is distributed in many discontinuous places. The length of rail corrugation is usually about 10 m to 15 m along the longitudinal direction of rail, and the wavelength is from 120 mm to 150 mm. The depth of rail corrugation is much smaller, generally in the range of 0.04 mm to 0.1 mm. The rail corrugation causes aggravated interactions between vehicle

and rail and terrible noises, which severely influences the safety and ride comfort of a running high-speed train. It is necessary for maintenance and safety to detect the wavelength and depth of rail corrugation effectively.

In recent years, research of track structure health monitoring utilizing vehicle vibration responses has attracted more and more attention. There are many studies on rail corrugation monitoring based on operating vehicles. Rail corrugation detection method based on vehicle vibration responses is a noncontact detection method. Moreover, vibration acceleration signal is easy to obtain, and real-time monitoring of track status can be realized without affecting railway operation. Hopkins and Taheri [3] proposed a defect detection algorithm for rail health monitoring with wavelet transform. The vibration acceleration signal of the bogie is

decomposed by wavelet transform, and the Lipschitz exponent of each scale is calculated to identify wheel flat, rail crack, and rail corrugation. Molodova et al. [4] used axle box acceleration to measure short wave track defects including rail corrugation. The amplitude and power spectral density of the vibration acceleration signal of axle box are analyzed to detect defects. Huang et al. [5] proposed a rail corrugation detection technology based on fiber laser accelerometer. The fiber laser accelerometer is installed on the bogie to detect the vertical acceleration of train axle box. The vibration acceleration signal is denoised by wavelet transform, and then the waveform of rail corrugation is estimated by double integral. Kaewunruen [6] used dynamic wheel-rail interaction to monitor rail corrugation on curved track for guiding maintenance. Corrugation roughness data are also obtained by double integration of axle box acceleration signals. Salvador et al. [7] made time-frequency analysis of the axle box vibration acceleration signal with short-time Fourier transform, which can detect rail corrugation, isolated rail defects, and loss of track vertical alignment. Most of the above studies only identify if there is rail corrugation defect, without giving a detailed diagnosis of the wavelength and depth of rail corrugation.

EEMD is a signal decomposition method, which is an improvement algorithm of empirical mode decomposition (EMD) and widely used in signal analysis and mechanical fault diagnosis. Shen et al. [8] proposed fast EEMD optimization algorithm, which applies nonlinear correlation coefficient and accuracy requirements to obtain the best parameters of EEMD. The proposed EEMD optimization algorithm is used to extract the accent of emotional speech. Guo and Tse [9] used EEMD to analyze bearing vibration signals and proposed a method to automatically select appropriate EEMD parameters using the relative root mean square error between the decomposition result and the original signal. Xue et al. [10] applied the same method to diagnose the fault of rolling bearing. Kedadouche et al. [11] used the Pearson coefficient of correlation between IMFs to select the parameters of EEMD.

In this paper, a rail corrugation detection method is presented based on the vertical vibration response of wheel. The basic principle of detection algorithm is analyzing the high frequency of wheel vibration acceleration with EEMD method to estimate the wavelength and depth of rail corrugation. The paper is organized as follows: A vehicle-track coupling model considering rail corrugation is described in Section 2 to calculate the wheel vibration acceleration used in the detection algorithm. The detection algorithm of rail corrugation is presented in Section 3, in which the estimation method of wavelength using EEMD to acquire the main frequency and the bispectrum features extraction to classify the depth are, respectively, described in detail. The numerical simulation and detection results of rail corrugation are demonstrated and analyzed in Section 4.

2. Simulation Model

In order to obtain the wheel dynamic responses used to detect rail corrugation, a vertical vehicle-track coupling

model is established as shown in Figure 1, consisting of vehicle model, track model, track irregularity model, and rail corrugation model.

2.1. Vehicle Model of High-Speed Railway. The vehicle model is a multibody system including a car body, two bogies, and four wheelsets, which are connected by stiffness-damping elements [12]. There are 10 degrees of freedom, which are the vertical motion y_c and nodding motion β_c of the car body, the vertical motion y_t and nodding motion β_t of two bogies, and the vertical motion y_w of four wheelsets. The vehicle parameters of Chinese high-speed train CRH3 used in the model are represented in Table 1.

2.2. Slab Track Model. The slab ballastless track structure is applied into the track model for its wide use in China high-speed railway, which is constituted of rail, fasteners, track slabs, CA mortar layer, and foundation [14]. The rail is regarded as an infinite beam with continuous support, the track slab is regarded as a free beam, and the fasteners and mortar layer are represented as equivalent stiffness-damping elements. The parameters of the slab track model for simulation are shown in Table 2.

2.3. Vehicle-Track Coupling Model. The vehicle model and the track model are coupled by wheel-rail interaction. According to Hertzian nonlinear elastic theory [12], the vertical force between the wheel and rail is defined as

$$p(t) = \begin{cases} \left[\frac{1}{G} \Delta Z(t) \right]^{3/2}, & \Delta Z(t) \geq 0, \\ 0, & \Delta Z(t) < 0, \end{cases} \quad (1)$$

where G is the wheel-rail contact constant and $\Delta Z(t)$ is the elastic compression deformation between the wheel and rail.

The elastic compression between wheel and rail is determined by the displacement of wheel and rail at the wheel-rail contact point, expressed as

$$\Delta Z(t) = y_{wi}(t) - y_r(x_{wi}, t) - y_0(t), \quad i = 1 \sim 4, \quad (2)$$

where y_{wi} is the displacement of the wheel; y_r is the displacement of the rail; and y_0 is the track irregularity which is the main excitation of vehicle-track coupling system. The power spectral density of ballastless track irregularities of China high-speed railway [15] is as follows:

$$S(f) = \begin{cases} 1.0544 \times 10^{-5} \times f^{-3.3891}, & f \leq 0.0187, \\ 3.5588 \times 10^{-3} \times f^{-1.9271}, & 0.0187 < f \leq 0.0474, \\ 1.9784 \times 10^{-3} \times f^{-1.3643}, & 0.0474 < f \leq 0.1533, \\ 3.9488 \times 10^{-3} \times f^{-3.4516}, & f > 0.1555, \end{cases} \quad (3)$$

where f is the spatial frequency.

The random track irregularities in spatial domain y_{irr} can be calculated with IFFT.

The dynamic equation of the vehicle-track coupling system is obtained by combining the vehicle vibration equation with the track vibration equation, which is expressed as

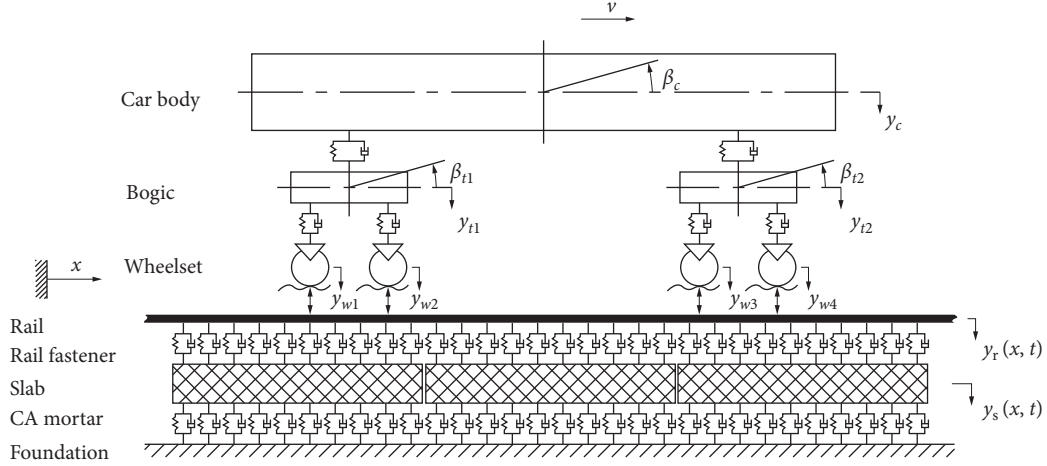


FIGURE 1: The vehicle-track system model of high-speed railway.

TABLE 1: Parameters for Chinese high-speed train CRH3 [13].

Parameter	Value	Unit
Mass of car body	40000	kg
Mass of bogie	3200	kg
Mass of wheelset	2400	kg
Pitch inertia of car body	547000	kg·m ²
Pitch inertia of bogie	6800	kg·m ²
Stiffness of primary suspension system	2.08×10^6	N/m
Stiffness of secondary suspension system	8×10^5	N/m
Damping of primary suspension system	1×10^5	N·s/m
Damping of secondary suspension system	1.2×10^5	N·s/m
Semilongitudinal distance between bogies	8.6875	m
Semilongitudinal distance between wheelsets in bogie	1.25	m
Radius of wheel	0.46	m

TABLE 2: Parameters of the CRTS II slab track [13].

Parameter	Value	Unit
Elastic modulus of rail	2.1×10^{11}	N/m ²
Inertia of rail	3.217×10^{-5}	m ⁴
Mass of rail	60	kg/m
Stiffness of rail fastener	6×10^7	N/m
Damping of rail fastener	4.77×10^4	N·s/m
Elastic modulus of slab	3.9×10^{10}	N/m ²
Inertia of slab	8.5×10^{-5}	m ⁴
Mass of slab	1275	kg/m
Length of single slab	6.5	m
Stiffness of CA mortar	9×10^8	N/m
Damping of CA mortar	8.3×10^4	N·s/m

$$[M]\{A\} + [C]\{V\} + [K]\{X\} = \{P\}, \quad (4)$$

where $[M]$, $[C]$, and $[K]$ are the mass, damping, and stiffness matrices of the vehicle-track coupling model, respectively; $\{A\}$, $\{V\}$, and $\{X\}$ are the acceleration, velocity, and displacement vectors of the coupling model, respectively; and $\{P\}$ is the load vector of the coupling model.

Vehicle-track coupling model is a system of nonlinear differential equations, which can be solved by the numerical integration method.

2.4. Rail Corrugation Model. Rail corrugation is a kind of harmonic irregularity, which is expressed by a cosine function:

$$y_{\text{cor}}(t) = \frac{1}{2}a \left[1 - \cos\left(\frac{2\pi vt}{\lambda}\right) \right], \quad \left(0 \leq t \leq \frac{L}{v}\right), \quad (5)$$

where a is the depth of rail corrugation; λ is the wavelength of rail corrugation; v is the train speed; and L is the length of rail corrugation.

In this paper, a 130-meter track is simulated with a 10-meter rail corrugation at the middle position from 60°m to 70°m, of which the wavelength is from 100 mm to 150 mm and the depth is from 0.01 mm to 0.1 mm. Figure 2 shows a section of rail corrugation, of which the wavelength is 150 mm and the depth is 0.01 mm.

Therefore, the integrated track irregularity of the vehicle-track system can be expressed as

$$y_0(t) = y_{\text{irr}}(t) + y_{\text{cor}}(t). \quad (6)$$

Obviously, rail corrugation will influence the vibration response of wheels through wheel-rail interaction. Rail corrugation is a kind of short-wavelength irregularity, while the wavelength of random track irregularity is much longer. Therefore, high-frequency vibration will appear in the vibration response of wheels if rail corrugation exists, and the main frequency of high-frequency band matches the wavelength of rail corrugation. This is the basic principle of detecting rail corrugation using wheel dynamic responses.

2.5. Model Validation. It is necessary to validate the model accuracy because wheel responses used in the following detection algorithm are acquired from the model. Different conditions with different wavelength and depth of rail corrugation are simulated, and the results are compared with Wang's study [16]. The effect of rail corrugation wavelength on wheel-rail force is shown in Figure 3, in which the depth of rail corrugation is 0.1 mm and the train speed is 300 km/h. The results show that the influence of wavelength on wheel-rail force is nonlinear, and the maximum wheel-rail force is at 120 mm wavelength. Sensitive wavelength is

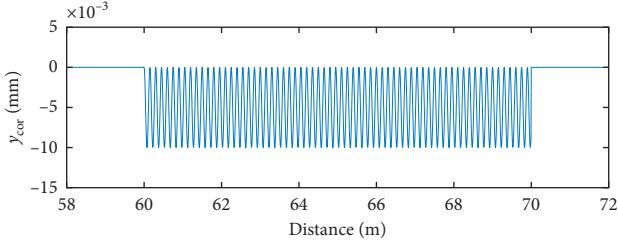


FIGURE 2: Rail corrugation.

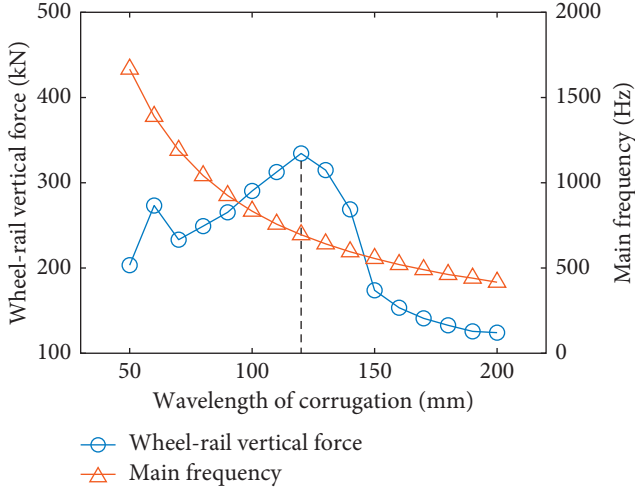


FIGURE 3: Effect of rail corrugation wavelength on wheel-rail interaction.

the wavelength when rail corrugation has the greatest effect on wheel-rail interaction. The sensitive wavelength of the simulation model is 120 mm. In addition, the main frequency of wheel-rail force is related to the wavelength and decreases with the increase of wavelength. The effect of rail corrugation depth on maximum wheel-rail force and rail vibration acceleration is shown in Figure 4. The wavelength of rail corrugation is determined to be 100 mm, and the train runs at 300 km/h. With the increase of rail corrugation depth, the values of wheel-rail force and rail vibration acceleration gradually increase. The simulation results show good consistence with the conclusion of Wang.

3. Detection Method

A detection method for rail corrugation is proposed, by which the wavelength can be estimated through analyzing main frequency of wheel vibration responses based on EEMD, and the depth can be classified with bispectrum features and SVM. The detection flow chart is shown in Figure 5. LIBSVM [17] toolbox and particle swarm optimization (PSO) are used to optimize the parameters of SVM.

3.1. Wavelength Estimation. The process of wavelength estimation can be described as 4 steps:

- (1) Decompose wheel acceleration signal using EEMD method.

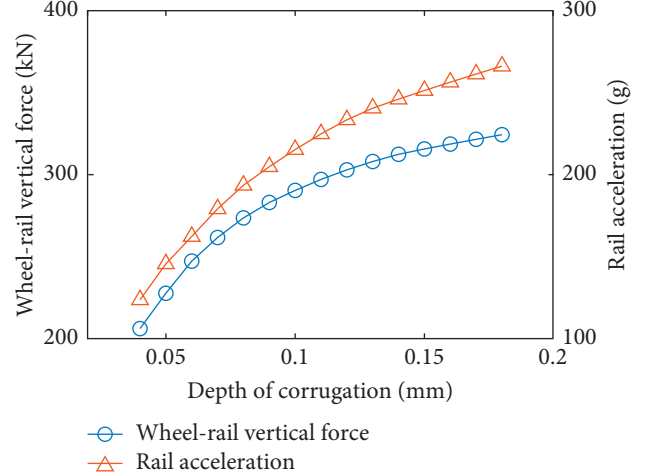


FIGURE 4: Effect of rail corrugation depth on wheel-rail interaction.

- (2) Eliminate the false intrinsic modal functions (IMFs) according to the correlation analysis between the IMFs and the original signal.
- (3) Select IMFs with high-frequency components and obtain their main frequency using FFT.
- (4) Estimate the wavelength of rail corrugation based on main frequency and train speed.

3.1.1. Background. Huang et al. [18] defined the signal satisfying the following two conditions as intrinsic modal function (IMF): (1) the number of extreme points and zero-crossing points is equal or different by one; (2) the mean value of the upper envelope formed by the local maximum points and the lower envelope formed by the local minimum points is zero.

The EMD process for signal $x(t)$ is as follows:

- (1) Find all local maximum points and local minimum points of the signal $x(t)$.
- (2) Fit the upper and lower envelope and obtain the average $m(t)$ of the upper and lower envelope and then calculate

$$h(t) = x(t) - m(t). \quad (7)$$

- (3) If $h(t)$ satisfies the above two conditions, then $h(t)$ is an IMF, denoted as $c(t)$; otherwise, $h(t)$ is treated as the original signal; repeat the above two steps.
- (4) Calculate the residual signal

$$r(t) = x(t) - c(t). \quad (8)$$

- (5) Regard $r(t)$ as the original data and repeat the above steps until the residual signal is a monotone function.
- (6) The original signal $x(t)$ can be expressed as the sum of all IMFs and residual signal $r(t)$:

$$x(t) = \sum_{i=1}^n c_i(t) + r(t). \quad (9)$$

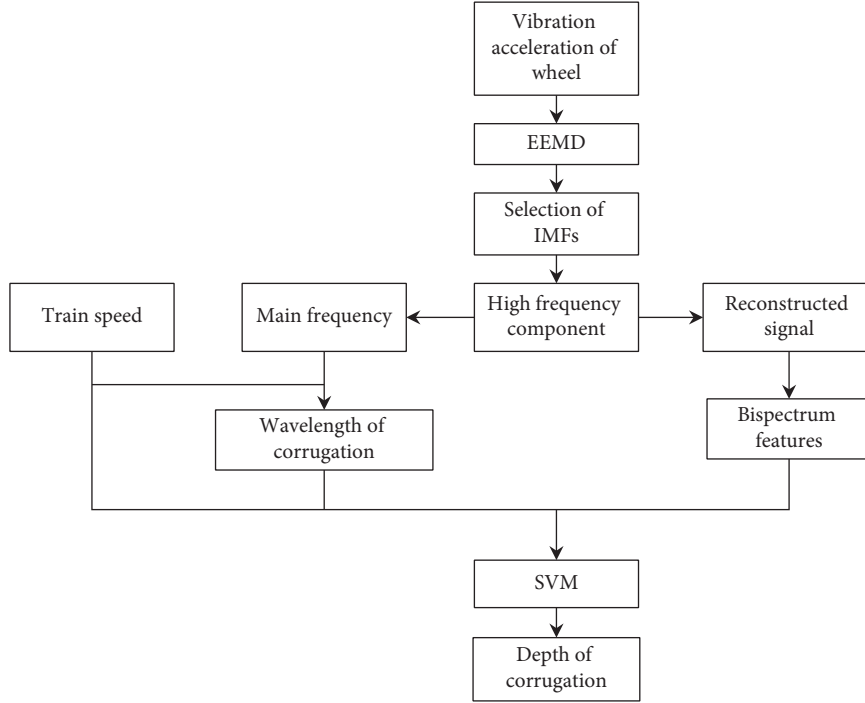


FIGURE 5: Rail corrugation detection method.

The orthogonality of IMFs is used to evaluate the decomposition results. The overall index of orthogonality is defined as

$$IO = \sum_{t=0}^T \left(\frac{\sum_{j=1}^{n+1} \sum_{k=1}^{n+1} c_j(t)c_k(t)}{x^2(t)} \right), \quad (j \neq k). \quad (10)$$

The mode mixing problem occurs when the signal is analyzed by IMF sifting method because there are multiple frequency components in an IMF. To avoid this problem, Wu and Huang [19] proposed EEMD based on noise-assisted data analysis method.

The EEMD process for signal $x(t)$ is as follows:

- (1) Add a white noise with amplitude α to the signal $x(t)$.
- (2) The signal with noise is analyzed by EMD.
- (3) Repeat the above steps N times and average the results of EMD.

The difference between the input signal and the corresponding IMF is called the final standard deviation of error, which is expressed by e . The added white noise satisfies the following rule [19]:

$$e = \frac{\alpha}{\sqrt{N}}, \quad (11)$$

where α is the amplitude of the added white noise and N is the number of ensemble members.

3.1.2. Selection of EEMD Key Parameters. If the amplitude of the white noise is too small, the mixing of the modes cannot be weakened. On the contrary, the final standard deviation of error will be large. If the number of ensemble members is too small, the influence of added white noise cannot be

eliminated; in contrast, the calculation cost will be increased. Therefore, it is very important to select suitable amplitude of the white noise and number of ensemble members when EEMD is employed to analyze signals. The amplitude of white noise is defined as

$$\alpha = k \cdot \sigma, \quad (12)$$

where σ is the standard deviation of the signal and k is a coefficient.

The purpose of added white noise is to improve the distribution of extreme points of signal. The extreme point distribution index is defined as

$$SI = \sqrt{S_1^2 + S_2^2 + S_3^2 + S_4^2}, \quad (13)$$

where S_1 is the standard deviation of amplitude interval of maximum points; S_2 is the standard deviation of coordinate interval of maximum points; S_3 is the standard deviation of amplitude interval of minimum points; and S_4 is the standard deviation of coordinate interval of minimum points.

The vibration acceleration of wheel with the condition of 10-meter rail corrugation is shown in Figure 6. White noise with different amplitudes is added to the signal, and the extreme point distribution index SI is calculated. It can be seen from Figure 7 that the extreme point distribution index SI tends to be stable when the amplitude of white noise increases to a certain value.

In this paper, the extreme point distribution index SI is used to determine the optimal range of white noise amplitude. Then, the added white noise amplitude α and the number N of ensemble members are selected, respectively, according to the orthogonal coefficient IO and equation (11). The parameter selection algorithm of EEMD is shown in

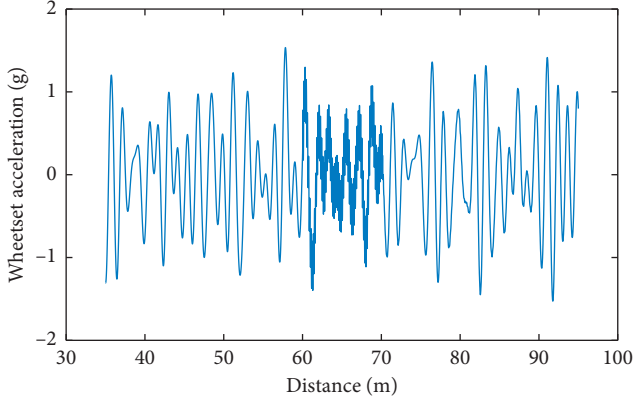


FIGURE 6: Vibration acceleration signal of wheel.

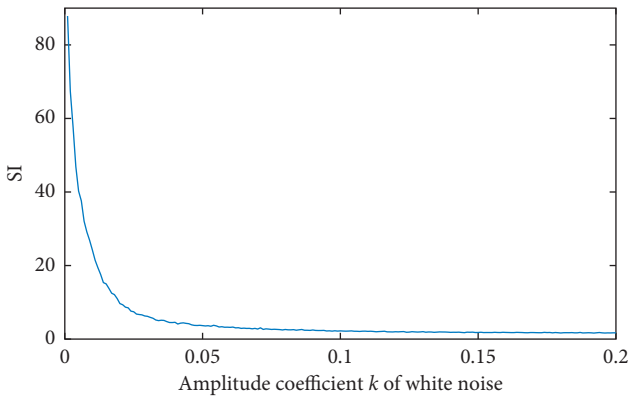


FIGURE 7: The extreme point distribution index SI.

Figure 8. Firstly, the optimum range of white noise amplitude is determined by the stability value of SI. In order to ensure that the amplitude of white noise can improve the distribution of signal extreme points, the minimum value of k is 0.001. The maximum value of k is set to be 0.01 so that the optimization range is not too small. In order to select the appropriate amplitude of white noise, it is necessary to determine the number of ensemble members in advance. The number N of ensemble members should not be too large; otherwise, the calculation time is very long. If N is too small, EEMD will be invalid. After many trials, N is initially set to be 10. EEMD analyses of the signal are carried out in the optimal range of white noise amplitude, and the decomposition results are evaluated by the orthogonal coefficients. The white noise amplitude corresponding to the optimal decomposition result is the best white noise amplitude α . In this paper, the error less than 1% can be acceptable. The final standard deviation of error is set to be 0.01. Then, the best N is determined according to the rules of the final standard deviation of error and the white noise amplitude. Meanwhile, the minimum value of N is 10 to avoid the EEMD invalidation caused by too small N .

The vibration acceleration signals of wheel in Figure 6 are analyzed by EMD and EEMD, respectively. Figure 9 shows the first four IMFs after decomposition. IMF components are arranged from high frequency to low frequency, so the first

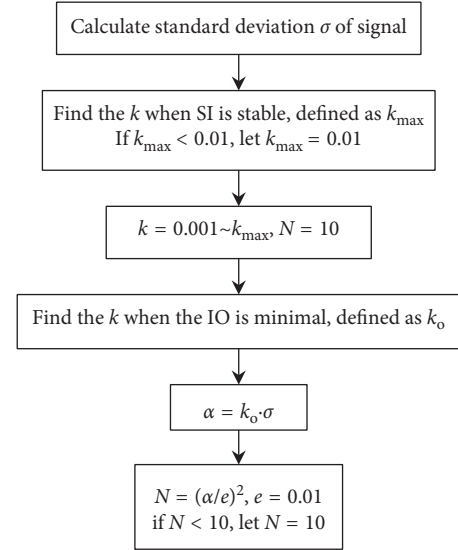


FIGURE 8: Selection algorithm of EEMD parameters.

IMF (IMF1) is the high-frequency component of the signal. It can be seen from Figure 9(a) that IMF1 of EMD analysis has low-frequency signals at other locations besides high-frequency signals caused by rail corrugation which indicates that there is mode mixing in EMD analysis. Apparently, the mode mixing will influence the detection results. In Figure 9(b), there is only the high-frequency components related with rail corrugation and no low frequency in IMF1. Therefore, EEMD analysis is an effective method to extract the part of the signal caused by rail corrugation.

3.1.3. Wavelength Calculation. After the IMFs are obtained by EEMD analysis, the IMFs are selected to eliminate the effects of noise and the random irregularity of the track. IMF selection and signal reconstruction algorithm are shown in Figure 10. The false components are eliminated by correlation analysis, and the high-frequency components are reconstructed into a high-frequency signal which is caused by rail corrugation.

Estimation of wavelength of rail corrugation by main frequency of the reconstructed signal y_r is expressed as

$$\lambda = \frac{v}{f_m}, \quad (14)$$

where v is train speed and f_m is the main frequency of the reconstructed signal, which can be obtained by FFT.

3.2. Features Extraction of Corrugation Depth. The vibration acceleration signals of wheel under rail corrugation are nonlinear, nonstationary, and non-Gaussian. Higher-order spectra are useful in analyzing nonlinearity and non-Gaussianity of the signal as it provides high noise immunity [20]. The frequency domain representation of third-order cumulants of signals is called bispectrum, which is expressed as

$$B(f_1, f_2) = E[X(f_1)X(f_2)X^*(f_1 + f_2)], \quad (15)$$

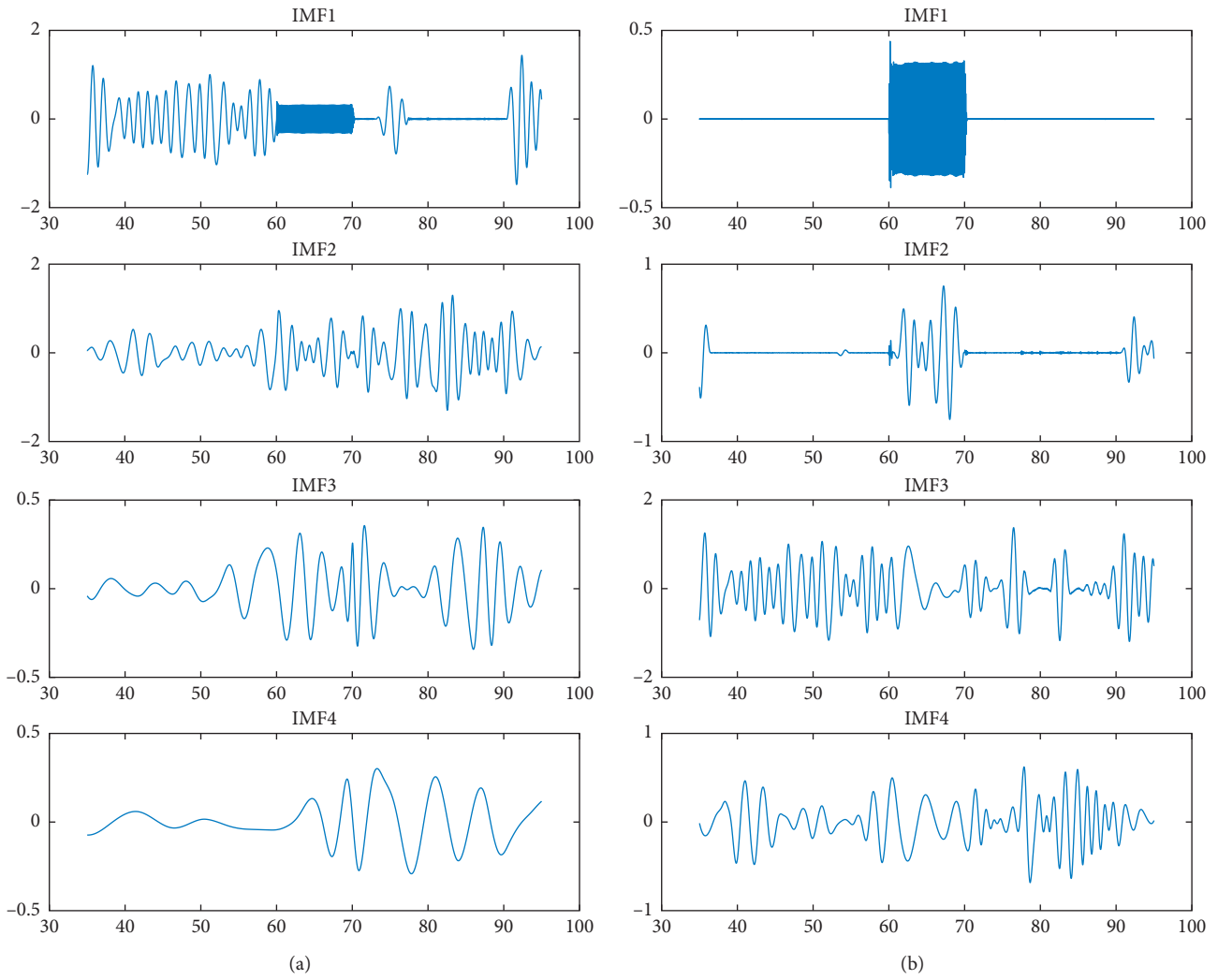


FIGURE 9: The first four IMFs of the signal. (a) EMD. (b) EEMD.

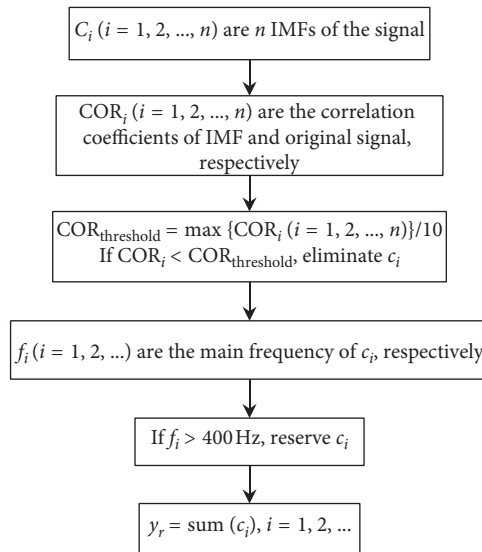


FIGURE 10: IMFs selection and signal reconstruction algorithm.

where $X(f)$ is the Fourier transform of the signal; * denotes complex conjugate; $E[\cdot]$ denotes the expectation operation; and the frequency f may be normalized by the Nyquist frequency to be between 0 and 1.

The discrete bispectrum matrix B is obtained by the high order spectral analysis of the reconstructed signal $y_r(t)$. The size of the bispectrum matrix B is $Q \times Q$. In order to recognize the depth of rail corrugation easily, bispectrum features need to be extracted.

Three amplitude features of bispectrum [21]:

$$\begin{aligned} \text{Amp}_1 &= \frac{1}{Q^2} \sum_{\Omega} |B(i, j)|, \\ \text{Amp}_2 &= \sum_{\Omega} \log(|B(i, j)|), \\ \text{Amp}_3 &= \sum_{i=1}^Q \log(|B(i, i)|). \end{aligned} \quad (16)$$

Three moment features of bispectrum [22]:

$$\begin{aligned} \text{Mom}_1 &= \sum_{i=1}^Q i \cdot \log(|B(i, i)|), \\ \text{Mom}_2 &= \sum_{i=1}^Q (i - M)^2 \cdot \log(|B(i, i)|), \\ \text{Mom}_3 &= \sum_{\Omega} \sqrt{i^2 + j^2} \cdot |B(i, j)|. \end{aligned} \quad (17)$$

Three entropy features of bispectrum [23]:

$$\text{Ent}_1 = - \sum_{\Omega} p_1(i, j) \cdot \log(p_1(i, j)), \quad (18)$$

where $p_1(i, j) = |B(i, j)| / \sum_{\Omega} |B(i, j)|$.

$$\text{Ent}_2 = - \sum_{\Omega} p_2(i, j) \cdot \log(p_2(i, j)), \quad (19)$$

where $p_2(i, j) = |B(i, j)|^2 / \sum_{\Omega} |B(i, j)|^2$.

$$\text{Ent}_3 = - \sum_{\Omega} p_3(i, j) \cdot \log(p_3(i, j)), \quad (20)$$

where $p_3(i, j) = |B(i, j)|^3 / \sum_{\Omega} |B(i, j)|^3$.

The above nine bispectrum features have different amplitudes at different rail corrugation depths, as shown in Figure 11. Three entropy features of bispectrum change nonlinearly with the increase of rail corrugation depth, while the other features of bispectrum increase with the increase of rail corrugation depth. The bispectrum features can well reflect the depth of rail corrugation.

The train speed and the wavelength of the rail corrugation also affect the vibration response of the wheel. Therefore, the train speed v and the estimated wavelength λ are also taken as the feature parameters. The extracted features are constructed into a features vector and classified using the SVM model.

4. Detection Result

4.1. Data Preparation. In the simulation model, the train speeds are 250 km/h to 350 km/h, the wavelengths of rail

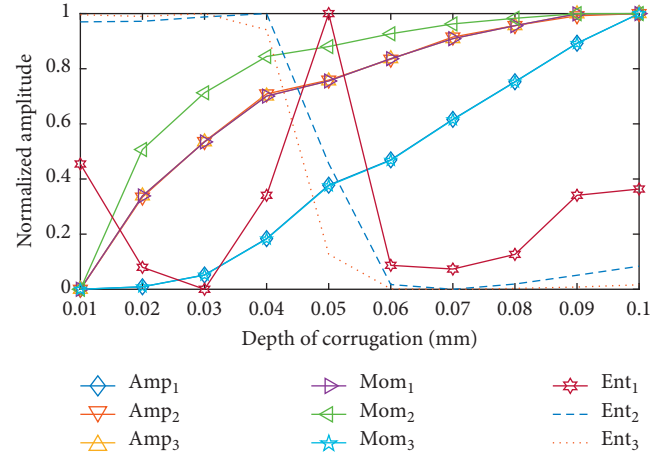


FIGURE 11: Bispectrum features at different depths of corrugation (train speed is 250 km/h and wavelength is 100 mm).

corrugation are 100 mm to 150 mm, and the depths of rail corrugation are 0.01 mm to 0.1 mm. There are 660 signals. After repeated 10 simulations, 6600 sets of vibration acceleration signals of wheel are obtained. The signal length is 60 m including 25 m before the wheel enters the rail corrugation and 25 m after it leaves the rail corrugation.

In order to verify the antinoise ability of the detection method, a Gaussian noise signal is added to the wheel acceleration signal to simulate the measurement noise.

$$x_{\text{measurement}} = x_{\text{simulation}} + E_p \times \{N\} \times \text{var}(x_{\text{simulation}}), \quad (21)$$

where E_p is the noise level; $\{N\}$ is a standard normal distribution vector with zero mean and unit standard deviation; and $\text{var}(\cdot)$ denotes the standard deviation of signal.

4.2. Wavelength Estimation of Rail Corrugation. The estimation results of rail corrugation wavelength are shown in Figure 12. It can be seen from Figure 12 that the wavelength of rail corrugation can be estimated at different corrugation depths and train speeds, and the noise has no effect on the estimation algorithm.

The relative error between the estimated value of wavelength and the true value of wavelength is defined as:

$$\text{error} = \frac{1}{n} \sum_{i=1}^n \frac{|\lambda_i^{\text{estimation}} - \lambda_i^{\text{true}}|}{\lambda_i^{\text{true}}}, \quad (22)$$

where n is the number of data samples.

In order to analyze the influence of corrugation depth on wavelength estimation, depths of 0.01 mm, 0.05 mm, and 0.1 mm rail corrugation are selected, respectively. The wavelength estimation results with 0%, 1%, 3%, and 5% noise levels are shown in Table 3. The wavelength estimation error of rail wavelength is almost unchanged under different depths, and the maximum value of wavelength estimation error is not more than 0.2%. The wavelength estimation errors are very small, which shows that the estimation of rail wavelength is completely reliable. Moreover, the simulation results show that the proposed method can estimate the

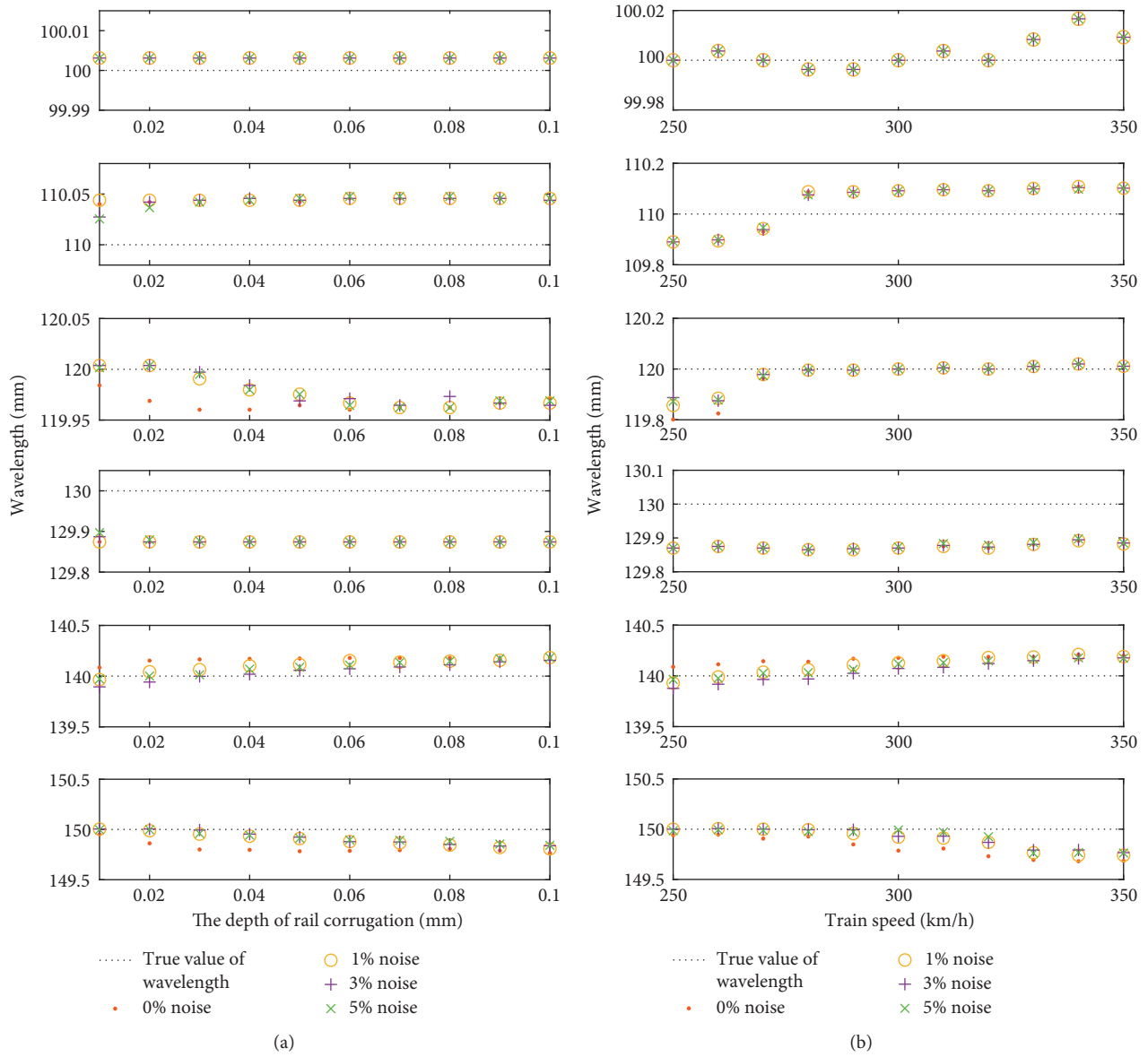


FIGURE 12: The estimation results of rail corrugation wavelength. (a) At different depths of rail corrugation. (b) At different train speeds.

TABLE 3: Wavelength estimation error at different depths of rail corrugation.

Case	Depth 0.01 mm				Depth 0.05 mm				Depth 0.1 mm			
	Nil	1%	3%	5%	Nil	1%	3%	5%	Nil	1%	3%	5%
100 mm	0.0045	0.0045	0.0045	0.0045	0.0045	0.0045	0.0045	0.0045	0.0045	0.0045	0.0045	0.0045
110 mm	0.0900	0.0897	0.0908	0.0910	0.0902	0.0900	0.0900	0.0899	0.0899	0.0899	0.0900	0.0899
120 mm	0.0205	0.0045	0.0045	0.0063	0.0367	0.0276	0.0330	0.0275	0.0313	0.0349	0.0367	0.0330
130 mm	0.0968	0.0968	0.0980	0.0994	0.0968	0.0968	0.0968	0.0968	0.0968	0.0968	0.0968	0.0968
140 mm	0.1252	0.1124	0.1001	0.1100	0.1347	0.1286	0.1230	0.1260	0.1360	0.1357	0.1329	0.1358
150 mm	0.0376	0.0045	0.0045	0.0087	0.1453	0.0623	0.0543	0.0601	0.1563	0.1293	0.1091	0.1068

wavelength well under the conditions of different depths and measurement noises.

The train speeds are 250 km/h, 300 km/h, and 350 km/h, and the wavelength of rail corrugation is estimated, respectively. The wavelength estimation results with 0%, 1%, 3%, and 5% noise levels are shown in Table 4. The

wavelength estimation error of rail wavelength is almost unchanged at different depths, and the maximum value of wavelength estimation error is not more than 0.25%. The wavelength estimation error is also very small, which indicates that the wavelength estimation effect of rail corrugation is very good. Meanwhile, the simulation results

TABLE 4: Wavelength estimation error at different train speeds.

Case	Train speed 250 km/h				Train speed 300 km/h				Train speed 350 km/h			
	Nil	1%	3%	5%	Nil	1%	3%	5%	Nil	1%	3%	5%
100 mm	0	0	0	0	0	0	0	0	0.0093	0.0093	0.0093	0.0093
110 mm	0.0999	0.0999	0.0999	0.0997	0.0834	0.0834	0.0834	0.0836	0.0927	0.0927	0.0927	0.0927
120 mm	0.1657	0.1198	0.0938	0.1058	0	0	0	0	0.0093	0.0093	0.0093	0.0093
130 mm	0.0999	0.0999	0.0999	0.0999	0.0999	0.0999	0.0999	0.1001	0.0907	0.0907	0.0910	0.0910
140 mm	0.1234	0.1070	0.1016	0.1107	0.1325	0.1275	0.1217	0.1265	0.1428	0.1412	0.1391	0.1386
150 mm	0.0399	0	0	0.0100	0.1421	0.0524	0.0474	0.0050	0.2124	0.1778	0.1616	0.1639

illustrate that the proposed method can estimate the wavelength excellent under the conditions of different train speeds and measurement noises.

4.3. Depth Classification of Rail Corrugation. According to the values of depth of rail corrugations, three depth levels are divided, as shown in Table 5.

Bispectrum features, estimated wavelength, and train speed are taken as inputs of SVM and depth level is taken as SVM output. The 80% of all simulation data is used to train the SVM model, and the remaining 20% is used for testing.

The classification results of rail corrugation depth level with different levels of noise are shown in Figure 13.

The reliability of the proposed method is evaluated by the accuracy of the test results. The ratio between the number of correct classification results and the number of total test samples is defined as the detection accuracy, which can be expressed as

$$\text{accuracy} = \frac{\text{Num}_{\text{correct}}}{\text{Num}_{\text{total}}} \times 100\%. \quad (23)$$

The detection results of depth level with 0%, 1%, 3%, and 5% noise levels are shown in Table 6. The detection accuracy is more than 99%, indicating that the extracted corrugation depth feature is effective. The proposed detection method has strong antinoise ability and still has high accuracy under different measurement noises.

5. Conclusion

Rail corrugation is a short-wavelength track irregularity excitation and accordingly causes high-frequency vibration response of wheel. A rail detection algorithm based on EEMD and bispectrum features is proposed using wheel vibration acceleration. Different frequency components of wheel vibration response are extracted with EEMD of wheel vibration acceleration signal. The parameters α and N of EEMD are optimized using the orthogonal coefficient IO and the extreme point distribution index SI, which reduces the mode mixing and calculation time of the decomposition. The main frequency is found after EEMD to calculate the wavelength. The depth detection is regarded as a classification problem with SVM. The high-frequency signal of rail corrugation is reconstructed through the selection of IMFs, by which not only the interference of track random irregularity is avoided but also noise influence. Bispectrum features, which are extracted from the

TABLE 5: Definition of depth levels of rail corrugation.

Depth levels	Depths of rail corrugation (mm)
Level 1	$a \leq 0.04$
Level 2	$0.04 < a \leq 0.07$
Level 3	$a > 0.07$

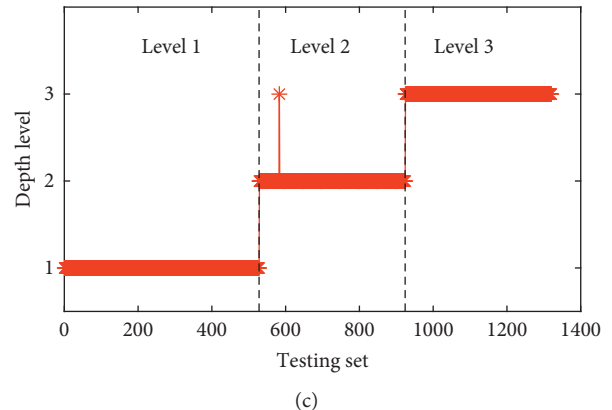
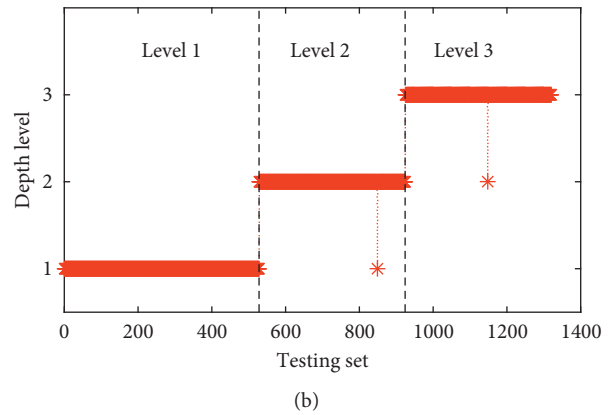
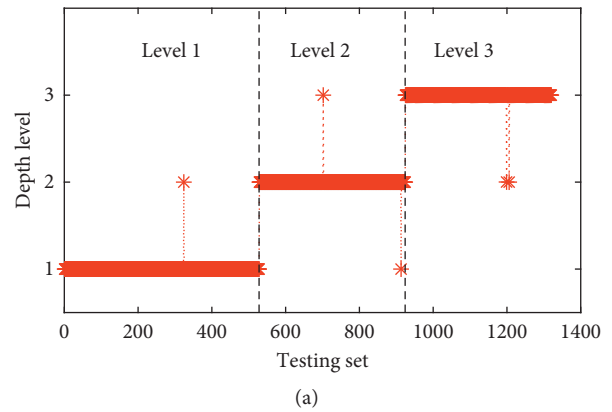


FIGURE 13: Continued.

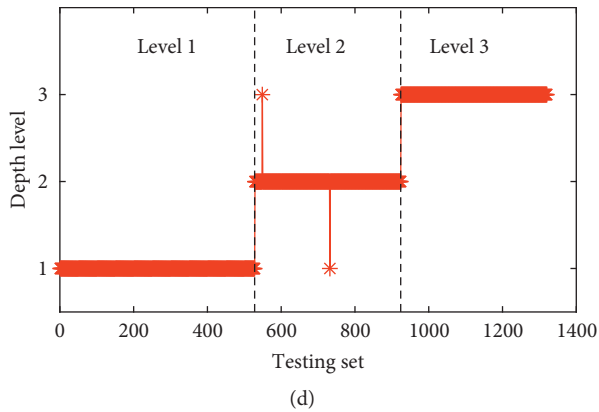


FIGURE 13: The classification results of rail corrugation depth level. (a) 0% noise. (b) 1% noise. (c) 3% noise. (d) 5% noise.

TABLE 6: The accuracy of depth level classification results at different measurement noises.

Noise level	Nil	1%	3%	5%
Accuracy of level 1 (%)	99.81	100	100	100
Accuracy of level 2 (%)	99.49	99.75	99.75	99.49
Accuracy of level 3 (%)	99.49	99.75	100	100
Total accuracy (%)	99.62	99.85	99.92	99.85

reconstructed signal, combining with train speed and the corrugation wavelength, are input into SVM. The numerical simulation results show the proposed detection algorithm can accurately identify the existence of rail corrugation. The error between the estimated wavelength and the real value is small, and the accuracy of corrugation depth level classification is high. And the results also represent robustness under different train speeds and measurement noises. The proposed rail corrugation detection method provides a feasible scheme for the in-service vehicle test in the future.

Data Availability

The data used to support the findings of this study are included within the article.

Conflicts of Interest

The authors declare that they have no conflicts of interest.

Acknowledgments

This work was supported by the National Key Research and Development Program of China under Grant no. 2016YFB1200401.

References

- [1] K. H. Oostermeijer, "Review on short pitch rail corrugation studies," *Wear*, vol. 265, no. 9-10, pp. 1231-1237, 2008.
- [2] Z. Q. Jiang, D. L. Si, W. Li et al., "On rail corrugation of high speed railway (in Chinese)," *China Railway Science*, vol. 35, no. 4, pp. 9-14, 2014.
- [3] B. M. Hopkins and S. Taheri, "Track health monitoring using wavelet," in *Proceedings of ASME 2010 Rail Transportation Division Fall Technical Conference*, pp. 9-15, Roanoke, VA, USA, October 2010.
- [4] M. Molodova, Z. Li, and R. Dollevoet, "Axle box acceleration: measurement and simulation for detection of short track defects," *Wear*, vol. 271, no. 1-2, pp. 349-356, 2011.
- [5] W. Huang, W. Zhang, Y. Du et al., "Detection of rail corrugation based on fiber laser accelerometers," *Measurement Science and Technology*, vol. 24, no. 9, article 094014, 2013.
- [6] S. Kaewunruen, "Monitoring of rail corrugation growth on sharp curves for track maintenance prioritisation," *International Journal of Acoustics and Vibration*, vol. 23, no. 1, pp. 35-43, 2018.
- [7] P. Salvador, V. Naranjo, R. Insa, and P. Teixeira, "Axlebox accelerations: their acquisition and time-frequency characterisation for railway track monitoring purposes," *Measurement*, vol. 82, pp. 301-312, 2016.
- [8] Z. Shen, Q. Wang, Y. Shen et al., "Accent extraction of emotional speech based on modified ensemble empirical mode decomposition," in *Proceedings of Instrumentation and Measurement Technology Conference*, Austin, TX, USA, May 2010.
- [9] W. Guo and P. W. Tse, "A novel signal compression method based on optimal ensemble empirical mode decomposition for bearing vibration signals," *Journal of Sound and Vibration*, vol. 332, no. 2, pp. 423-441, 2013.
- [10] X. Xue, J. Zhou, Y. Xu, W. Zhu, and C. Li, "An adaptively fast ensemble empirical mode decomposition method and its applications to rolling element bearing fault diagnosis," *Mechanical Systems and Signal Processing*, vol. 62-63, pp. 444-459, 2015.
- [11] M. Kedadouché, M. Thomas, and A. Tahan, "A comparative study between empirical wavelet transforms and empirical mode decomposition methods: application to bearing defect diagnosis," *Mechanical Systems and Signal Processing*, vol. 81, pp. 88-107, 2016.
- [12] W. Zhai and X. Sun, "A detailed model for investigating vertical interaction between railway vehicle and track," *Vehicle System Dynamics*, vol. 23, no. 1, pp. 603-615, 1994.
- [13] X. Lei and J. Wang, "Dynamic analysis of the train and slab track coupling system with finite elements in a moving frame of reference," *Journal of Vibration and Control*, vol. 20, no. 9, pp. 1301-1317, 2013.
- [14] W. Zhai, K. Wang, and C. Cai, "Fundamentals of vehicle-track coupled dynamics," *Vehicle System Dynamics*, vol. 47, no. 11, pp. 1349-1376, 2009.
- [15] X. Kang, X. B. Liu, H. Y. LI et al., "PSD of ballastless track irregularities of high-speed railway (in Chinese)," *Scientia Sinica Technologica*, vol. 44, no. 7, pp. 687-696, 2014.
- [16] K. Wang, P. Liu, W. Zhai, C. Huang, Z. Chen, and J. Gao, "Wheel/rail dynamic interaction due to excitation of rail corrugation in high-speed railway," *Science China Technological Sciences*, vol. 58, no. 2, pp. 226-235, 2015.
- [17] C. C. Chang and C. J. Lin, "LLIBSVM: a library for support vector machines," *ACM Transactions on Intelligent Systems and Technology*, vol. 2, no. 3, pp. 1-27, 2011.
- [18] N. E. Huang, Z. Shen, S. R. Long et al., "The empirical mode decomposition and the Hilbert spectrum for nonlinear and non-stationary time series analysis," *Proceedings of the Royal Society A-Mathematical Physical and Engineering Sciences*, vol. 454, no. 1971, pp. 909-995, 1998.

- [19] Z. Wu and N. E. Huang, "Ensemble empirical mode decomposition: a noise-assisted data analysis method," *Advances in Adaptive Data Analysis*, vol. 1, no. 1, pp. 1–41, 2009.
- [20] L. W. Jian and T.-C. Lim, "Automated detection of diabetes by means of higher order spectral features obtained from heart rate signals," *Journal of Medical Imaging and Health Informatics*, vol. 3, no. 3, pp. 440–447, 2013.
- [21] R. Yuvaraj, M. Murugappan, N. Mohamed Ibrahim et al., "Detection of emotions in Parkinson's disease using higher order spectral features from brain's electrical activity," *Biomedical Signal Processing and Control*, vol. 14, pp. 108–116, 2014.
- [22] C.K.Y., M. Hariharan, R. Ngadiran, A. H. Adom, S. Yaacob, and K. Polat, "Hybrid BBO_PSO and higher order spectral features for emotion and stress recognition from natural speech," *Applied Soft Computing*, vol. 56, pp. 217–232, 2017.
- [23] L. Saidi, J. Ben Ali, F. Fnaiech et al., "Application of higher order spectral features and support vector machines for bearing faults classification," *ISA Transactions*, vol. 54, pp. 193–206, 2015.

Research Article

Seismic Resistance and Displacement Mechanism of the Concrete Footing

Abdoullah Namdar  and Yun Dong 

Faculty of Architecture and Civil Engineering, Huaiyin Institute of Technology, Huai'an, China

Correspondence should be addressed to Yun Dong; hadyun@163.com

Received 2 November 2018; Revised 17 December 2018; Accepted 15 January 2019; Published 6 February 2019

Guest Editor: Krzysztof Holak

Copyright © 2019 Abdoullah Namdar and Yun Dong. This is an open access article distributed under the Creative Commons Attribution License, which permits unrestricted use, distribution, and reproduction in any medium, provided the original work is properly cited.

A realistic seismic simulation of the concrete footing has been made by using finite element method (FEM) software called ABAQUS. The effect of concrete footing embedment in soil on concrete footing-soil foundation interaction has numerically been simulated for considering displacement, stress, strain, and seismic acceleration load response at the base of a concrete footing. The results showed that the height of embedded concrete footing in soil foundation controls (i) mechanism and magnitude of lateral, vertical, and differential displacements of the concrete footing, (ii) strain energy, the acceleration load response, and stress paths, and (iii) concrete footing-soil foundation interaction. Compared with various theoretical and experimental results reported in the literature, the present study provides realistic seismic behavior of concrete footing-soil foundation interaction.

1. Introduction

From the available literature [1–9], it is demonstrated that the displacement of soil foundation is very important in the design of view to construct a stable infrastructure. There are several analytical, experimental, and numerical investigations for understanding the static and dynamic response of soil. In order to investigate the failure mitigation of soil foundation, soil bearing capacity, and soil improvement [1–3], several analytical investigations were reported. The differential settlement and seismic mitigation of embankment models were studied [4, 5]. The displacement of concrete footing was numerically analyzed using ABAQUS [6], and the dynamic behavior of soil foundation during liquefaction was reviewed [7]. ABAQUS software is used in simulation displacement of reinforced rock-soil slopes [8], and FLAC-3D software is employed for numerically simulating displacement and shear strain of sandy soil subjected to cyclic loading [9]. In all the methods, the static, dynamic, and seismic response of whole soil mass or soil models is investigated. On the contrary, in many projects, the improvement of soil needs to be done if the soil cannot provide enough bearing capacity and strength to sustain the applied

load on the soil. The most common soil improvement techniques are reinforcing, grouting, densification, deep mixing, and drainage. Inattention to the complexity of static, dynamic, and seismic behaviors of soil, it requires to investigate and soil load response in specific cross-section of soil for accurate soil improvement process. On the contrary, only the subsoil analysis will not perfectly support the soil foundation and concrete foundation design.

In the present study, the ABAQUS is used for study displacement of the concrete footing. The analysis was done by using a new technique in numerical analysis. There is not any numerical analysis report by using ABAQUS on the seismic concrete footing-soil foundation interaction with considering the vertical and horizontal displacement of concrete footing, strain, stress, and seismic acceleration load response at the underneath concrete footing, while the height of embedded concrete footing in a soil foundation is varied for each model, and the model was subjected to seismic loading. In this investigation, the numerical analysis was performed to provide a realistic understanding of a complex geotechnical engineering problem. The seismic vertical, horizontal, and differential displacements mechanisms of concrete footing are evaluated for all the models

with attention to concrete footing-soil interaction. In the present work, the numerical analysis is unique, it is due to the development of cycling graphs by using ABAQUS, and the results exactly depict the seismic behavior of the models. The numerical results obtained from this study are compared with those that are available in the literature.

2. Problem Definition

At present investigation, the influence of concrete footing height embedded in the layered soil has been evaluated. The single concrete footing is placed on and inside soil foundation. The seismic behavior of concrete footing-soil interaction complicates; however, modeling concrete footing-soil interaction with using suitable techniques helps to realize this problem. It is assumed that the soil medium obeys the Mohr–Coulomb failure criterion and an associated flow rule, and this concept was applied in numerical analysis with considering mechanical properties of soil and concrete. The concrete footing and soil foundation are loaded simultaneously in one step in numerical analysis to have vertical and horizontal displacements simultaneously. The numerical analysis was performed to determine (i) seismic acceleration load response versus vertical displacement at the base of concrete footing, (ii) seismic acceleration load response versus stress and strain at the base of concrete footing, (iii) lateral displacement of concrete footing, and (iv) the stress-strain curve at the base of concrete footing. However, from the solution available in the literature is understood [10], lateral displacement of concrete footing reduces with increasing height of embedded concrete footing in the soil foundation. The results of numerical analysis influence soil-structure interaction. The suitable aspects in concrete footing-soil foundation design are well understood, and a valid analysis method is used in respect to literature analysis.

3. Modeling and Materials

The model is subjected to the realistic seismic load. The boundary condition, the nature of applied load, and mechanical properties of soil in all the models are assumed to be same. The mechanical properties of the materials and the seismic load are shown in Table 1 and Figures 1–3, respectively. In the present study, the earthquake data are collected from the United States Geological Survey (USGS) and Center for Engineering Strong Motion Data (CESMD). The earthquake data were recorded by Forca Canapine station, and this station is located in 11.7 km distance from the epicenter of the earthquake. The northern Norcia Italy earthquake has been occurred with 6.6 magnitudes, at the location of 42.85°N 13.09°E, and depth of 10.0 km, on 07:16:03 UTC, 30 Oct 2016. ABAQUS software has the ability to simulate the seismic acceleration load and apply realistic seismic load on the model in numerical analysis. The ABAQUS is based on the Lagrangian formulation. To simulate concrete footing-soil foundation interaction, the three different models are developed, and in each model, the level of embedment footing in soil is different. In the first model, the concrete footing is placed on soil foundation, and

it is not embedded in the soil foundation. In the second model, half of the concrete footing is embedded in the soil foundation. In the third model, whole concrete footing is embedded in the soil foundation, and it is shown in Figure 4. The full height of the concrete footing is 30 cm. In the numerical simulation, the dimensions of concrete footing are 70 cm width * 70 cm length * 30 cm height. The dimensions of the soil foundation are 150 cm width * 150 cm length * 90 cm height. The ABAQUS has the ability to depict dynamic response at any part of a model. Depict dynamic response at a cross-section in a model is a new achievement in this research work, and it has not been reported in the literature previously. However, the seismic response between bases of concrete footing with soil foundation is not explained in the literature. The modeling of the three-dimensional concrete footing is important to capture the true seismic response under accurate boundary condition.

4. Numerical Analysis, Discussion, and Verification of the Results

The investigation on concrete footing-soil foundation interaction at the base of the concrete footing is essential for the analysis and design of infrastructure seismic stability. To analyze concrete footing-soil foundation interaction, an accurate model is made. This modeling is capable of simulating seismic concrete footing-soil foundation interaction at the base of the concrete footing. The model is able to capture the three-dimensional seismic response. The numerical results for seismic acceleration load response versus displacement at the base of a concrete footing, during concrete footing-soil foundation seismic interaction, have been provided in Figures 5–7. Due to the high variation of models of seismic response, different scales have been selected for graphs. The stiffness of the soil foundation is responsible for developing displacement. The level of loading, unloading, and reloading has been investigated for all the models. The seismic acceleration load response reached to zero in the unloading process, and in reloading, it increases up to the maximum level, and it is shown in Figures 5–7. When the model is subjected to seismic loading, unloading, and reloading in all the three phases of the loading mechanism, the displacement shows with different shapes. In the unloading phase, the displacement is zero, while in loading and reloading phases, the displacements reached the maximum level with two different directions. This displacement mechanism is developed due to the nature of the seismic load is applied to the model. The seismic loading is transferred to the bottom of the concrete footing, and it leads to seismic acceleration load response. The results of numerical simulation explained that the ABAQUS is able to compute nonlinear analysis. The seismic acceleration load response is distributed within the concrete footing base in contrast with the displacement pattern. The smaller seismic acceleration load response is observed with fully embedded concrete footing in the soil foundation. The differential displacement of the concrete footing was reduced with increasing depth of the concrete footing in the soil foundation. The seismic load acting at the base of a concrete footing was

TABLE 1: Soil and concrete mechanical properties [11, 12].

Soil type	Modulus elasticity, E (MPa)	Poisson's ratio, ν	Friction angle, ϕ (degree)	Dilatancy angle, ψ (degree)	Cohesion, c (kPa)	Unit weight, γ (kN/m ³)	Ref.
Soil	5	0.36	35	20	20	12.2	[11]
Concrete	49195	0.24	—	—	—	24.405	[12]

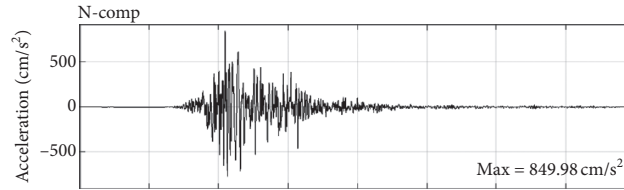


FIGURE 1: Acceleration history, northern Norcia Italy earthquake of 30 Oct 2016 [13].

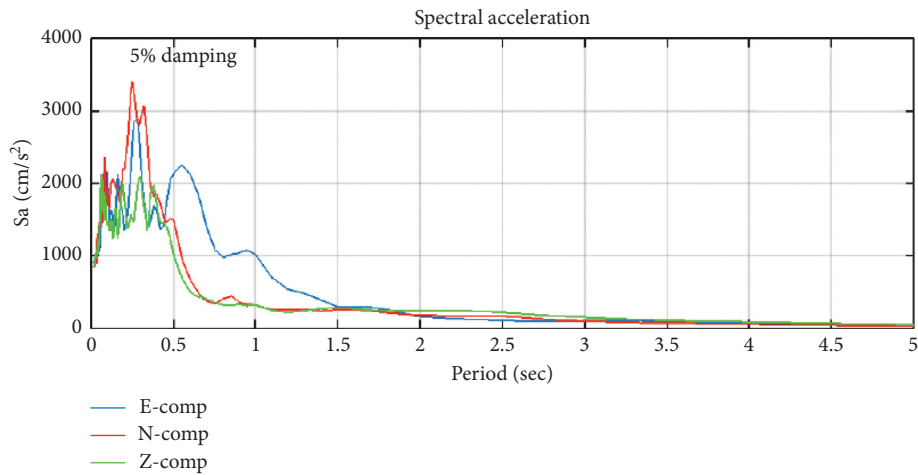


FIGURE 2: Spectral acceleration history, northern Norcia Italy earthquake of 30 Oct 2016 [13].

developing differential displacement with different mechanisms and magnitudes. The seismic load plays a crucial role in developing the ground displacement mechanism, and it has a direct relationship with damage caused by an earthquake. The failure of concrete footing due to high differential displacement is more possible if the concrete footing is placed over the soil foundation. With embedment of concrete footing in the soil foundation, the failure of concrete footing due to differential displacement was reduced.

The numerical results for seismic acceleration load response versus strain at the base of a concrete footing during concrete footing-soil foundation have seismic interaction which is shown in Figures 8–10. The strain level of a model is evaluated with respect to seismic acceleration load response. With the reduction of strain, the stiffness of soil increases and damping ratio decreases; all of this process directly is depend on seismic acceleration load response. The cyclic strength of soils is determined numerically with a focus on the propagation of seismic waves, considering small strain and inelastic behavior of soil foundation at beneath of concrete footing. The permanent deformation and reduction strength of soil foundation are expecting in the first model when the concrete footing is placed over the soil foundation

and concrete footing is not embedded in the soil foundation. On the contrary, with the half and full embedded concrete footing in the soil foundation, the possibility for permanent deformation and reduction strength of the soil foundation is reduced significantly. The location of the embedment concrete footing in the soil foundation governs seismic energy dissipation. The strain rate sensitivity is analyzed by evaluating seismic acceleration load response, and it supports in understanding differential displacement of the concrete footing.

The numerical results for shear stress versus shear strain at the base of a concrete footing, during concrete footing-soil foundation interaction, are shown in Figures 11–13. The graphs show, with increased depth of embedment concrete footing in the soil foundation, the shear stress and shear strain were reduced, and they behave smoother with smaller magnitude. It can understand that, with increasing embedment of concrete footing in the soil foundation, the vibration of the concrete footing is significantly reduced. The results show that the stress buildup strain energy in the base of the concrete footing leads to releasing the strain energy in the form of vibration and causes deformation of the model. After applied seismic load on the model, the concrete footing

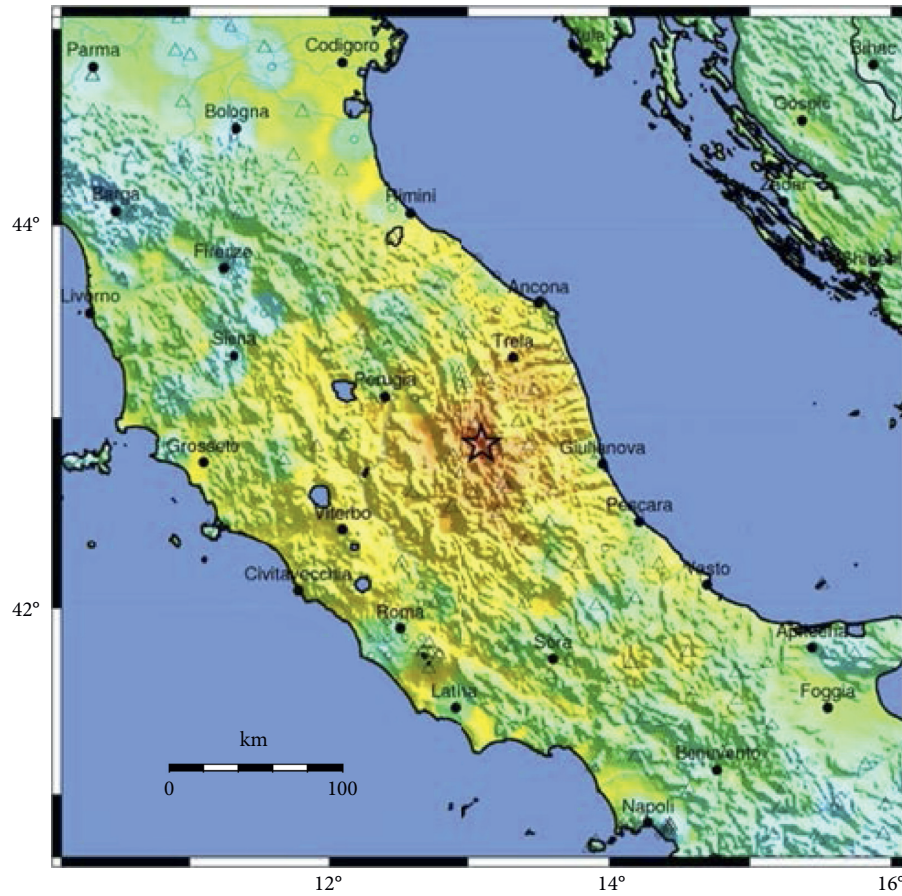


FIGURE 3: ShakeMap, northern Norcia Italy earthquake of 30 Oct 2016 [13].

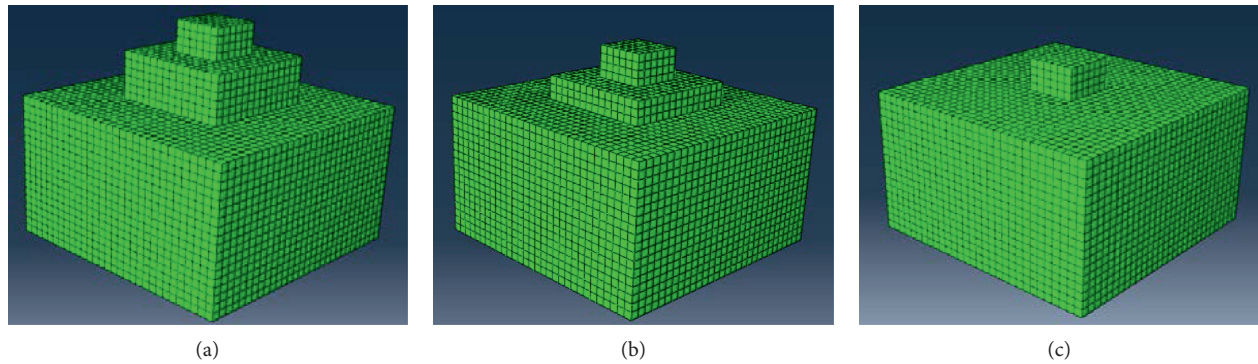


FIGURE 4: Concrete footing-soil models. (a) Footing not embedded. (b) Half of the footing is embedded. (c) Full of the footing is embedded.

is displaced. The level of the concrete footing displacement depends on the level of releasing strain energy and strength of soil foundation. If the strength of soil foundation is the same in all the models, the strain energy plays important role in the displacement of the concrete footing. On the contrary, the level of strain energy depending on the location of the concrete footing is embedded in the soil foundation. Each model is capable to produce different amounts of strain energy after seismic loading is applied to the model. The geometry of the model is a factor in the production level of strain energy. It can be understood that the concrete footing

geomorphology has an important function in releasing strain energy, and it influences on earthquake zone differently. However, the stability of a structure is different at any location when the structure is subjected to seismic loading. If two structures with the same strength and geometry are located nearby, but in distance between the two structures, the geomorphology changes significantly, the structure seismic response is too different. The level of strain energy is influenced on the variability damping ratio of a model. With fully embedment concrete footing in the soil foundation, the damping ratio and natural frequency are reduced. The lateral

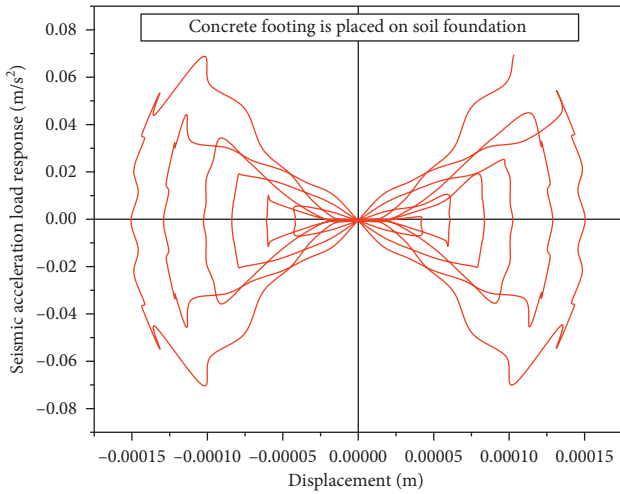


FIGURE 5: Seismic acceleration load response vs displacement at the base of a concrete footing, during concrete footing-soil foundation interaction.

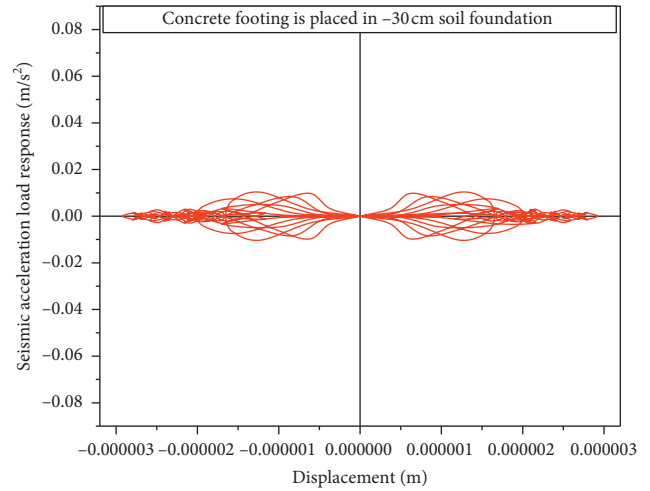


FIGURE 7: Seismic acceleration load response vs displacement at the base of a concrete footing, during concrete footing-soil foundation interaction.

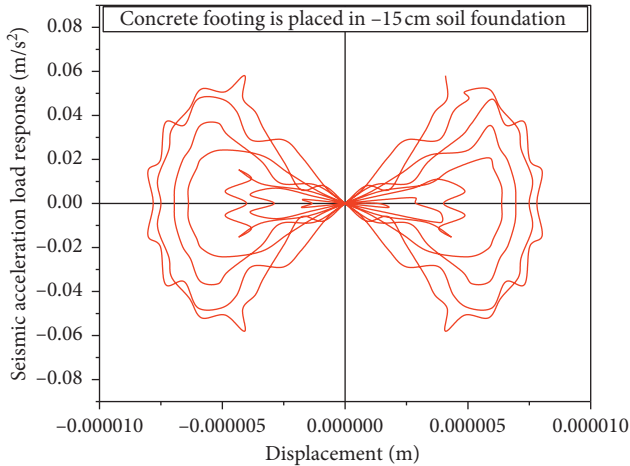


FIGURE 6: Seismic acceleration load response vs displacement at the base of a concrete footing, during concrete footing-soil foundation interaction.

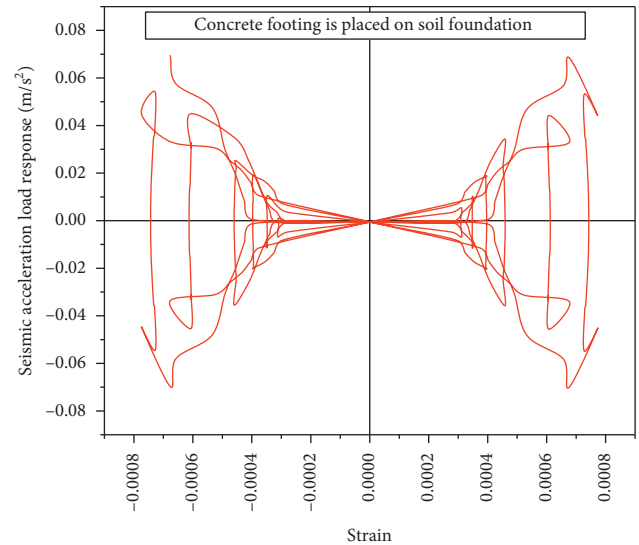


FIGURE 8: Seismic acceleration load response vs strain at the base of a concrete footing, during concrete footing-soil foundation interaction.

strength of the concrete footing increases with full embedment of the concrete footing in the soil. It is due to the strain energy distributed. In the model fully embedded with concrete footing in the soil foundation, the shape of the strain energy is converted from point loading to distribute loading, while the magnitude of strain energy does not change. The shape of the strain energy has a direct relationship with a vertical and horizontal displacement of the concrete footing.

Seismic acceleration load response versus stress at the base of a concrete footing during concrete footing-soil foundation interaction is shown in Figures 14–16. The seismic acceleration load response changes with the distribution of vertical and horizontal seismic stresses are applied to the whole model, and this phenomenon is shown in Figures 14–16. It is based on elastic soil interaction with solid concrete footing. The minimum level of stress is developed in a fully embedded concrete footing in the soil foundation.

The numerical results for lateral displacement of a concrete footing with considering concrete footing-soil foundation seismic interaction are illustrated in Figure 17. Figure 17 shows that the lateral displacement is reduced with an increase in the concrete footing embedment level in the soil foundation. It is required to indicate that the level of the embedded concrete footing in soil foundation directly affects on concrete footing differential displacement magnitude and mechanism. The mechanism of lateral displacement is not linear in all the models. In all the three models, the magnitude of the displacement drops to zero, during the direction of seismic loading is changed. The seismic loading has three steps: loading, unloading, and reloading. In unloading steps, the load reached zero. The results of numerical simulation have good agreement with the concept of

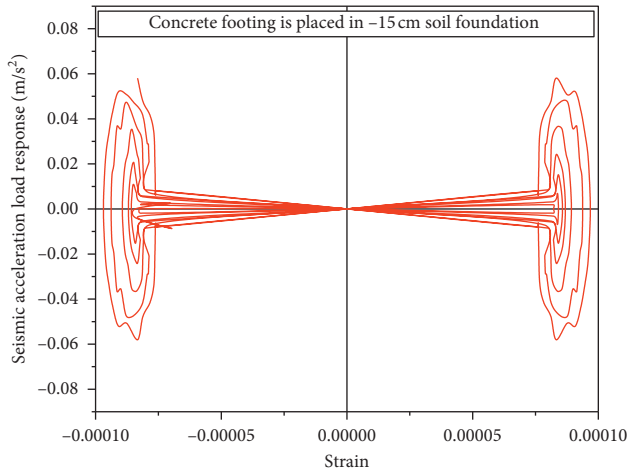


FIGURE 9: Seismic acceleration load response vs strain at the base of a concrete footing, during concrete footing-soil foundation interaction.

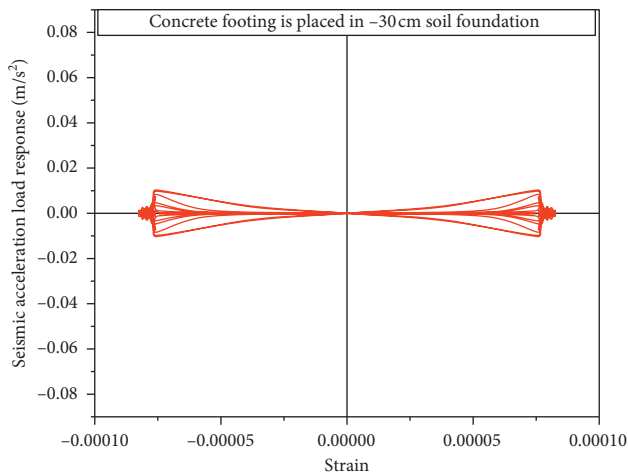


FIGURE 10: Seismic acceleration load response vs strain at the base of a concrete footing, during concrete footing-soil foundation interaction.

seismic loading nature. The lateral displacement changes (i) with smooth movement at the base of the concrete footing and (ii) marginally smaller than for fully embedded concrete footing. However, due to the faster release of the lateral loading to zero, for a fully embedded concrete footing in soil foundation, the value of loading frequency is reduced, and less shaking has been observed at the model with fully embedded concrete footings in soil foundation. The magnitude and mechanism of lateral displacement change with respect to the location of a concrete footing is embedded in the soil foundation.

The validation of SSI analysis through field data has been difficult, due to the lack of well-documented and instrumented structures subjected to earthquakes [11]. The suitable three-dimensional models have been made to explain the concrete footing-soil foundation interaction, during the model is subjected to realistic seismic loading. It is observed that the seismic loading response of each model, at any

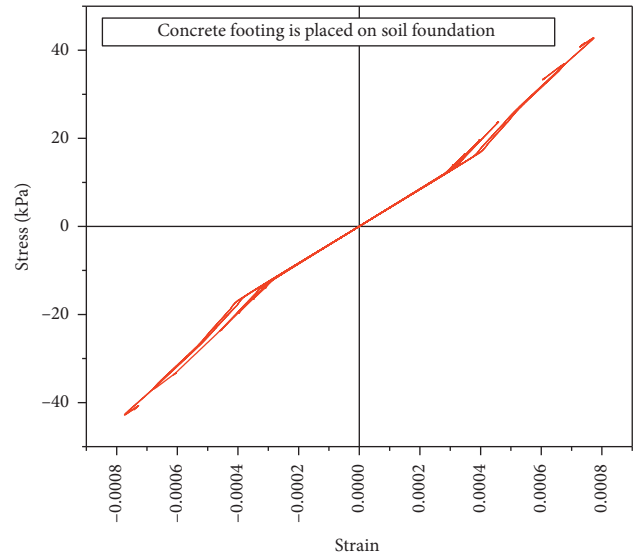


FIGURE 11: Shear stress vs shear strain at the base of a concrete footing, during concrete footing-soil foundation interaction.

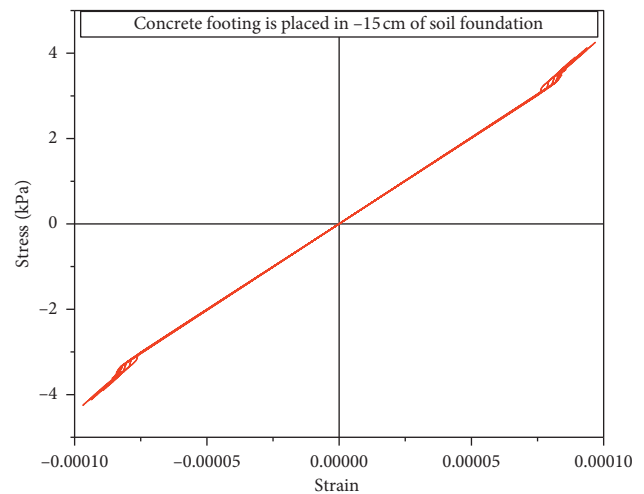


FIGURE 12: Shear stress vs shear strain at the base of a concrete footing, during concrete footing-soil foundation interaction.

cross-section of concrete footing and soil foundation, is not the same. This phenomenon leads to the occurrence of different concrete footing-soil foundation interaction mechanisms horizontally and vertically. This phenomenon leads to the occurrence of different displacement mechanisms at each direction and cross-sections of the model, as shown in Figures 5–16. However, for studying the concrete footing differential displacement mechanism, the concrete footing-soil interaction at the base of the concrete footing have numerically been investigated. Figure 18 shows that the horizontal displacement resonance curves at the foundation bottom forced vibration test [10]. Figure 17 shows the lateral displacement for a concrete footing, during concrete footing-soil foundation interaction. Figure 18 shows the horizontal displacement resonance curves at foundation bottom, forced vibration test. In comparing the results of the numerical simulation with those that are reported in the

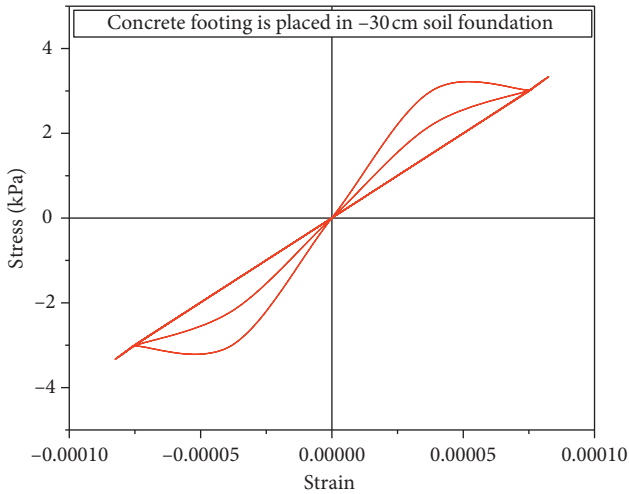


FIGURE 13: Shear stress vs shear strain at the base of a concrete footing, during concrete footing-soil foundation interaction.

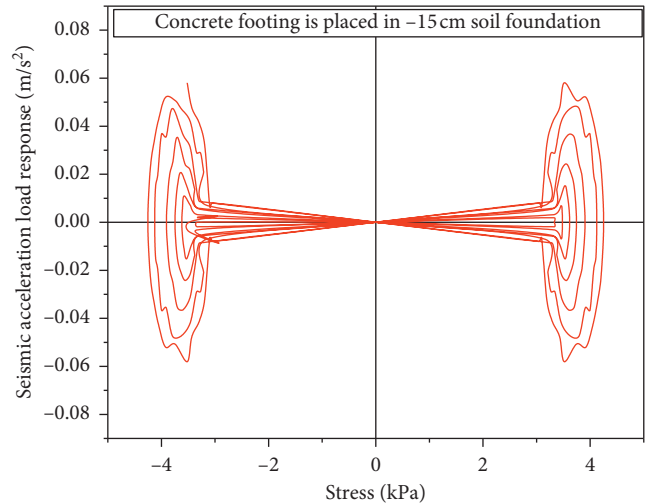


FIGURE 15: Seismic acceleration load response vs stress at the base of a concrete footing, during concrete footing-soil foundation interaction.

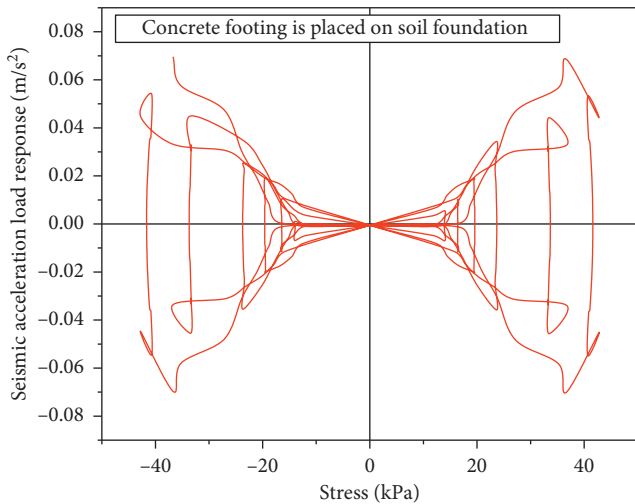


FIGURE 14: Seismic acceleration load response vs stress at the base of a concrete footing, during concrete footing-soil foundation interaction.

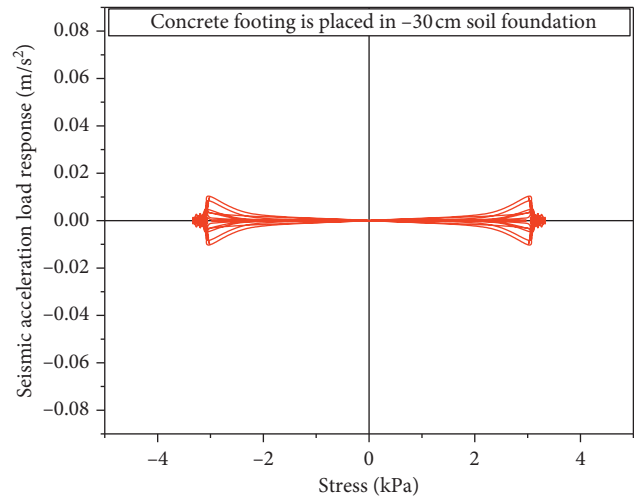


FIGURE 16: Seismic acceleration load response vs stress at the base of a concrete footing, during concrete footing-soil foundation interaction.

literature, it has been understood that the results of the numerical simulation are in good agreement with those that are reported in the literature. In this three-dimensional numerical simulation, the displacement mechanism at horizontally and vertically directions for all models plays a key role to explain the complexity of the concrete footing-soil interaction. The stability of concrete footing depends on the realistic result of the numerical analysis. The results of the present study demonstrate that the modeling of concrete footing-soil foundation interaction supports solving a geotechnical engineering problem is related to the differential displacement mechanism of the concrete footing. The results have shown that the model can capture the essential displacement mechanisms with considering both the vertical and horizontal differential displacement of soil foundation.

In the load-strain mechanism, only the part of the strain energy corresponding to the linear elastic response is

recovered [14]. On the contrary, the load transferring mechanism has been investigated using numerical analysis and experimental works with considering the strength of materials and shape of the modeling [15–18], and this phenomenon significantly influences on concrete footing-soil foundation interaction. But due to characteristics of soil during loading, unloading, and reloading process, and change compression loading to tensile loading in very short times, the crack on soil due to tensile loading and fatigue of soil cannot be explained same as which is presented in the literature, about crack and fatigue on metal [19–21]. The failure pattern and shear resistance of soil have been discussed using mathematical modeling techniques and numerical simulation [22–27], and the bearing capacity and effective stress have been changing with respect to soil foundation displacement. There are special techniques in numerical simulation [6, 14, 22, 26, 28].

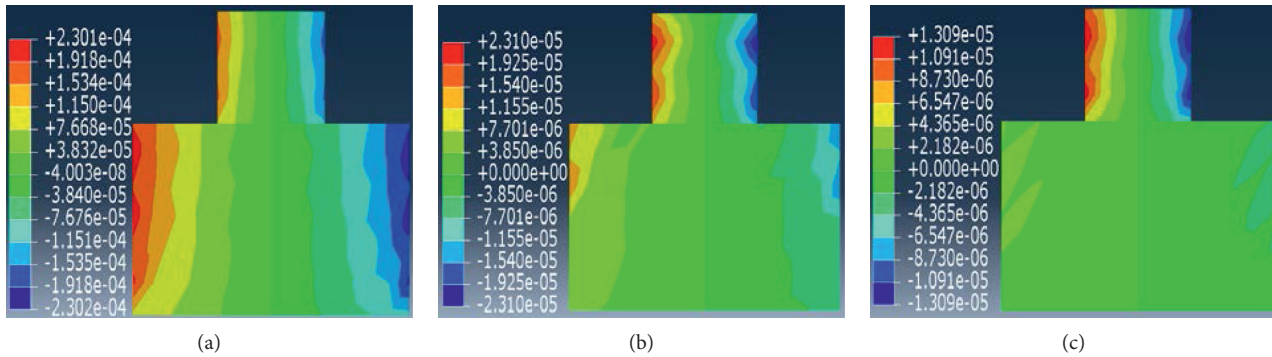


FIGURE 17: Lateral displacement of a concrete footing, during concrete footing-soil foundation interaction. (a) Footing not embedded. (b) Half of the footing embedded. (c) Full of footing embedded.

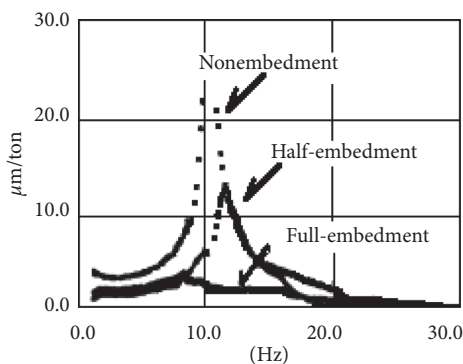


FIGURE 18: Comparison of displacement resonance at foundation bottom [10].

In the present study, cyclic graphs have been developed for understanding concrete footing displacement using ABAQUS which never has been reported in the literature.

5. Conclusion

In this study, a procedure for the 3D finite element analysis on the concrete footing-soil foundation model is made for understanding concrete footing-soil foundation seismic interaction. It has been attempted to simulate concrete footing-soil interaction during model that is subjected to realistic seismic loading. The results of the numerical analysis show that the height of concrete footing is embedded in the soil influences on seismic behavior of concrete footing and govern concrete footing-soil interaction, and it results in displacement magnitude and mechanism of the concrete footing.

- (i) The acceleration seismic load response-strain and stress at the base of the concrete footing is changed in respect to concrete footing-soil interaction. The concrete footing-soil interaction is minimized deformation of soil and is enhanced concrete footing stability. The acceleration seismic load response at the base of concrete footing can be controlled with installing concrete footing in the appropriate location of the soil foundation.

- (ii) The acceleration load response-displacement at the base of the concrete footing is not the same for all the three models.
- (iii) The lateral and vertical displacements of the concrete footing are reduced with an increase in concrete footing embedment height in the soil.
- (iv) The differential displacement of the concrete footing is reduced with an increase in concrete footing embedment height in the soil.
- (v) After applying a seismic load to the model, the concrete footing is displaced, the level of displacement depending on the level of releasing strain energy. Each model is capable to produce different amounts of strain energy. The geometry of the model is a factor affecting on the level of the strain energy.
- (vi) The results have good agreement with those that have been reported in the literature.

Data Availability

The data used in this paper have been collected from the literature, and the references that support the data used in numerical analysis are cited as [11–13]. The mechanical properties of materials used are those reported in the literature (Table 1). Figures 1–3 show the seismic load has been collected from the literature and applied in numerical simulation. In the present study, the earthquake data are collected from United States Geological Survey (USGS), Center for engineering strong motion data (CESMD). The earthquake data are used as reported by the Forca Canapine station; this station is located at 11.7 km distance from the epicenter of the earthquake. The northern Norcia Italy earthquake occurred with the magnitude of 6.6, at the location of 42.85°N and 13.09°E and depth of 10.0 km, on 07:16:03 UTC, 30 Oct 2016 (Figures 1–3). ABAQUS software has the ability to simulate seismic acceleration load and apply realistic seismic load on the model in numerical analysis.

Conflicts of Interest

The authors declare that they have no conflicts of interest.

Acknowledgments

The support by the Major Projects of Natural Science Research in Jiangsu Colleges and Universities (Grant no. 17KJA560001), the Science and Technology Planning Project of Jiangsu Province (Grant no. BY2016061-29), the Jiangsu Province Six Talent Peak High-level Talent Project (Grant no. JZ-011), and the New wall Materials and Development of Bulk Cement Projects of Jiangsu Economic and Information Commission (Grant no. 2017-21) is greatly acknowledged.

References

- [1] A. Namdar and X. Feng, "Evaluation of safe bearing capacity of soil foundation by using numerical analysis method," *Frattura ed Integrità Strutturale*, vol. 8, no. 30, pp. 138–144, 2014.
- [2] A. Namdar and M. K. Pelkoo, "Numerical analysis of soil bearing capacity by changing soil characteristics," *Frattura ed Integrità Strutturale*, vol. 3, no. 10, pp. 38–42, 2009.
- [3] A. Namdar and A. Nusrath, "Tsunami numerical modeling and mitigation," *Frattura ed Integrità Strutturale*, vol. 4, no. 12, pp. 57–62, 2010.
- [4] A. Namdar, "Liquefaction zone and differential settlement of cohesionless soil subjected to dynamic loading," *European Journal of Government and Economics (EJGE)*, vol. 21, no. 2, pp. 593–605, 2016.
- [5] A. Namdar and G. S. Gopalakrishna, "Seismic mitigation of embankment by using dense zone in subsoil," *Emirates Journal for Engineering Research*, vol. 13, no. 3, pp. 55–61, 2008.
- [6] A. Namdar, "A numerical investigation on soil-concrete foundation interaction," *Procedia Structural Integrity*, vol. 2, pp. 2803–2809, 2016.
- [7] N. B. Muhammad, A. Namdar, and I. B. Zakaria, "Liquefaction mechanisms and mitigation-A review," *Research Journal of Applied Sciences, Engineering and Technology*, vol. 5, no. 2, pp. 574–578, 2013.
- [8] S. N. Moghaddas Tafreshi, N. Joz Darabi, and A. Dawson, "Cyclic loading response of footing on multi-layered rubber-soil mixtures," *Geomechanics and Engineering*, vol. 14, no. 2, pp. 115–129, 2018.
- [9] Z. Karabash and A. F. Cabalar, "Effect of tire crumb and cement addition on triaxial shear behavior of sandy soils," *Geomechanics and Engineering*, vol. 8, no. 1, pp. 1–15, 2015.
- [10] Y. Miyamoto, Y. Ohtsuka, A. Fukuoka, T. Nasuda, and M. Izumi, "Experimental studies on an embedded structure-soil interaction," in *Proceedings of International Conferences on Recent Advances in Geotechnical Earthquake Engineering and Soil Dynamics*, vol. 19, Rolla, MO, USA, March 1991.
- [11] A. Armin, R. Fotouhi, and W. Szyszkowski, "On the FE modeling of soil-blade interaction in tillage operations," *Finite Elements in Analysis and Design*, vol. 92, pp. 1–11, 2014.
- [12] J. Li, C. Wu, and H. Hao, "An experimental and numerical study of reinforced ultra-high performance concrete slabs under blast loads," *Materials and Design*, vol. 82, pp. 64–76, 2015.
- [13] <https://strongmotioncenter.org/>.
- [14] A. Namdar, Y. Dong, and Y. Liu, "Timber beam seismic design—a numerical simulation," *Frattura ed Integrità Strutturale*, vol. 47, pp. 451–458, 2019.
- [15] O. F. El Hadi Drbe and M. H. El Naggar, "Axial monotonic and cyclic compression behaviour of hollow-bar micropiles," *Canadian Geotechnical Journal*, vol. 52, no. 4, pp. 426–441, 2014.
- [16] A. V. Rose, R. N. Taylor, and M. H. El Naggar, "Numerical modelling of perimeter pile groups in clay," *Canadian Geotechnical Journal*, vol. 50, no. 3, pp. 250–258, 2013.
- [17] A. Y. Abd Elaziz and M. H. El Naggar, "Geotechnical capacity of hollow-bar micropiles in cohesive soils," *Canadian Geotechnical Journal*, vol. 51, no. 10, pp. 1123–1138, 2014.
- [18] A. M. Alnuaim, M. H. El Naggar, and H. El Naggar, "Numerical investigation of the performance of micropiled rafts in sand," *Computers and Geotechnics*, vol. 77, pp. 91–105, 2016.
- [19] A. De Santis, O. Di Bartolomeo, D. Iacoviello, and F. Iacoviello, "Quantitative shape evaluation of graphite particles in ductile iron," *Journal of Materials Processing Technology*, vol. 196, no. 1–3, pp. 292–302, 2008.
- [20] F. Iacoviello, V. Di Cocco, M. Cavallini, T. Marcu, and A. Molinari, "Influence of sintered stainless steel microstructure on fatigue crack paths," *Fatigue Fracture of Engineering Materials and Structures*, vol. 28, no. 1–2, pp. 187–193, 2005.
- [21] M. Cavallini, O. Di Bartolomeo, and F. Iacoviello, "Fatigue crack propagation damaging micromechanisms in ductile cast irons," *Engineering Fracture Mechanics*, vol. 75, no. 3–4, pp. 694–704, 2008.
- [22] J. Kumar and P. Ghosh, "Seismic bearing capacity for embedded footings on sloping ground," *Géotechnique*, vol. 56, no. 2, pp. 133–140, 2006.
- [23] J. Kumar and V. B. K. M. Rao, "Seismic bearing capacity factors for spread foundations," *Géotechnique*, vol. 52, no. 2, pp. 79–88, 2002.
- [24] D. Chakraborty and J. Kumar, "Seismic bearing capacity of shallow embedded foundations on sloping ground surface," *International Journal of Geomechanics*, vol. 15, no. 1, article 04014035, 2015.
- [25] L. Y. Peng, Y. J. Kang, Z. Y. Tang, and H. T. Chen, "Seismic performance of CAP1400 nuclear power station considering foundation uplift," *Shock and Vibration*, vol. 2018, Article ID 8761209, 16 pages, 2018.
- [26] O. Abuhajar, H. El Naggar, and T. Newson, "Experimental and numerical investigations of the effect of buried box culverts on earthquake excitation," *Soil Dynamics and Earthquake Engineering*, vol. 79, pp. 130–148, 2015.
- [27] A. El Takch, A. Sadrekarimi, and H. El Naggar, "Cyclic resistance and liquefaction behavior of silt and sandy silt soils," *Soil Dynamics and Earthquake Engineering*, vol. 83, pp. 98–109, 2016.
- [28] K. Holak, P. Kohut, A. Martowicz, and T. Uhl, "An uncertainty analysis for developed measurement vision system aided by numerical simulations," *Mechanics and Control*, vol. 30, no. 2, pp. 65–72, 2011.

Research Article

Estimation of Cement Asphalt Mortar Disengagement Degree Using Vehicle Dynamic Response

Hui Shi ^{1,2}, Liqiang Zhu,^{1,2} Hongmei Shi ^{1,2} and Zujun Yu^{1,2}

¹School of Mechanical, Electronic and Control Engineering, Beijing Jiaotong University, Beijing 100044, China

²Key Laboratory of Vehicle Advanced Manufacturing, Measuring and Control Technology (Beijing Jiaotong University), Ministry of Education, Beijing 100044, China

Correspondence should be addressed to Hongmei Shi; hmshi@bjtu.edu.cn

Received 4 October 2018; Revised 6 December 2018; Accepted 19 December 2018; Published 3 January 2019

Guest Editor: Alessandro Sabato

Copyright © 2019 Hui Shi et al. This is an open access article distributed under the Creative Commons Attribution License, which permits unrestricted use, distribution, and reproduction in any medium, provided the original work is properly cited.

Cement asphalt mortar (CA) disengagement of a ballastless track will induce changes of dynamic response of a passing vehicle, which can accordingly be used to estimate the disengagement degree. In this paper, a novel method called CA mortar disengagement degree estimation algorithm (CMDEA) is proposed through an analysis of wheel acceleration of a passing vehicle. The disengagement degree estimation is transformed into an optimization problem by regarding the CA mortar disengagement degree as a parameter of a vehicle-track coupling model. An improved genetic algorithm with a shifting window is employed for the parameter optimization, which is split into a number of phases and whose initial values are given in terms of a priori probabilities. The accuracy and robustness of the estimation are discussed, and the results are compared with regular genetic algorithm. The simulation results show that CMDEA can estimate CA mortar degrees with an acceptable accuracy. Meanwhile, the proposed algorithm has the advantages of a lower error value and much shorter computation time. Moreover, the robustness of the algorithm under different vehicle speeds, track irregularities, and signal noise levels is also verified.

1. Introduction

With the commissioning of the Beijing-Tianjin intercity railway in 2008, the running mileage of China's high-speed railways has exceeded 20,000 kilometers. As high-speed railways are being rapidly developed, ballastless track has been widely adopted in many countries due to its advantages of good stability, good durability, and less maintenance [1]. The understructure of the China Railway Track System II-type (CRTSII) slab ballastless track consists of track slabs, a cement-emulsified asphalt (CA) mortar layer, a support layer, and an embankment. As the speed of vehicles increases greatly, the dynamic effects between wheels and rails also increase, resulting in the strengthening of the dynamic effect on infrastructure. As CA mortar is a key component of the elastic adjustment layer in ballastless track, its performance directly affects the service durability of slab ballastless track

equipment. Due to the difficulty of construction quality control and the warping effect of track slabs, CA mortar will often deteriorate to varying degrees. When the entire CA mortar layer is separated from the interface of the track slab, it will give rise to a complete loss of cohesion, a phenomenon known as CA mortar disengagement. If it is not repaired in time, it will accelerate the structural damage of track and even have adverse effects on traffic safety. Therefore, CA mortar disengagement detection is necessary to ensure the safety of vehicle operations and formulate a timely rail line maintenance plan.

Presently, extensive research on nondestructive testing has been carried out in the field of concrete defect detection. Nevertheless, the references on CA mortar disengagement identification are countable, most of which is focused on the impulse hammer excitation method. Chen [2] evaluated the effectiveness of elastic wave detection in the underline

layered structure based on elastic wave propagation theory in layered media and the time frequency characteristics of elastic wave fields. Hu [3] researched the propagation velocity and laws of stress waves in track slabs and estimated the depth of honeycombing using the impact-echo method. Zhong et al. [4] proposed a detection method based on a detector array group for elastic wave propagation in multilayer media, which can effectively detect the spatial distribution of segregations among CA mortar layers. Tian et al. [5] discussed the feasibility of mortar defect detection using the transient elastic wave method. The results showed that the defects of CA mortar can be detected using the characteristics of frequency band peaks and the power density values of elastic waves. Li et al. [6] applied gradient boosted regression trees (GBRT) to CA mortar disengagement detection using a sound signal produced by a passing train to detect the damage qualitatively. The aforementioned methods based on the impulse hammer can only be carried out in the period of skylight time with the shortcomings of low efficiency and limited identification area.

Service condition monitoring of railway infrastructures using passing vehicles has been a new research area since 2000 and shows promising results in structural health monitoring [7]. Its main premise is that differences in the physical properties of track structure such as mass, stiffness, and damping will give rise to changes in vibration characteristics. A direct detection method is to install sensors on the track and detect damages by analysing the vibration responses of the track. This requires a large number of sensors to be laid along the track. An alternative, more cost-efficient detection method is to mount sensors on vehicles and detect track damages utilizing the dynamic responses of the vehicles. The last two decades have seen a rise in studies attempting to detect bridge damage using indirect vibration-based methods. Yang et al. [8, 9] firstly proposed the theory of extracting the first-order natural frequency of bridges from vehicle response and then carried validation tests. Zhang et al. [10] described a new method based on operating deflection shape curvature extracted from the dynamic response of a passing vehicle, which can be used to detect local damages in beam and plate-like structures. Molodova et al. [11] employed a model to determine a quantitative relationship between the characteristics of the axle box accelerations and short track defects. On-board methods using vehicle dynamic responses have the potential to be used as a monitoring tool to estimate track infrastructure conditions. Nonetheless, most of these indirect methods utilize low-speed vehicles and involve disturbing normal rail traffic.

In recent years, more and more researchers have introduced intelligent sensing algorithms into vehicle-based indirect methods. Li and Au [12] suggested a multistage damage detection method based on modal strain energy and a genetic algorithm to determine the location of damage in a two-span continuous bridge. Quirke et al. [13] proposed a method to estimate railway track stiffness using a cross-entropy optimization technique. Li et al. [14] employed a method based on the generalized pattern search

algorithm to identify bridge parameters indirectly using a passing vehicle.

Typical intelligent optimization algorithms include simulated annealing (SA), the gradient descent method, genetic algorithm (GA), etc. Although simulated annealing and gradient descent method achieve fast convergence in local optimizations, they can easily fall into local minima, resulting in a weak global search ability, low optimization performance, and slow or even no global convergence. Moreover, the gradient descent method involves computing the derivatives, which can be hard for large nonlinear problems. Genetic algorithm, first proposed by John Holland in 1975, achieves the adaptability of individuals through the mechanics of natural selection, crossover, and mutation by means of biogenetics and simulates the evolution process of nature. It is a nonderivative-optimized stochastic optimization search algorithm with strong global search ability and robustness. As an adaptive global probability search algorithm, GA is very suitable for solving complex nonlinear optimization problems. Therefore, it is widely used in global optimization [15, 16], search [17], and machine learning [18] contexts. In order to overcome the shortcoming of long running time of regular genetic algorithm, an improved genetic algorithm is employed in this paper, which is split into a number of phases and whose initial values are given in terms of a priori probabilities.

At present, the research on the estimation of CA mortar disengagement degree based on dynamic responses of passing vehicles is still a blank field. A novel method is proposed in this paper for the estimation of CA mortar disengagement degree through an analysis of vehicle wheel accelerations. The method is referred to throughout the paper as the CA mortar disengagement degree estimation algorithm (CMDEA). The vehicle-track coupling model with the CA mortar disengagement model used in this paper and the simulation result of dynamic response are described in Section 2. The CA mortar disengagement degree estimation algorithm is introduced in Section 3. Numerical simulation results are demonstrated and analysed in Section 4, and the robustness of the proposed algorithm under different conditions is validated in Section 5.

2. Model Description

2.1. Vehicle Model. As shown in Figure 1(a), the vehicle is modelled as a multirigid system that moves on a track structure at the speed of v and consists of three masses: m_c representing the car body mass, m_t representing the bogie mass, and m_w representing the wheel mass [19]. In consideration of the vertical translation and nodding motion of the car body and the bogies, and the vertical translation of the wheels, the vehicle system has 10 degrees of freedom (DOFs). The components are connected by elastic springs and dampers, representing the secondary and primary suspension of the vehicle, respectively.

The general form of the equation of motion for the vehicle system can be represented as follows:

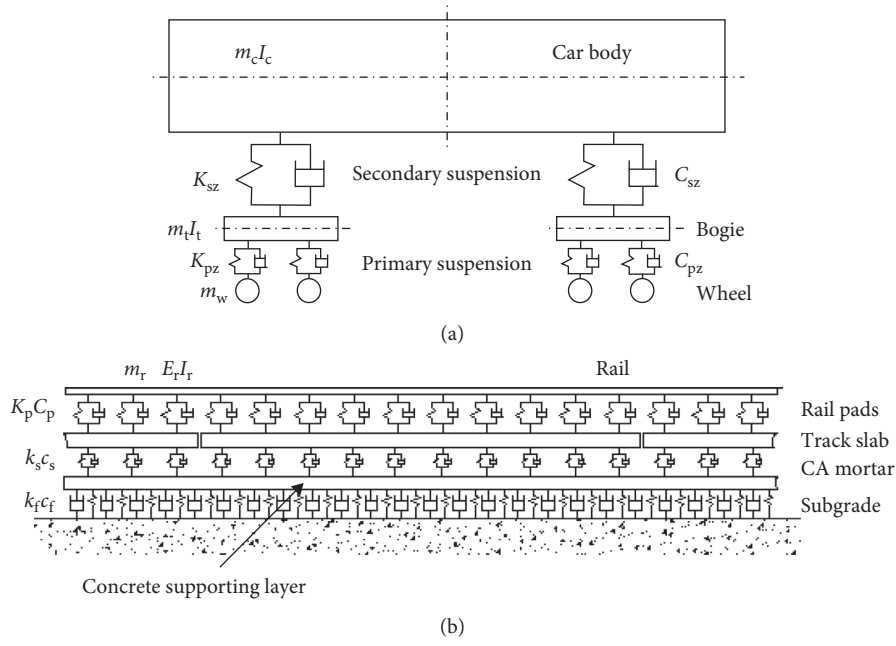


FIGURE 1: Vehicle and track model: (a) vehicle model; (b) ballastless slab track model.

$$\mathbf{M}_v \ddot{\mathbf{x}}_v + \mathbf{C}_v \dot{\mathbf{x}}_v + \mathbf{K}_v \mathbf{x}_v = \mathbf{p}_v, \quad (1)$$

where \mathbf{M}_v , \mathbf{C}_v , and \mathbf{K}_v are the mass, damping, and stiffness matrices of the vehicle; the vectors \mathbf{x}_v , $\dot{\mathbf{x}}_v$, and $\ddot{\mathbf{x}}_v$ are the vehicle displacements, velocities, and accelerations, respectively; and \mathbf{p}_v is the force vector of the vehicle system.

2.2. Track Model. As shown in Figure 1(b), the track system is modelled here as a beam continuously supported on a triple-layer spring-damper system, which represents the rail pads, CA mortars, and subgrade, respectively.

The general form of the equation of motion for the track system can be represented as follows:

$$\mathbf{M}_t \ddot{\mathbf{x}}_t + \mathbf{C}_t \dot{\mathbf{x}}_t + \mathbf{K}_t \mathbf{x}_t = \mathbf{p}_t, \quad (2)$$

where \mathbf{M}_t , \mathbf{C}_t , and \mathbf{K}_t are the global mass, damping, and stiffness matrices of the track system; the vectors \mathbf{x}_t , $\dot{\mathbf{x}}_t$, and $\ddot{\mathbf{x}}_t$ are the track system displacements, velocities, and accelerations, respectively; and \mathbf{p}_t is the force vector of the track system.

The China Railways High-speed 2 (CRH2) electric multiple unit (EMU) trailer and the high-speed line with China Railway Track System II-type (CRTS II) track slab are considered in this paper. The corresponding property values were gathered from the literature [19] and are listed in Tables 1 and 2.

2.3. Coupling Model. To determine the wheel-rail vertical force, we applied Hertz nonlinear elastic contact theory for the vehicle-track vertical coupling relationship. When the wheel tread is wear type, the expression of the wheel-rail vertical force is

TABLE 1: Properties for CRH2 EMU trailer.

Property	Unit	Symbol	Value
Mass of car body	kg	m_c	26100
Mass of bogie	kg	m_t	2600
Mass of wheel	kg	m_w	2100
Pitch moment of inertia of car	kg·m ²	I_c	1.28×10^6
Pitch moment of inertia of bogie	kg·m ²	I_t	1424
Stiffness of primary suspension	N/m	K_{pz}	1.176×10^6
Stiffness of secondary suspension	N/m	C_{pz}	9.91×10^5
Damping of primary suspension	N·s/m	K_{sz}	1.02×10^6
Damping of secondary suspension	N·s/m	C_{sz}	1.96×10^5
Half of rigid wheelbase	m	l_t	1.25
Half of length between the bogie pivot centers	m	l_c	8.75
Radius of wheel	m	R	0.43

TABLE 2: Properties for high-speed line.

Property	Unit	Symbol	Value
Elastic modulus of rail	N/m ²	E_r	2.059×10^{11}
Rotational inertia of rail	m ⁴	I_r	3.217×10^{-5}
Mass of rail per unit length	kg/m	m_r	60.64
Stiffness of rail pad	N/m	K_p	6×10^7
Damping of rail pad	N·s/m	C_p	7.5×10^4
Length between fasteners	m	L_p	0.65
Length of track slab	m	L_s	6.5 m
Mass of track slab	kg	m_s	8.3×10^3
Elastic modulus of track slab	MPa	E_s	3.9×10^4
Rotational inertia of track slab	m ⁴	I_s	3.32×10^7
Stiffness of CA mortar	N/m ²	k_s	1.25×10^9
Damping of CA mortar	N·s/m ²	c_s	3.458×10^4

$$p_j(t) = \begin{cases} \left\{ \frac{1}{G} [x_{wj}(t) - x_r(x_{wj}, t) - x_0(t)] \right\}^{3/2}, & (x_{wj}(t) - x_r(x_{wj}, t) - x_0(t) > 0), \\ 0, & (x_{wj}(t) - x_r(x_{wj}, t) - x_0(t) < 0), \end{cases} \quad (3)$$

where $j = 1 \sim 4$; $x_{wj}(t)$ and $x_r(x_{wj}, t)$ represent the vertical displacement of the j th wheel and the rail at the j th wheel-rail contact position at time t , respectively; $x_0(t)$ represents

the track irregularity at the wheel-rail interface; and G is the Hertzian contact coefficient.

The expression of the force vector of the vehicle system is

$$\mathbf{p}_v = \{m_c g \ 0 \ m_t g \ 0 \ m_t g \ 0 \ m_w g - 2p_1(t) \ m_w g - 2p_2(t) \ m_w g - 2p_3(t) \ m_w g - 2p_4(t)\}^T. \quad (4)$$

The expression of the force vector of the track system is

$$\mathbf{p}_t = \left[\sum_{j=1}^4 p_j(t) Y_k(x_{wj}), \mathbf{0}_{1 \times (m \times \text{NMS})}, \mathbf{0}_{1 \times \text{NMSS}} \right]^T, \quad (k = 1 \sim \text{NM}), \quad (5)$$

where NM, NMS, and NMSS are the modal orders of the rail, track slab, and concrete supporting layer, respectively, and m is the number of track slabs in the model. Y_k is the modal shape function of rail, the expression of which can be written as follows:

$$Y_k(x) = \sqrt{\frac{2}{m_t L}} \sin \frac{k\pi x}{L}. \quad (6)$$

2.4. Track Irregularity. Considering the influence of track irregularity on the vibration of the coupling model, a time domain random irregularity sample is generated using the China ballastless track power spectral density (PSD) function $S(f)$ proposed by the China Academy of Railway Sciences. The fitting equation is as follows:

$$S(f) = m f^{-k}, \quad (7)$$

where the unit of $S(f)$ is $\text{mm}^2/(1/\text{m})$; f is the spatial frequency (1/m); m and k are fitting coefficients. The time domain random irregularity sample of the China ballastless track spectrum is calculated using the inverse fast Fourier transform (IFFT) method.

2.5. CA Mortar Disengagement Model. The condition of CA mortar disengagement can be simulated as a loss in stiffness by changing the coefficients of the elastic spring and damper that represent CA mortar in the corresponding areas [20]. In order to simulate the disengagement, a discrete CA mortar model is established, in which a CA mortar is divided into many units of longitudinal length l_s [21].

The CA mortar disengagement model is shown in Figure 2. The direction along the rail is the longitudinal direction, while the direction which is vertical to the rail is the lateral direction. The CA mortar disengagement condition can be measured by two parameters, one of which is the CA mortar longitudinal disengagement length l and the

other is the lateral disengagement degree of the i th CA mortar unit d_i .

As illustrated in Figure 2, d_i can be expressed as

$$d_i = 1 - \frac{b_i}{b_0}, \quad (8)$$

where b_0 is the overall track slab width (2.55 m for CRTS II track slab), and b_i is the width of the i th CA mortar unit where no disengagement has occurred. Hence, $d_i = 1$ indicates that the i th CA mortar unit is completely disengaged in the lateral direction, whereas $d_i = 0.7$ implies that 70% of the i th CA mortar unit in the lateral direction is disengaged. Then the supporting force of the i th CA mortar unit on the track slab can be expressed as

$$F_{sri} = d_i \cdot k_s \cdot (x_r - x_s) + d_i \cdot c_s \cdot (\dot{x}_r - \dot{x}_s), \quad (9)$$

where x_r and x_s are the displacement of the rail and the track slab, respectively.

When the CA mortar disengagement longitudinal length is less than 0.65 m, the effect of disengagement on the wheel acceleration is not obvious [22, 23]. Consequently, 0.65 m will be considered as longitudinal length of one unit in this model, i.e., $l_s = 0.65$ m. Therefore, the CA mortar longitudinal disengagement length l can be evaluated by unit, while the lateral disengagement degree d of each unit is the value we want to estimate and is the focus in this paper.

The schematic diagram of the overall model used in this paper is shown in Figure 3. The simulated length in this paper is 16 track plates, i.e., 104 m. The position of the track slab is represented by No. 1~No. 16. For the CRTS II ballastless track considered in this paper, there are 10 CA mortar units corresponding to a piece of track slab. Considering the length of track occupied by the vehicle (20 m for CRH2 EMU) and the boundary effect of wheel acceleration signal, the CA mortar disengagement condition of the first 5 and the last piece's track slab (No. 1~No. 5, No. 16) is assumed to be known. In this paper, we aim at estimating the disengagement degree parameters of the subsequent 10 pieces track slabs (No. 6~No. 15), regardless of the boundary effect, which corresponds to 100 units ($D = [d_1, d_2, \dots, d_{100}]$). The subscript number i ($i = 1 \sim 100$) represents the order number of each CA mortar unit.

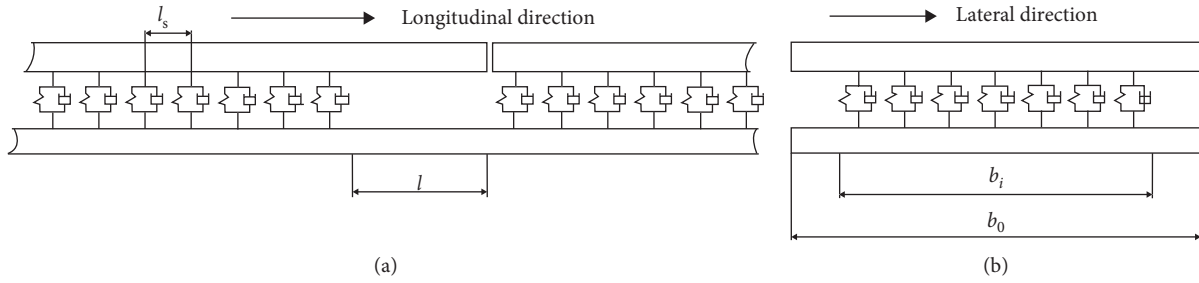


FIGURE 2: CA mortar disengagement model: (a) longitudinal view; (b) lateral view.

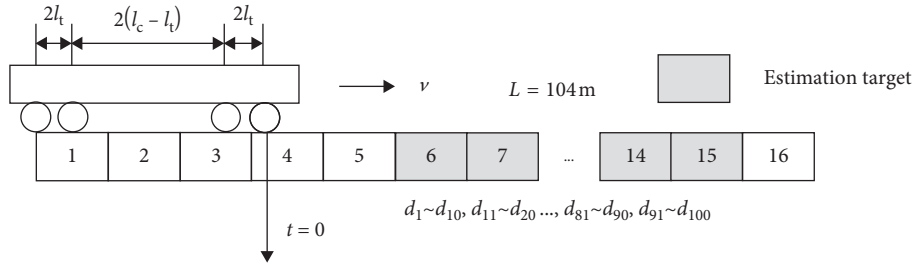


FIGURE 3: Schematic diagram of the overall model.

2.6. Simulation Results. To assess the concept of CMDEA in this paper, numerical simulations for the vehicle-track coupling model are used. A hypothetical CA mortar disengagement condition was used to demonstrate the capabilities of CMDEA. The values of the hypothetical condition of CA mortar disengagement referred to here as the “actual” values are as follows:

$$\begin{aligned} d_{11} &= 0.2, \\ d_{31} &= 0.4, \\ d_{51} &= 0.6, \\ d_{71} &= 0.8, \\ d_{91} &= 1, \end{aligned} \quad (10)$$

with the disengagement degrees of other units set to 0.

The equations of the coupling model are solved using the multistep prediction-correction based on Newmark’s method, as developed by Zhai for Matlab [19]. A vehicle travels over a track at a constant speed of 300 km/h. The scanning frequency used for all simulations is 10 kHz. The simulated acceleration signal of the front wheel when a vehicle crosses a track model including the hypothetical CA mortar disengagement condition is taken as the “measured” signal, shown in Figure 4. Then, the simulated response (“measured” signal) is input into CMDEA, which was used to estimate the CA disengagement degrees.

3. CA Mortar Disengagement Degree Estimation Algorithm (CMDEA)

A CA mortar disengagement degree estimation algorithm is described in this section based on an adapted genetic optimization algorithm. The disengagement degree estimation is transformed into an optimization problem by regarding

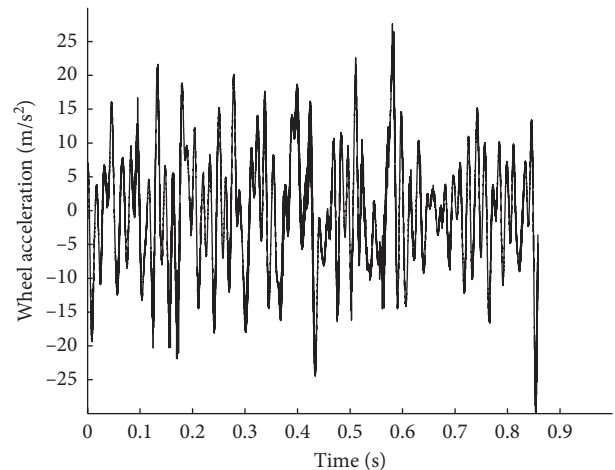


FIGURE 4: Simulated signal of wheel acceleration.

the disengagement degree as a parameter of the vehicle-track coupling model.

3.1. CA Mortar Disengagement Degree Estimation Principle Using Genetic Algorithm. A genetic algorithm is applied in this paper to estimate CA mortar disengagement degrees from the dynamic responses of a passing vehicle as it crosses a track. Considering the CA mortar disengagement degrees as individuals, the parameters are transformed into a one-dimensional data string. The fitness of the individuals in each generation gradually increases utilizing the genetic operations and finally converges to a group of individuals that minimizes the objective function.

Firstly, a population of CA mortar disengagement degree vectors is generated randomly in the range of $[0, 1]$. For each seed in the population, a CA mortar disengagement degree

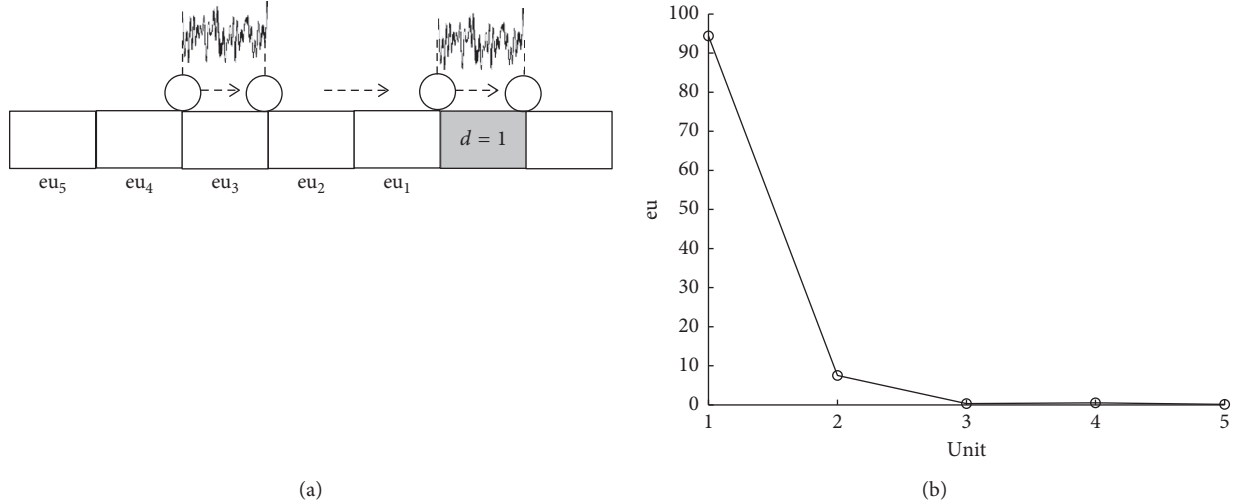


FIGURE 5: Boundary effects analysis: (a) diagram of effect index; (b) effect index ($l = 0.65$ m and $d = 1$).

matrix is produced, and the simulated acceleration signal of the wheel is calculated using the vehicle-track coupling model. An objective function value is then calculated to assess the quality of each seed.

In this paper, the objective function is taken as the sum of squared differences between the wheel accelerations calculated for each trial CA mortar disengagement degree matrix, \tilde{A} , and the simulated wheel accelerations for the on-board measurement system, A' . The equation of the objective function is

$$O = \Delta E^2 = \sum_{i=1}^n (\tilde{A} - A')^2, \quad (11)$$

where n is the total number of scans in the acceleration signal.

3.2. Basis for the Structure of CMDEA. The disengagement of a CA mortar unit not only has an effect on the response of a vehicle when it passes the unit, but also has an effect when the vehicle passes the preceding units, as shown in Figure 5(a). In order to remove the boundary effects, it is necessary to include a number of units at the beginning of the estimation process. To quantify the effect of the disengagement unit on the wheel acceleration when a vehicle passes the preceding units, the effect index eu_i is defined as follows:

$$eu_i = \sum_{j=1}^n (A_j - A_{0j})^2, \quad (12)$$

where n is the number of sampling points in each unit; A_{0i} and A_i represent the wheel acceleration over healthy and damaged CA mortar, respectively; and the subscript number i ($i = 1, 2, 3, \dots$) represents the order number of the preceding unit.

Figure 5(b) shows the effect index of a CA mortar disengagement unit ($l = 0.65$ m and $d = 1$) on wheel acceleration when a vehicle passes the 5 preceding units. It can be

seen that the effect index of the 1st unit is large, but diminishes as the distance from the disengagement unit becomes longer. The effect index of the 3rd unit is very small and can be ignored. Therefore, the effects of 2 preceding units need to be considered for the estimation process for each unit.

3.3. Improved Genetic Algorithm with a Shifting Window. The CA mortar disengagement degree varies along the track, which means the representing parameter d_i is different and multiple parameters need to be estimated. Considering the possibility of determining limit parameters for one optimization process, an adapted version of the genetic algorithm with a shifting window is used. The total estimation process is split into a number of phases, in which a smaller number of CA mortar disengagement degrees are estimated before proceeding to the next phase. Stepping through the CA mortar disengagement degrees in phases significantly reduces the dimensionality of the problem.

Due to the effects of varied CA mortar disengagement degrees on the dynamic response of a vehicle when it passes the 2 preceding units of a disengagement unit, a length of 4 units is used in CMDEA as a phase length. CA mortar disengagement degrees at each phase are estimated for the last 2 units of the phase. CMDEA steps through the CA mortar disengagement degrees in phases using the disengagement degree estimation template, as shown in Figure 6(a). Green represents known parameters; gray represents unknown parameters which will be estimated during the current phase; white represents unknown parameters which are set to 0. The CA mortar disengagement degree values for the first 2 units are obtained from the previous phase, whereas for the last 2 units, they are estimated in the current phase and are used as known values for the first 2 units in the next phase. In order to ensure the vehicle dynamic equilibrium at the start of each phase, initial values for the dynamic response vectors (displacement, velocity, and acceleration) of the coupling model in the

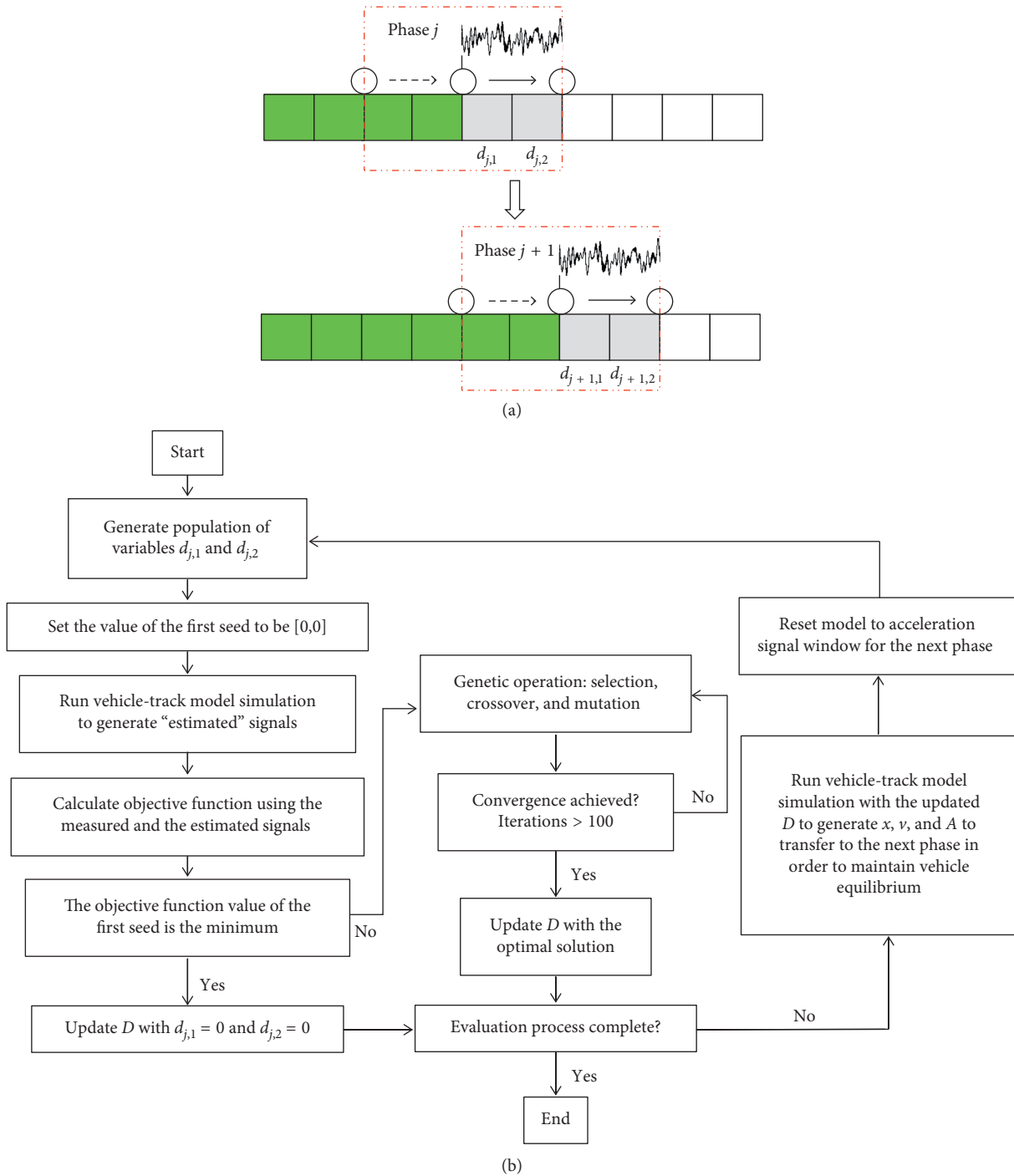


FIGURE 6: Improved genetic algorithm with a shifting window: (a) stepping procedure; (b) flowchart of CMDEA: Phase j .

current phase are transferred from the previous phase using the values estimated for the CA mortar disengagement degrees.

In view of the a priori probability that the CA mortar is healthy in most cases, i.e., $d_i = 0$, an improved genetic algorithm optimization process is employed in each phase. When the initial population is generated, the value of the first seed is initialized to $[0, 0]$. The sum of squares of the differences between the measured and the estimated signals

is calculated. If the objective function value of the first seed is the minimum, the value of $[0, 0]$ is then taken as the optimal solution in the current phase. Otherwise, the objective function values for all seeds in the population are ranked and genetic operations are carried out to improve the population of solutions in the next generation until convergence is achieved.

The process for estimating the CA mortar disengagement degrees in Phase j is shown in Figure 6(b).

4. Results and Discussion

The results of the numerical test of CMDEA for estimating the CA mortar disengagement are presented in this section. Parameters used in the CMDEA are listed in Table 3.

The objective function values of the optimal solution for the five damaged units at each iteration are illustrated in Figure 7(a). It is observed that the optimal solution of the function converges continuously during the evolution of the genetic algorithm, and the values of the objective function become smaller and smaller. It can be seen from the evolution process that at the beginning of the optimization, the seed optimization is rapid, and after 80 generations, the objective function value tends to stabilize. Therefore, 100 is taken as the upper limit of the number of iterations here.

The CA mortar disengagement degree estimation result is shown in Figure 7(b). The black circles represent the accrual values, whereas the red stars represent the estimated ones.

It can be seen from Figure 7(b) that the estimated values are almost consistent with the actual ones. In order to qualify the overall error between the actual and estimated values for CA mortar disengagement degrees, the margin of error E is defined as

$$E = \frac{\sqrt{\sum_{i=1}^N (d_i - \tilde{d}_i)^2}}{N}, \quad (13)$$

where i represents the order number of the unit, N represents the number of units to be estimated, and d_i and \tilde{d}_i represent the actual and the estimated value of the i th unit, respectively.

Table 4 shows comparisons of error values and total computation time required for CMDEA using the regular genetic algorithm and the improved genetic algorithm, respectively. The simulations were performed using a 4 GHz processor and 16.0 GB of RAM running on Matlab.

Since the improved genetic algorithm simplifies the optimization processes for most healthy units and reduces the cumulative error, it has the advantages of a lower error value and much shorter total computation time compared with the regular genetic algorithm, as illustrated in Table 4. Therefore, the CMDEA used in this paper is effective for estimating CA mortar disengagement degrees with an acceptable accuracy.

5. CMDEA under Different Conditions

When vehicle speeds, track irregularities, and signal noise levels are different, the dynamic responses of the vehicle-track coupling system are also different. In order to verify the robustness of CMDEA, its performance under different conditions will be discussed in this section.

5.1. Influence of Vehicle Speeds. The dynamic response of a vehicle will change as the vehicle's speed changes. The wheel accelerations resulting from the vehicle-track model for speeds of 250 km/h and 360 km/h are investigated in this

TABLE 3: CMDEA parameters.

Property	Value
Population size	10
Maximum of iterations	100
Crossover probability	0.7
Mutation probability	0.25

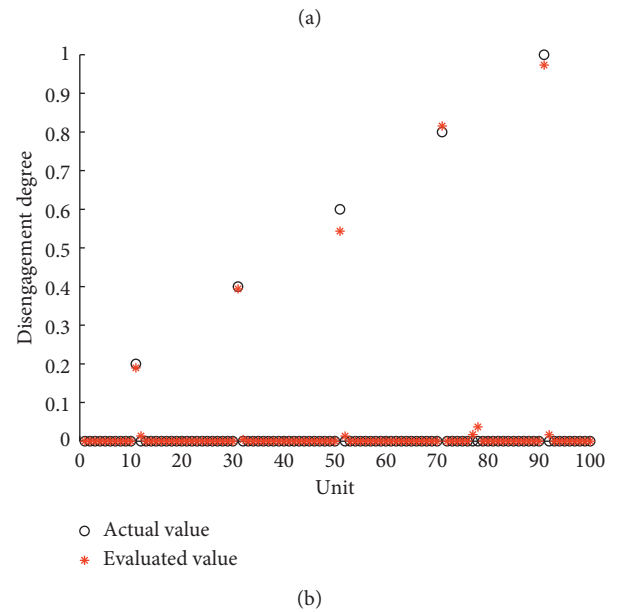
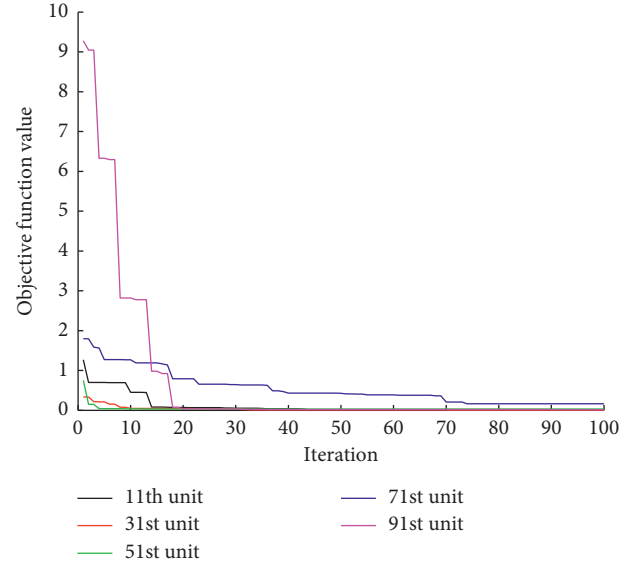


FIGURE 7: Simulation results: (a) objective function values for the optimal solutions at each iteration; (b) result of CA mortar disengagement degree estimation.

TABLE 4: Comparisons of error and computation time.

Algorithm	E	Computation time
Regular genetic algorithm	0.0021	150 h
Improved genetic algorithm	$8.1020e-04$	15 h

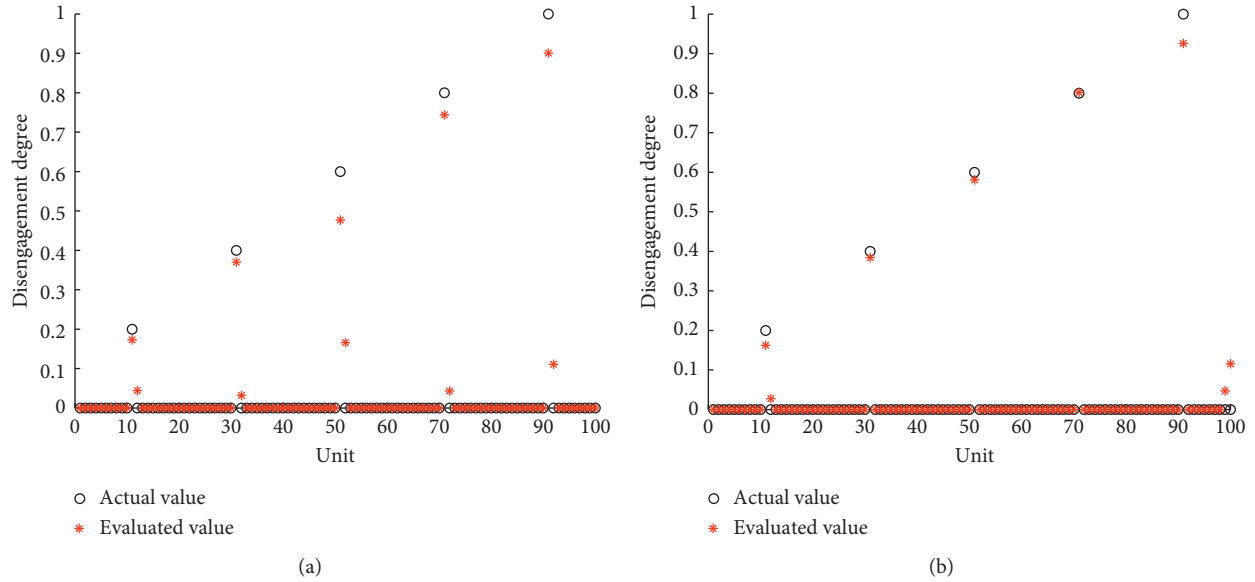


FIGURE 8: Estimation results of CMDEA under different vehicle speeds: (a) 250 km/h; (b) 360 km/h.

section. The other simulation parameters are the same as the above simulation. The estimation results under different vehicle speeds are shown in Figure 8.

According to equation (13), for vehicle speeds of 250 km/h and 360 km/h, the corresponding values of E are 0.0027 and 0.0015, respectively. Vehicle speeds have small influence on the prediction accuracy, and CA mortar disengagement degrees can be estimated well at both speeds. Therefore, the CMDEA shows good estimation robustness for various vehicle speeds.

5.2. Influence of Track Irregularities. In order to verify CMDEA under different track irregularities, the German low-disturbance spectrum was adopted and input into the algorithm, with the corresponding results shown in Figure 9.

It can be seen from Figure 9 that under the condition, the CA mortar disengagement degrees can also be estimated well except for limited incorrect estimates. The error E is 0.0048.

Track irregularities with larger amplitude have a great effect on the dynamic response than CA mortar disengagement, resulting in relatively large error values. Due to the larger amplitude of the German low-disturbance spectrum in the time domain compared with the China ballastless track spectrum, the estimation accuracy will be lower.

5.3. Influence of Noise. When assessing the effectiveness of CMDEA, its robustness with respect to measurement noise should be considered. To verify the tolerance to noise, the simulations were carried out by adding increasing Gaussian signal noise levels of 1%, 3%, 5%, and 10% (SNR 40 dB, 30.5 dB, 26 dB, and 20 dB) to the wheel acceleration signal before initiating CMDEA. The estimated and actual values of CA mortar disengagement degrees for this range of added signal noise levels are shown in Figure 10.

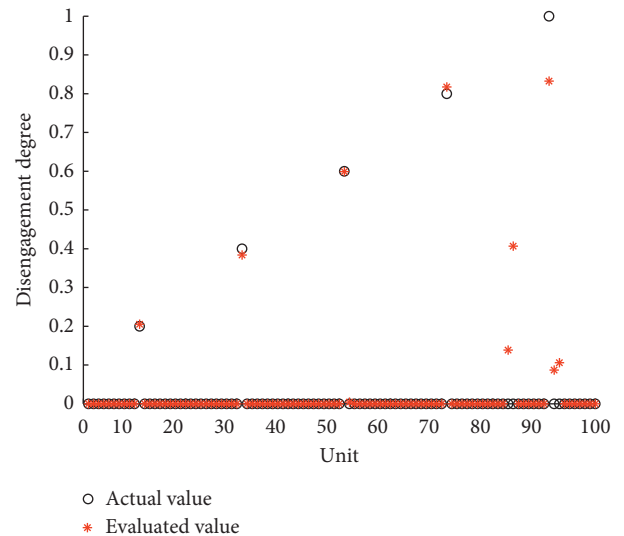


FIGURE 9: Estimation result of CMDEA with German low-disturbance spectrum.

It can be seen from Figure 10 that CA mortar disengagement degrees can be estimated under a lower level noise and even with a measurement signal noise of 10%. The estimation error is $9.9154e-04$, 0.0012, 0.0015, and 0.0025. An increase in the level of signal noise results in an increase in the error of the estimated CA mortar disengagement degrees.

6. Conclusions

CA mortar disengagement of a ballastless track will induce changes of the dynamic response of a passing vehicle, which can accordingly be used to estimate the disengagement degree. In this paper, a novel method for estimating CA mortar disengagement degrees was described through an

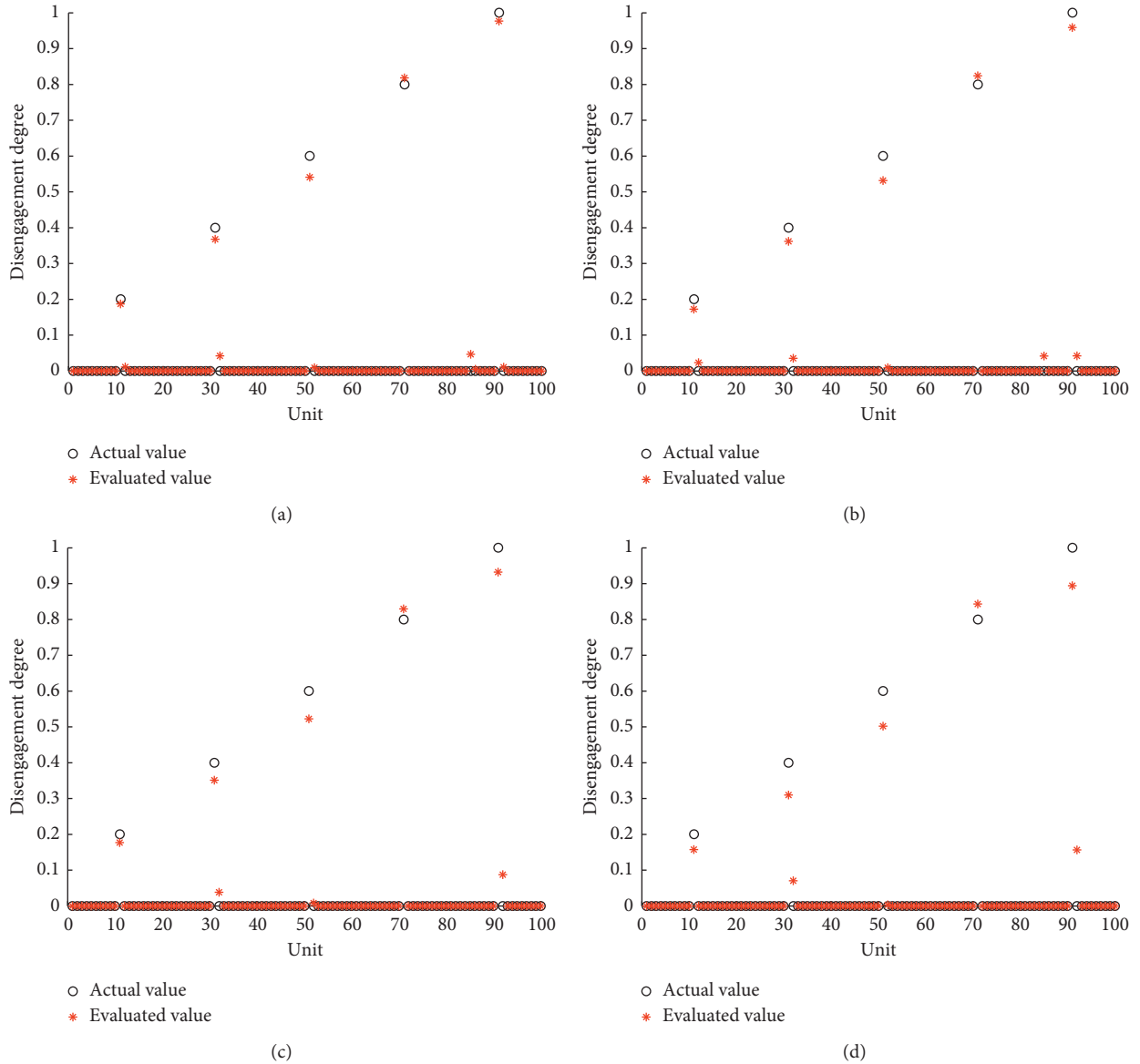


FIGURE 10: Estimation results of CMDEA under different noise levels: (a) 1% signal noise; (b) 3% signal noise; (c) 5% signal noise; (d) 10% signal noise.

analysis of wheel acceleration of a passing vehicle. The CMDEA employs an adapted genetic algorithm with a shifting window for parameter optimization, the process of which is split into a number of phases, and the initial value is given in terms of a prior probability. The CMDEA steps through the track in phases and obtains the overall disengagement degrees. The accuracy and robustness of the estimation were discussed.

From the simulation results presented in this paper, it is concluded that the CA mortar disengagement degrees estimated by the proposed algorithm are consistent with the hypothetical values assumed, and the robustness of the algorithm is validated under different track speeds, track irregularities, and signal noise levels. Compared with regular genetic algorithm, the improved algorithm has the advantages of a lower error value and much shorter total

computation time. The CMDEA method in this paper assumes a convergence limit of 100. The effect of this upper limit value has not been investigated in this paper. Increasing the value will improve the accuracy of the method, but at a cost in computation time.

The proposed algorithm uses a vehicle-track coupling model and takes the simulated responses as field measurements to estimate CA mortar disengagement degrees. The theoretical analysis and simulation experiments have been carried out to obtain corresponding results and provide a theoretical basis for the field detection of CA mortar disengagement in the future. In the actual application process, due to the difference between the actual vehicle parameters and theoretical parameters, the estimation value of the actual CA mortar disengagement degree and the simulation result may be different. Therefore, future

experiments for the CMDEA involving the installation of measurement sensors are necessary to validate and improve the accuracy of CMDEA. Improving the robustness of the CMDEA by combining the characteristics of different line structures, vehicle types, and operating conditions is also an important direction for future research.

Data Availability

All data generated or analysed during the study are included in this paper.

Conflicts of Interest

The authors declare that they have no conflicts of interest.

Acknowledgments

This work was supported by the National Key Research and Development Program of China under Grant no. 2016YFB1200401 and the Technology Research and Development Program of China Railway under Grant no. 2017G002-A.

References

- [1] Z. W. Lu, *Railway Track of Passenger Dedicated Line*, China Railway Publishing House, Beijing, China, 2005.
- [2] M. Chen, "study on elastic wave field detection method used in under line layered structure of high-speed railway," Master's thesis, Shanghai Jiaotong University, Shanghai, China, 2014.
- [3] Z. P. Hu, "Identify the depth of honeycomb in ballastless track concrete structure based on impact-echo method," *Railway Standard Design*, vol. 60, no. 10, pp. 22–26, 2016.
- [4] P. F. Zhong, A. L. Che, S. K. Feng et al., "Typical defects' analysis and nondestructive detection method for undertrack structures of high speed railways," *Journal of Vibration and Shock*, vol. 36, no. 11, pp. 154–160, 2017.
- [5] X. Tian, W. Zhao, Y. Du, and B. Wang, "Detection of mortar defects in ballastless tracks of high-speed railway using transient elastic wave method," *Journal of Civil Structural Health Monitoring*, vol. 8, no. 1, pp. 151–160, 2017.
- [6] Z. F. Li, W. B. Xie, and T. Liu, "A detection method of CA mortar disengagement based on GBRT algorithm," *Journal of Railway Science and Engineering*, vol. 15, no. 2, pp. 292–301, 2018.
- [7] A. Malekjafarian, P. J. McGetrick, and E. J. OBrien, "A review of indirect bridge monitoring using passing vehicles," *Shock and vibration*, vol. 2015, Article ID 286139, 16 pages, 2015.
- [8] Y. B. Yang, C. W. Lin, and J. D. Yau, "Extracting bridge frequencies from the dynamic response of a passing vehicle," *Journal of Sound and Vibration*, vol. 272, no. 3–5, pp. 471–493, 2004.
- [9] C. W. Lin and Y. B. Yang, "Use of a passing vehicle to scan the fundamental bridge frequencies: an experimental verification," *Engineering Structures*, vol. 27, no. 13, pp. 1865–1878, 2005.
- [10] Y. Zhang, L. Wang, and Z. Xiang, "Damage detection by mode shape squares extracted from a passing vehicle," *Journal of Sound and Vibration*, vol. 331, no. 2, pp. 291–307, 2012.
- [11] M. Molodova, Z. Li, and R. Dollevoet, "Axle box acceleration: measurement and simulation for detection of short track defects," *Wear*, vol. 271, no. 1–2, pp. 349–356, 2011.
- [12] Z. H. Li and F. T. K. Au, "Damage detection of a continuous bridge from response of a moving vehicle," *Shock and Vibration*, vol. 2014, Article ID 146802, 7 pages, 2014.
- [13] P. Quirke, D. Cantero, E. J. Obrien, and C. Bowe, "Drive-by detection of railway track stiffness variation using in-service vehicles," *Proceedings of the Institution of Mechanical Engineers Part F: Journal of Rail and Rapid Transit*, vol. 231, no. 4, pp. 498–514, 2017.
- [14] W. M. Li, Z. H. Jiang, T. L. Wang, and H. P. Zhu, "Optimization method based on generalized pattern search algorithm to identify bridge parameters indirectly by a passing vehicle," *Journal of Sound and Vibration*, vol. 333, no. 2, pp. 364–380, 2014.
- [15] J. Marzbanrad, P. Poozesh, and M. Damroodi, "Improving vehicle ride comfort using an active and semi-active controller in a half-car model," *Journal of Vibration and Control*, vol. 19, no. 9, pp. 1357–1377, 2012.
- [16] M. A. Wardeh and H. A. Toutanji, "Parameter estimation of an anisotropic damage model for concrete using genetic algorithms," *International Journal of Damage Mechanics*, vol. 26, no. 6, pp. 801–825, 2015.
- [17] S. Acikbas and M. T. Soylemez, "Coasting point optimisation for mass rail transit lines using artificial neural networks and genetic algorithms," *IET Electric Power Applications*, vol. 2, no. 3, pp. 172–182, 2008.
- [18] Y. He and J. Mcphee, "Design optimization of rail vehicles with passive and active suspensions: a combined approach using genetic algorithms and multibody dynamics," *Vehicle System Dynamics*, vol. 37, no. 1, pp. 397–408, 2002.
- [19] W. M. Zhai, *Vehicle-Track Coupling Dynamics*, Science Press, Beijing, China, 3rd edition, 2007.
- [20] P. G. Li, X. Y. Liu, and G. Q. Li, "Influence of CA mortar void on dynamic characteristics of unit slab track on bridge," *China Railway Science*, vol. 35, no. 3, pp. 20–27, 2014.
- [21] H. Shi, Z. J. Yu, and H. M. Shi, "An improved method for dynamic modelling of a slab track on a high-speed railway," in *Proceedings of the 15th International Conference on Railway Engineering Design and Operation*, pp. 225–237, WIT Press, Madrid, Spain, July 2016.
- [22] H. Shi, Z. J. Yu, H. M. Shi, and L. Zhu, "Recognition algorithm for the disengagement of cement asphalt mortar based on dynamic responses of vehicles," *Proceedings of the Institution of Mechanical Engineers, Part F: Journal of Rail and Rapid Transit*, article 0954409718794018, 2018.
- [23] P. Wang, H. Xu, and R. Chen, "Effect of cement asphalt mortar debonding on dynamic properties of CRTS II slab ballastless track," *Advances in Materials Science and Engineering*, vol. 2014, Article ID 193128, 8 pages, 2014.

Research Article

Visual Identity-Based Earthquake Ground Displacement Testing Method

Chen Su,¹ Zhao Sicheng,² Dai Zhijun ,¹ Li Xiaojun ,^{1,2} and Zhou Yue¹

¹*Institute of Geophysics, China Earthquake Administration, Beijing 100081, China*

²*College of Architecture and Civil Engineering, Beijing University of Technology, Beijing 100022, China*

Correspondence should be addressed to Dai Zhijun; dzj@cea-igp.ac.cn and Li Xiaojun; beerli@vip.sina.com

Received 19 July 2018; Revised 26 November 2018; Accepted 5 December 2018; Published 2 January 2019

Guest Editor: Krzysztof Holak

Copyright © 2019 Chen Su et al. This is an open access article distributed under the Creative Commons Attribution License, which permits unrestricted use, distribution, and reproduction in any medium, provided the original work is properly cited.

Ground deformation observation is widely concerned in the field of earthquake engineering. This paper proposes a high-precision displacement measurement technology based on both computer vision and numerical simulation. During the earthquake, the vision-based testing system collects visual data of the target installed on the location to be observed. The visual data streams can be quantified to the dynamic relative displacement value automatically, by employing mathematical vision algorithms and then by taking the relative displacement as an intermediate quantity, which is brought into the numerical model for iteration. When the test result is close to the simulated one, the absolute ground displacement data could be obtained approximately. A series of experiments have been carried out to suggest that the proposed method presents an innovative and low-cost solution to ground measurement in high accuracy. The method not only realizes the real-time ground deformation observation; moreover, it also provides a wider range of reliable data support to understand deformation mechanism, investigate seismic source information, and recognize the ground motion characteristics.

1. Introduction

Ground deformation in earthquake has always been the focus in the field of earthquake engineering. Persistent monitoring and quantification of ground deformation before and after earthquake not only can establish significant amount of data for the mitigation of seismic hazard but also provide valuable insights into the evolution of the surface deformation accumulation phase and the ground motion properties [1, 2]. In spite of ground displacement response is known as the critical metric for ground motion evaluation, direct measurement also face a big challenge, especially for the dynamic measurements during an earthquake.

Early geodetic measurement relied on the ground-based optical or mechanical techniques, of which triangulation, trilateration, and leveling were the most common. However, it is difficult to provide a precise measurement in the complex geological environment consistently due to the discrete point monitoring and accumulative error [3]. The need for high performance in the field of intelligent sensing

machines, data intelligent processing, real-time monitoring, and dynamic management have become the development direction of modern geodetic monitoring instruments.

However, the seismic observation networks make great contributions to the research of strong-seismic observation. The near-field main shock is still hard to be recorded completely owing to the sparse density of networks in pain areas [4]. In recent years, various space-geodetic techniques, especially the global positioning system (GPS) [1, 5] and interferometer synthetic aperture radar (INSAR) [6], have been extensively implemented to study the ground motion based on in-depth analysis of surface deformation. However, most geodetic methods usually have limitations in dynamic displacement measurements. GPS-based methods are restricted by the possible mismodeling of various intervening effects (such as ionospheric and tropospheric delay, multipath, and residual clock errors) [7]. Besides, the deviation caused by the influence of atmospheric, satellite orbit, and temporal decorrelation sensitivity will lead to the image interpretation error in the INSAR technology [8, 9]. All these

limitations will increase the uncertainty and cost in the real ground motion measurements. In this paper, we use a computer vision-based observation technology which is an innovate approach through the previous observation techniques in recent years.

Computer vision measurement is an innovative technology [10]. Along with the unparalleled technological progress in digital image and computer intelligence technologies, vision-based technology is widely applied in various fields, such as artificial intelligence [11], structure detection [12], automatic assembly [13], and medical equipment [14]. In recent years, as a high-precision, noncontact, multipoint, and real-time measurement technology, vision technologies have significant potentials in civil engineering applications. Besides providing dynamic displacement information [15], vision-based technologies showed extensive implementation of damage detection [16] and structural health monitoring [17]. Vision-based technology also has great advantages on the measurements of ground motions compared with point-based methods. For measurement of a complex scene, structure from motion is an extensively researched topic, and 3D reconstruction is also widely used for remodelling of structures [18–20].

Moreover, the development of the city has made the number of urban monitoring equipment be in large scale. On this basis, this paper presents a new approach for measuring the absolute ground displacement using techniques of computer vision and numerical simulation, which is simple in design and has high accuracy. Besides presenting methods for each component in principle, a series of shaking table tests, such as target motion tracking and dynamic displacement monitoring, have been carried out to verify the reliability and accuracy of the proposed vision-based technology. The significance of this study is mainly reflected in two aspects. Firstly, it presents a new thought for the surface motion measurement. Secondly, it provides an effective basis to understand the ground deformation mechanism.

2. Ground Deformation Testing Method

2.1. Basic Principle of the Method. The basic principle of the ground deformation testing method is shown in Figure 1. From the figure, the camera (installed on the top of the rod) is used to obtain the relative displacement Δu , which equals to the camera deformation minus the ground deformation. Meanwhile, numerical simulation is performed to obtain the relative displacement $\Delta u'$. If the correlation coefficient between Δu and $\Delta u'$ is greater than a threshold value ε (in this paper, $\varepsilon = 95\%$), we can get the approximate absolute ground deformation value by numerical simulation. Also, the iteration time is short due to the simplicity of single degree-of-freedom system (SDOF) to simulate the testing system. Based on the basic principle of structural dynamics, the visual testing equipment is simplified as a single degree-of-freedom system with centralized mass m supported by a mass-free structure with lateral stiffness k , which retains the original structural dynamic characteristics [21].

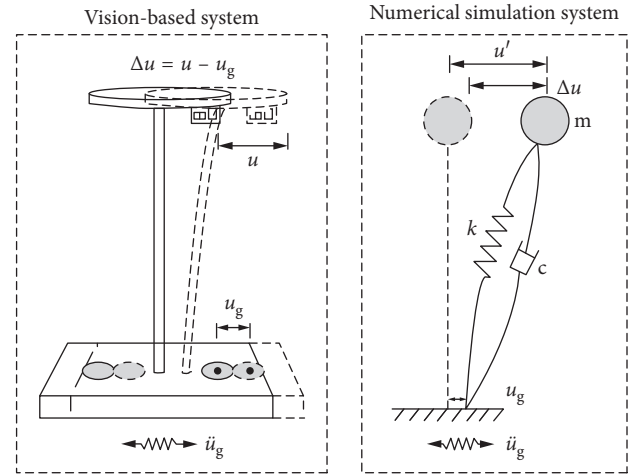


FIGURE 1: The basic principle of the method. (a) Vision-based system. (b) Numerical simulation system.

2.2. Test Instrumentation and Layout of Sensors. The camcorder used in this test, which has 1920×1080 pixels of resolution and is able to measure by 60 frames per second, the optical equipment (such as lenses, and cameras) and target size play important roles in the vision-based measurement system. Many sensors were deployed to record various parameters throughout the series of shaking table tests, such as acceleration and displacement. The layout of sensors in the test are shown in Figure 2, which includes 7 cameras, 2 accelerometers, and 1 gyroscope, denoted as Dc, A, and G, respectively.

2.3. Input Motions and Loading Conditions. The purpose of shaking table tests is to obtain the accuracy of the method on the ground deformation measurements. Therefore, the input motions should cover a wide range of frequency spectrum. Using the flat noise, 1 Hz, 3 Hz and El Centro and Taft ground motions as reference waves, the Taft ground motion was recorded at the Taft seismologic recording station during the Ms7.7 Kern County earthquake on 21 July 1952 in California, USA, with an original peak acceleration, fault distance, and duration of 0.152 g, 41 km, and 54 s, respectively. The acceleration time histories and Fourier spectra of the input motions are shown in Table 1. The flat noise inputs are used to obtain the inherent characteristic of the system, and 1 Hz (PGA = 0.1 g) and 3 Hz (PGA = 0.5 g) are used to verify the accuracy and precision of the vision-based ground deformation testing method.

2.4. Vision-Based Testing Method and Processing Method. The video was captured by the camera. The center coordinates and the radius of a target circle can be obtained by the circle fitting algorithm. The center coordinates of the target are derived from the sampled static image sequence. Therefore, the horizontal and vertical displacements of the target circle center in the image are obtained, and the real displacements are obtained by calibrating the relationship between the image pixels and coordinates of the actual objects (the 10 cm circle is used herein). The flow chart of the

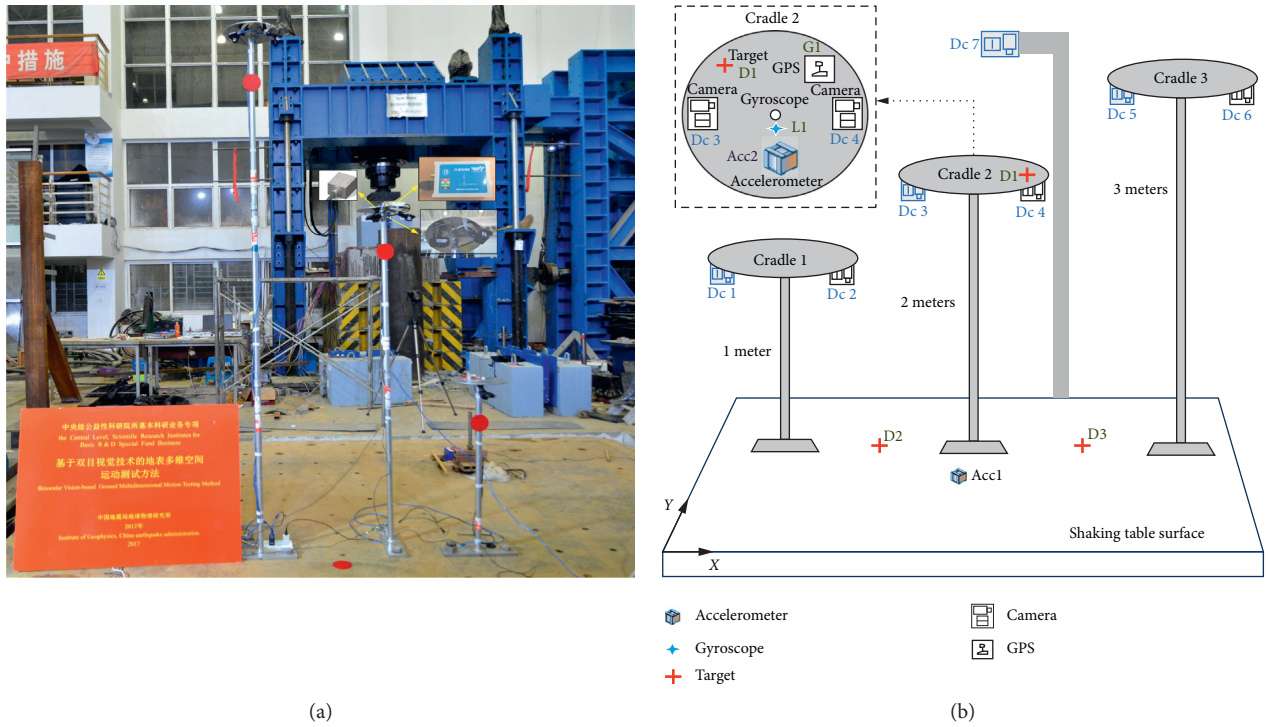
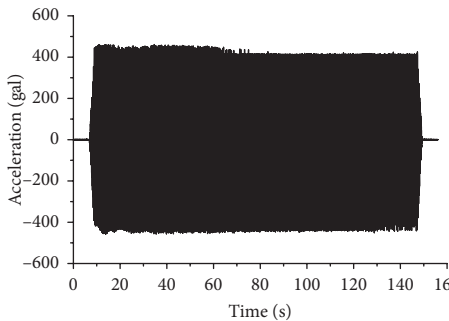
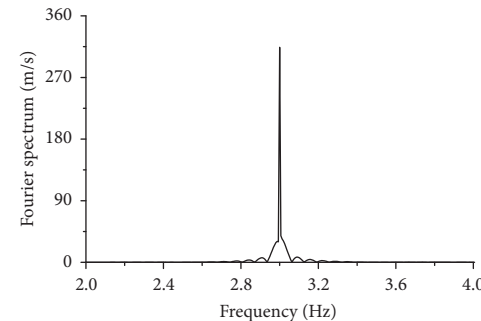
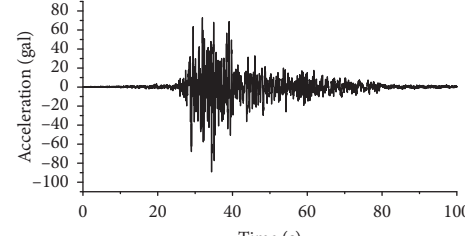
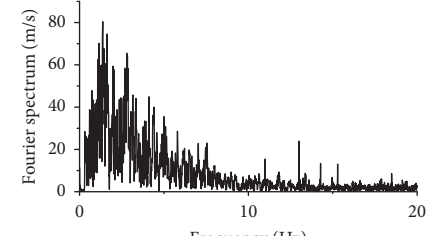


FIGURE 2: Test instrumentation and layout of sensors. (a). The layout of the instrumentation. Three instruments with different lengths are placed on the shaking table. The red circles are the targets used for vision tracking by cameras on the outside of the shaking table. In the background, it is the controller of the shaking table. (b) Sensor layout. On the top of the pole, main sensors are placed on the plate, which are cameras, accelerators, GPS sensors, and gyros.

TABLE 1: Test cases for the shaking table tests.

Test case	Ground motion acceleration time history	Fourier spectra
Flat noise		Broadband
1 Hz sine wave		

TABLE 1: Continued.

Test case	Ground motion acceleration time history	Fourier spectra
3 Hz sine wave	 <p>Acceleration (gal) vs Time (s). The plot shows a dense, noisy band of acceleration values between approximately -500 and 500 gal, centered around 0, over a time interval from 0 to 160 seconds.</p>	 <p>Fourier spectrum (m/s) vs Frequency (Hz). The plot shows a single sharp peak at approximately 3.0 Hz, with a maximum amplitude of about 360 m/s. The x-axis ranges from 2.0 to 4.0 Hz, and the y-axis ranges from 0 to 360 m/s.</p>
Taft record	 <p>Acceleration (gal) vs Time (s). The plot shows a transient seismic event with high-frequency oscillations between approximately -100 and 80 gal, occurring between 20 and 100 seconds.</p>	 <p>Fourier spectrum (m/s) vs Frequency (Hz). The plot shows a broad spectrum of frequencies from 0 to 20 Hz, with a maximum amplitude of about 80 m/s. The x-axis ranges from 0 to 20 Hz, and the y-axis ranges from 0 to 80 m/s.</p>

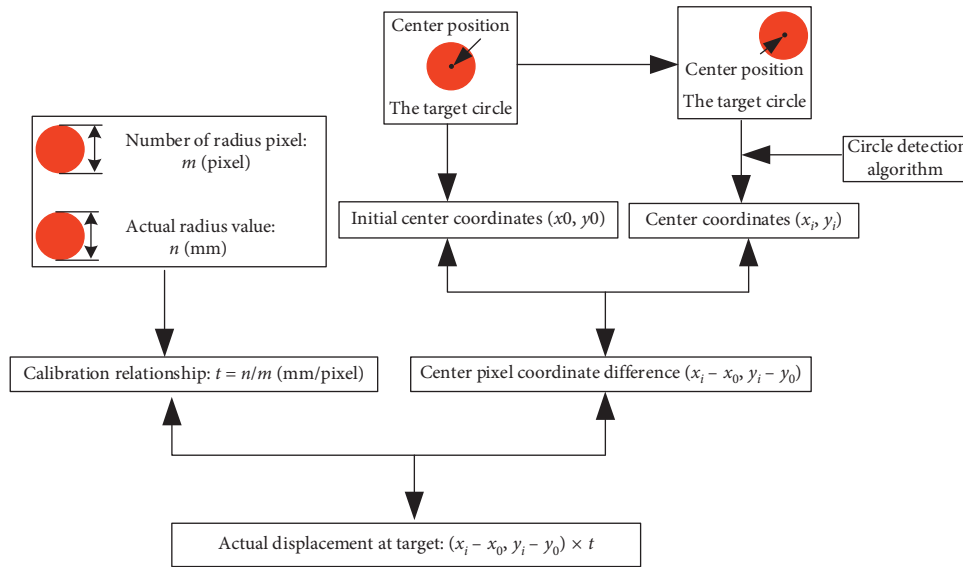


FIGURE 3: Schematic diagram of the algorithm flow.

vision-based deformation test method is shown in Figure 3. Two key points of the method are the circle detection algorithm and calibration relationship. In this paper, the basic principle of circle detection based on the least squares method (LSM) is adopted, which uses the target circle's edge point coordinates just doing one operation, and the target circle parameters (center coordinates and radius) are obtained. The algorithm flow is shown in Figure 4, in which $edge$ is the edge of the target circle in the image and (X_i, Y_i) is the edge point coordinates of the target circle. The asymptotic time complexity of the algorithm is $O(n)$, which is the computational efficient.

The precision of the vision-based dynamic displacement testing is estimated by a small-scale shaking table test. The validation system is shown in Figure 5. Four target circles (radii of all circles were 10 mm) were set for the displacement test, and strain displacement meters were laid on the side of the table board to collect displacement data. The testing input excitations were 1, 3, and 5 Hz sine waves. Based on the calibration relationship, approximately 45.2 pixels represent 1 cm of actual space [22].

Under different excitations, the displacements for the selected mark A were obtained by displacement meter and vision-based displacement test method which were

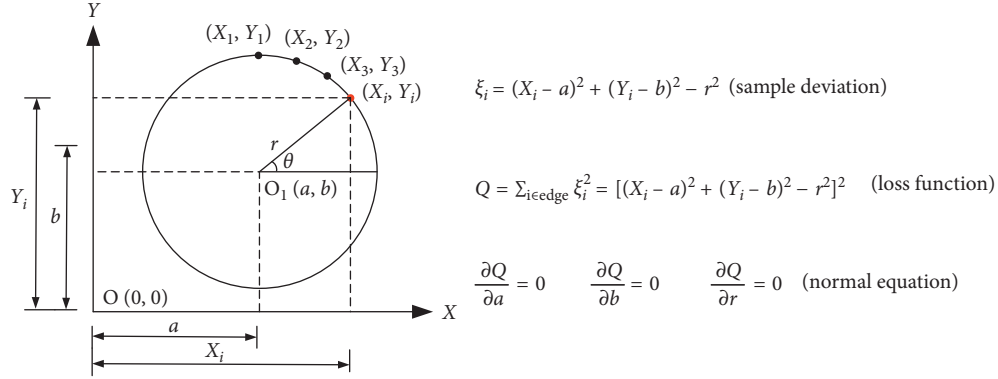


FIGURE 4: Schematic diagram of the circle detection algorithm.

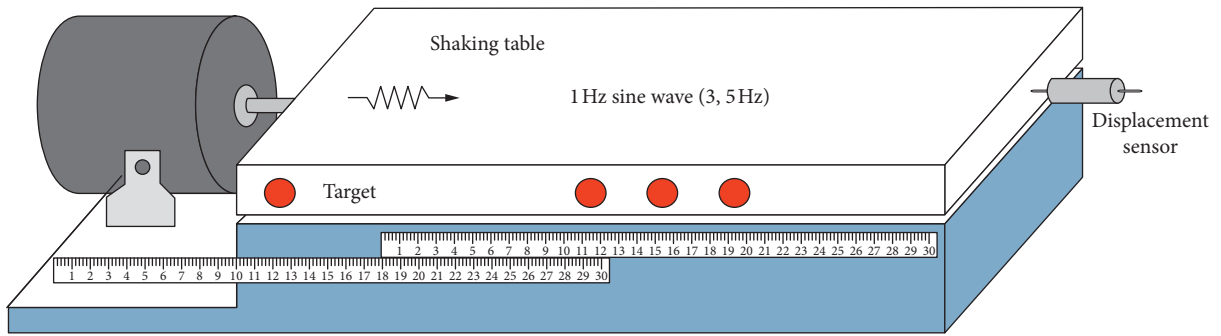


FIGURE 5: The verification test system of the vision-based displacement test method.

compared. The results are shown in Figure 6. It is clear that the displacement amplitudes and shapes are close to the curves obtained by the vision-based dynamic displacement testing method and the strain displacement meters. When input sine waves are 1, 3, and 5 Hz, the corresponding correlation coefficients of the displacement curves measured by the two testing methods are 0.994, 0.996, and 0.990, respectively.

2.5. Numerical Simulation and Verification. The whole testing system is simplified as a single degree-of-freedom model. Formula (1) is the governing equation of the vision-testing system. For the purpose of researching the feasibility and accuracy of the proposed analytical system, the same excitation loads were chosen to input into the numerical model. The analytical expression of the relative displacement of the system is calculated by the Duhamel integral method and is shown in formula (2), and the absolute ground displacement is obtained by formula (3):

$$m\Delta\ddot{u}'(t) + c\Delta\dot{u}'(t) + k\Delta u'(t) = -m\ddot{u}'_g(t), \quad (1)$$

$$\Delta u'(t) = -\frac{1}{m\omega\sqrt{1-\zeta^2}} \int_0^t e^{-\omega\zeta(t-\tau)} \cdot \sin \omega\sqrt{1-\zeta^2}(t-\tau)\ddot{u}'_g(\tau) d\tau, \quad (2)$$

$$u'_g(t) = \int \int_0^t u'_g(t) dt d\tau, \quad (3)$$

where m , k , ω , ζ , and c are the quality, stiffness, frequency, damping coefficient, and damping ratio, respectively; \ddot{u}'_g and u'_g express the ground motion acceleration and displacement, respectively; $\Delta u'$ is the analytical relative displacement between top of the rod and the ground surface; and t is the vibration time, and $d\tau$ means the time integral term.

The natural frequencies of the vision system are 7.96 Hz, 3.42 Hz, and 2.29 Hz, and the damping ratios of 1-meter pole, 2-meter pole, and 3-meter pole are 1.82%, 4.20%, and 6.32%, respectively. The relative displacement between experimental data and analytical solution (2-meter pole) is shown in Figure 7. The vision-based testing displacement result is close to the numerical simulation result in the frequency domain for both small and large PGAs, as shown in Table 2. However, in the time domain, the vision-based testing results are greater than the numerical results, the amplification factor are about 0.8120, 0.9244, and 0.8547 for the test cases of 1 Hz (PGA = 0.1 g), 3 Hz (PGA = 0.5 g), and Taft, respectively.

In addition to using graphics and quantitative parameters to intuitively reflect the correlation between the measured value Δu and the analytical solution $\Delta u'$, the Bland-Altman method is also used to verify the feasibility and accuracy of the numerical model. As shown in Figure 8, the mean is used as the abscissa and the difference $d = \Delta u - \Delta u'$ as the ordinate. The horizontal solid line in the middle is the mean line of difference d , which can be seen to be very

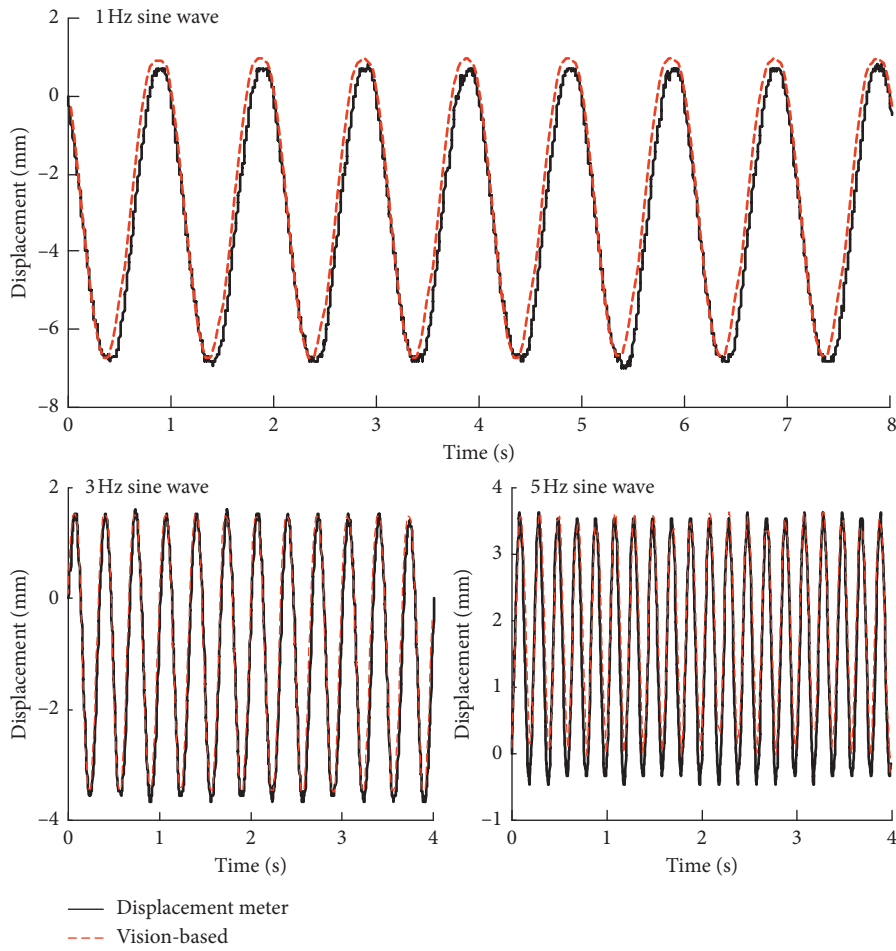


FIGURE 6: Displacement comparison charts obtained by different displacement test methods under different waves. (a) 1 Hz sine wave. (b) 3 Hz sine wave. (c) 5 Hz sine wave.

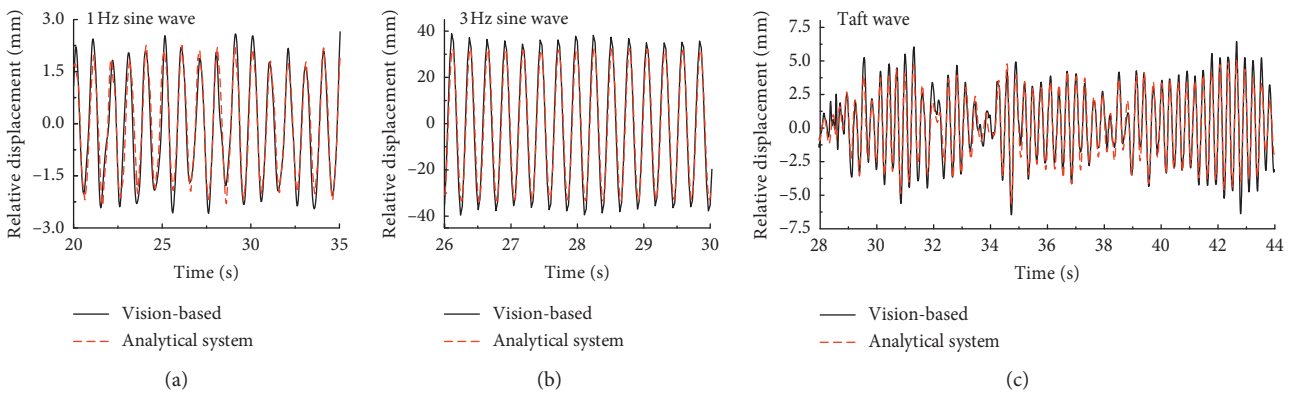


FIGURE 7: Continued.

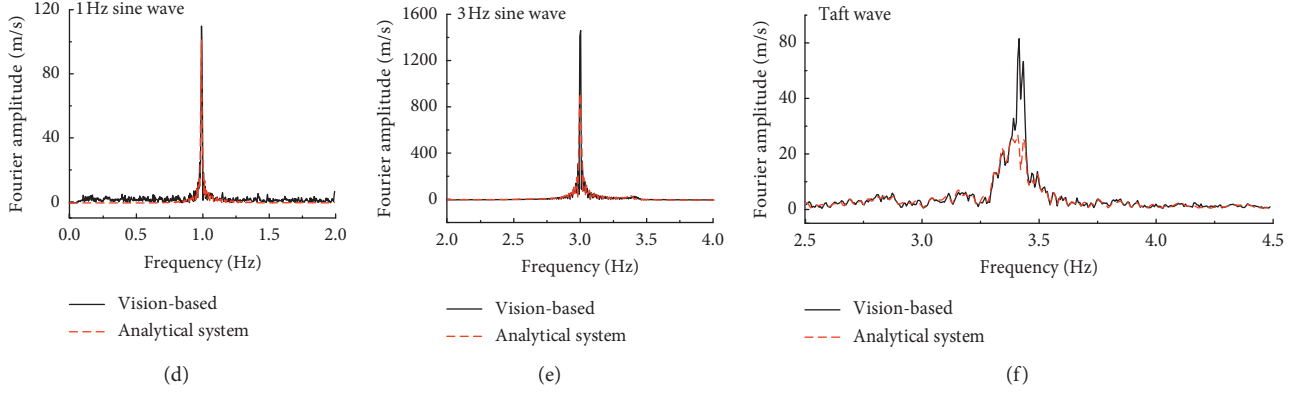


FIGURE 7: Comparison of the relative displacement of (a) 1 Hz sine wave, (b) 3 Hz sine wave, and (c) Taft wave and Fourier amplitude (d) 1 Hz sine wave, (e) 3 Hz sine wave, and (f) Taft wave between experimental data and analytical solution.

TABLE 2: Quantitative analysis of results.

Case	Time history amplitude (mm)			Fourier peak frequency (Hz)		
	Δu_A	$\Delta u'_A$	$\Delta u'_A/\Delta u_A$	f_p	f'_p	f'_p/f_p
1 Hz sine wave	2.8105	2.2821	0.8120	1.001	1.001	1.000
3 Hz sine wave	39.6298	36.6342	0.9244	3.0032	3.0029	0.999
Taft record	5.98947	5.1189	0.8547	3.418	3.412	0.998

Δu_A and $\Delta u'_A$ are the amplitude of experimental and numerical results for relative displacement time history curves, respectively. f_p and f'_p are the frequency corresponding to the peak point of Fourier spectrum curve in experimental and numerical results, respectively.

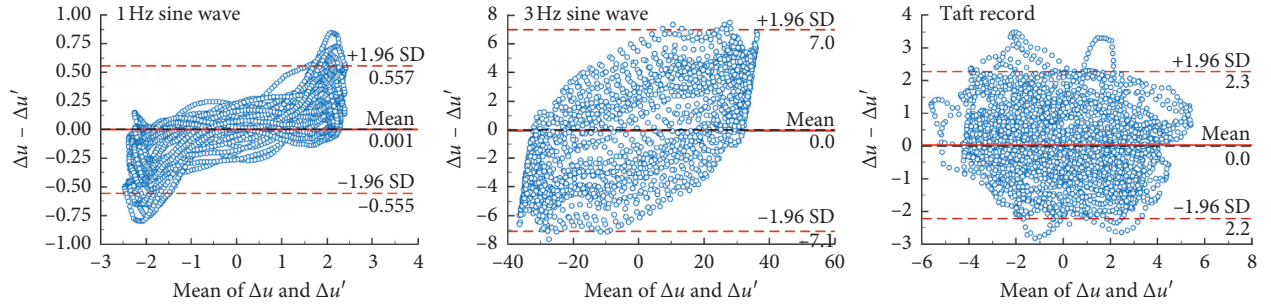


FIGURE 8: B-A diagram of relative displacement between experimental data and analytical solution. (a) 1 Hz sine wave. (b) 3 Hz sine wave. (c) Taft record.

close to the value of 0. Comparing the distribution of scatter points within the line of consistency limit ($d \pm 1.96Sd$, Sd is the standard deviation), the differences of 95.941%, 99.200%, and 96.502% are located in the confidence interval under different working conditions, respectively. It shows that the results of the two methods are very close and consistent. The numerical model represents the dynamic response of real monitoring equipment well under complex ground motions.

3. Result and Interpretation

3.1. Ground Displacement. At present, the ground displacement generally is adopted by the macroseismograph (using the numerical integration method), and Figures 9–10 shows the displacement integral from acceleration to displacement in different test cases; it is clear

that using acceleration integral to obtain the displacement requires corresponding processing of the acceleration signal, especially the filtering process, where the acceleration signal is not filtered, the displacement signal will be distorted, and under different filters, the displacement shows different characteristics. In addition, it can be seen from Figure 10 that, no matter what filter and parameter are adopted, the signal will be suppressed at some frequency domain, so that the displacement value generated by the integral is less than the value of ground truth.

In Figure 11, the ground displacement acquired by the new testing method is almost equal to the ground truth (in this test, we use Dc7, which is installed outside of the shaking table), where the relative displacement calculated by the numerical simulation is close to the measurements by the vision system. Moreover, the absolute displacements

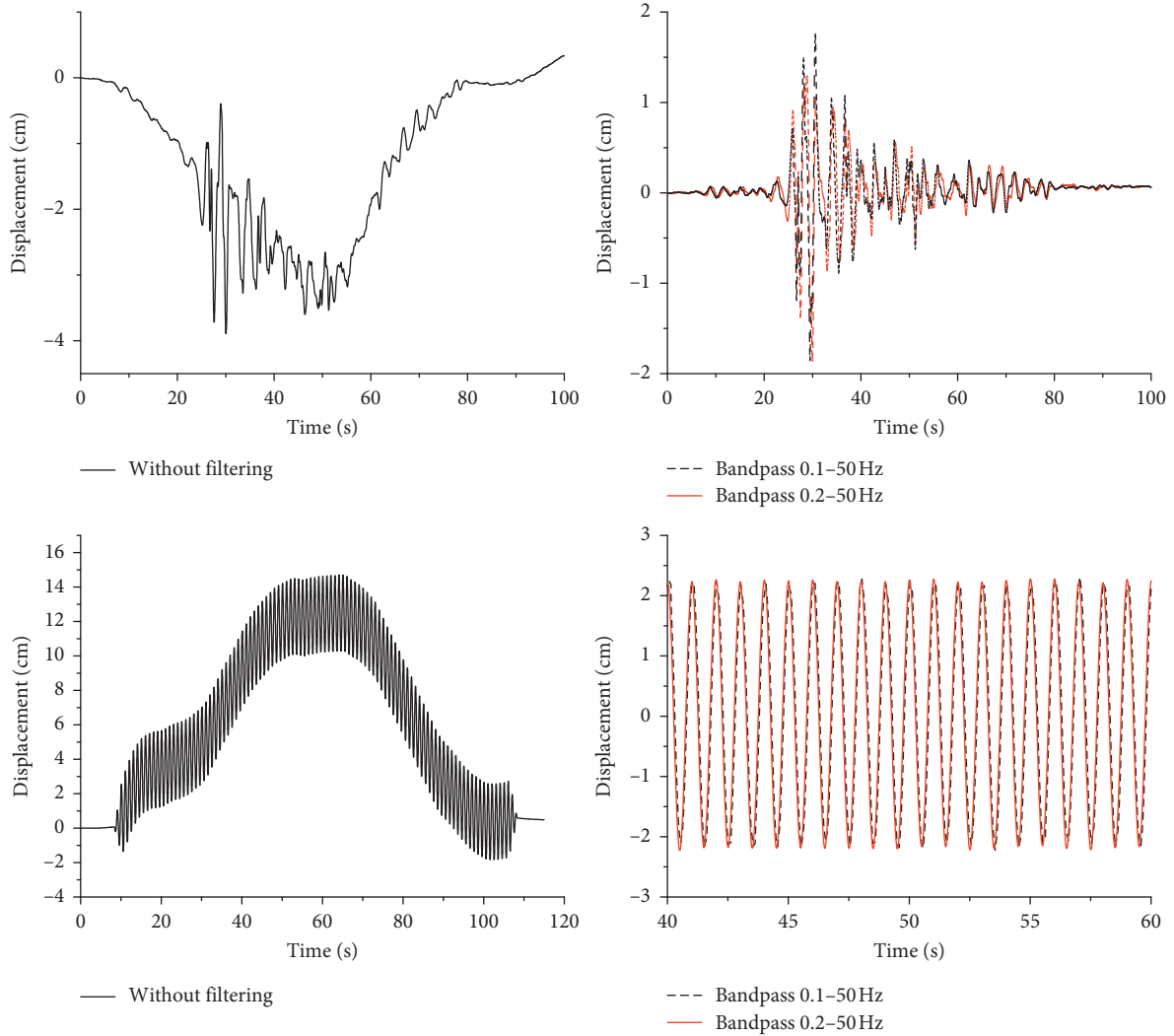


FIGURE 9: The ground displacement generally is adopted by the macroseismograph.

measured by the two methods coincide well in the frequency domain. From the BA chart of the two observation results, the scatter points are uniformly distributed in the standard deviation line, the mean line is close to zero, and the difference distribution in the confidence interval accounts for more than 95%. Hence, we can use the vision system and numerical simulation method to obtain the approximated ground displacements.

3.2. Concluding Remarks and Discussion. We have proposed and tested a simple but sophisticated new approach to estimate ground deformation. Major issues of the proposed method have been discussed in detail, such as visualized data processing and numerical methods. A series of shaking table tests were performed to investigate the feasibility and practicability of the proposed method. The new approach provides a ground displacement testing method with acceptable accuracy, in noncontact mode, being multipoint measured in real time and cost saving.

Based on our experiments and numerical simulation, the real-time ground displacement can be obtained,

validated by the vision observations. Note that the same ground motion has been used when processing the ground displacement, which corresponds to the condition when the macroseismograph is installed at the bottom of the equipment. However, the acceleration is unknown under actual conditions; in such cases, we use the nearest macroseismograph data as a seed for input motion and use the relative displacement as an intermediate quantity, by repeated iteration to obtain the approximate ground displacement. The basic idea of our approach is to estimate the ground deformations, meanwhile, and the inverse method can be used to determine the absolute ground displacement by the following formula:

$$u_g(t) = -\frac{1}{m} \cdot \left(m\Delta u(t) + c \int \Delta u(t) dt + k \iint \Delta u(t) dt d\tau \right), \quad (4)$$

where $\Delta u(t)$ means relative displacement and can be tested by the vision-based method; m , c , and k are the mass, damping, and stiffness, respectively, and can be tested or calculated by the existing mature method.

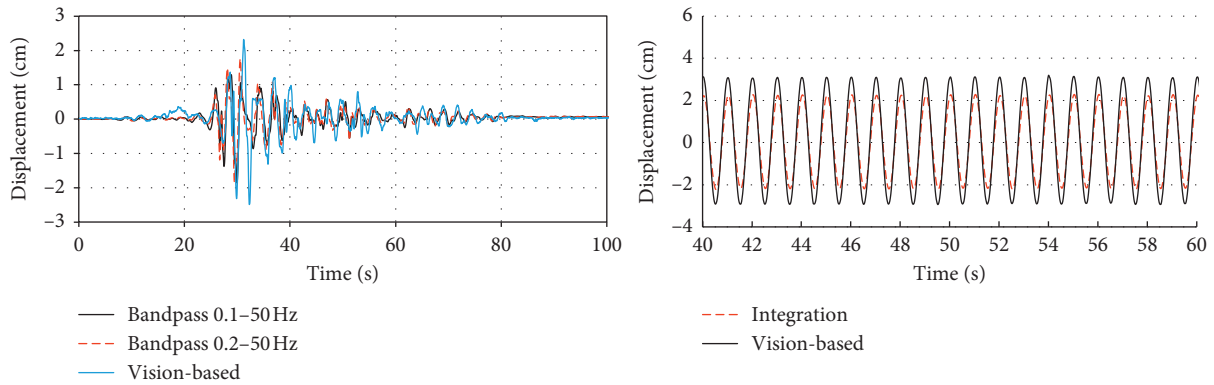


FIGURE 10: Comparison of displacement between integration and vision-based methods.

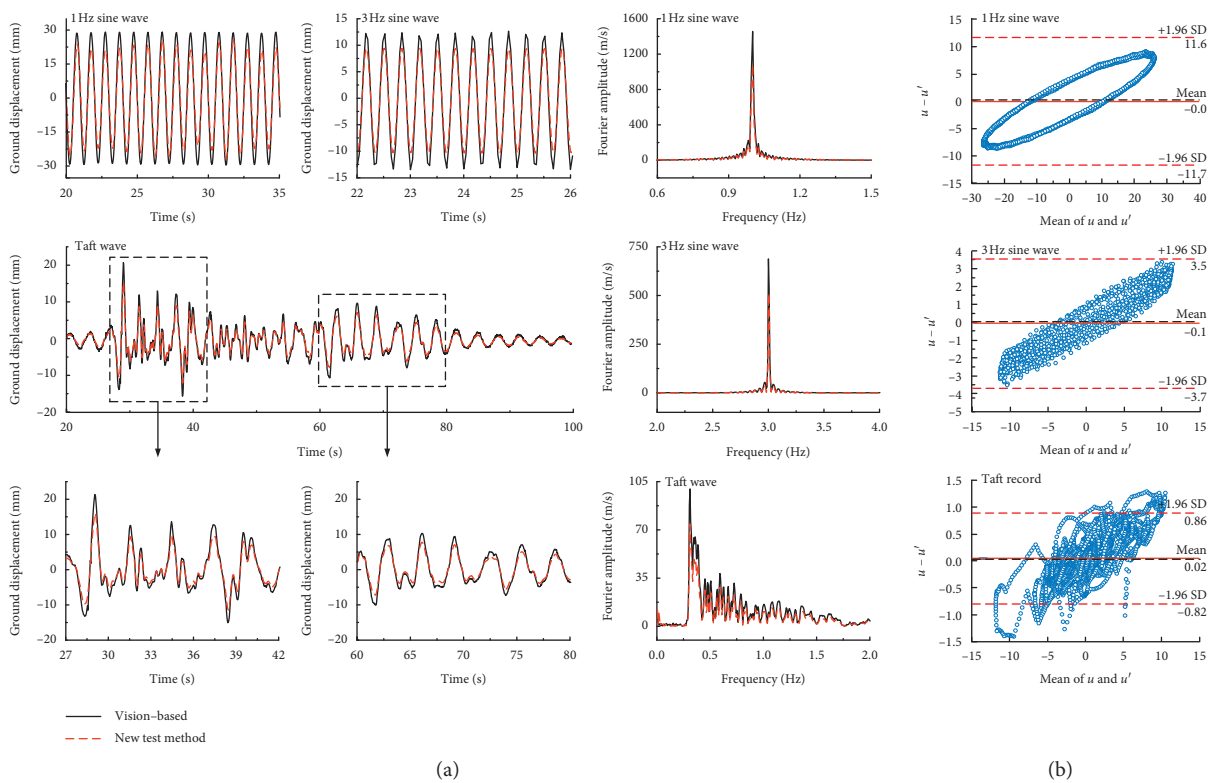


FIGURE 11: Comparison of ground displacements between experimental data and new method. (a) Comparison between time domain and frequency domain. (b) Bland-Altman diagram.

Noted that the new ground displacement method can only track the motions in flat surfaces, the method cannot be performed on all axes (X , Y , and Z axes) that use binocular vision technology to recover the depth information and establish the three-dimensional displacement spatial field after earthquake. Meanwhile, the device parameters play a very important role in the test; in addition, we adopt the high-precision optimal circle fitting method, and with the development of computer vision algorithm, the precision can be improved continuously. Moreover, the results measured by direct integration and new testing method are both smaller than the real displacement, and the amplification factor is in the range of 1.2 to 1.3. Our method has the

potential to provide large amounts of seismic data, and with the progress of optical equipment and VI (visual identity) algorithms, the accuracy of this method will be improved significantly.

Data Availability

The data used to support the findings of this study are available from the corresponding author upon request.

Conflicts of Interest

The authors declare that they have no conflicts of interest.

Acknowledgments

The authors gratefully acknowledge the financial support for this study by the Natural Science Foundation of China (Nos. 51738001 and 61472373) and by the Project of the Central Level, Scientific Research Institutes for Basic R&D Special Business (DQJB17B03).

Supplementary Materials

This supplementary material is a video about how the software works and to show the process of the employed technique. The used technique can be seen in Section 2.4 of the manuscript. Using the software, we can recognize the target and obtain the displacement. In the video, the displacement is calculated for each frame, and the time series of the displacement is obtained after the whole video processed. (*Supplementary Materials*)

References

- [1] B. H. Hager, R. W. King, and M. H. Murray, "Measurement of crustal deformation using the global positioning system," *Annual Review of Earth and Planetary Sciences*, vol. 19, no. 1, pp. 351–382, 1991.
- [2] M. Huang, "Strong motion observations and recordings from the great Wenchuan Earthquake," *Earthquake Engineering and Engineering Vibration*, vol. 7, no. 3, pp. 235–246, 2008.
- [3] K. Lambeck, "Geophysical geodesy: the slow deformations of the earth," *Clarendon*, vol. 60, no. 4, pp. 7–10, 1988.
- [4] Jin Xing, Li Shanyou, Li Zuning et al., "Prospects for the development and application of the earthquake monitoring network," *Earthquake Research in China*, vol. 21, no. 2, pp. 121–129, 2007.
- [5] C. Grecea, *Geodetic Engineering- Important Tool for Romanian Seismicity Study*, 2009.
- [6] R. Michel, J.-P. Avouac, and J. Taboury, "Measuring near field coseismic displacements from SAR images: application to the Landers Earthquake," *Geophysical Research Letters*, vol. 26, no. 19, pp. 3017–3020, 1999.
- [7] G. Colosimo, M. Crespi, and A. Mazzoni, "Real-time GPS seismology with a stand-alone receiver: a preliminary feasibility demonstration," *Journal of Geophysical Research Solid Earth*, vol. 116, no. B11, pp. 1–14, 2011.
- [8] C. Colesanti, A. Ferretti, F. Novali, C. Prati, and F. Rocca, "SAR monitoring of progressive and seasonal ground deformation using the permanent scatterers technique," *IEEE Transactions on Geoscience and Remote Sensing*, vol. 41, no. 7, pp. 1685–1701, 2003.
- [9] R. Bürgmann, P. A. Rosen, and E. J. Fielding, "Synthetic aperture radar interferometry to measure earth's surface topography and its deformation," *Annual Review of Earth and Planetary Sciences*, vol. 28, no. 1, pp. 169–209, 2003.
- [10] M. Sonka, *Image Processing, Analysis, and Machine Vision*, pp. 685–686, Thomson-Engineering, Mobile, AL, USA, 2007.
- [11] L. Pérez, Í Rodríguez, N. Rodríguez et al., "Robot guidance using machine vision techniques in industrial environments: a comparative review," *Sensors*, vol. 16, no. 3, pp. 1–26, 2016.
- [12] H. Jeon, Y. Bang, and H. Myung, "A paired visual servoing system for 6-DOF displacement measurement of structures," *Smart Materials and Structures*, vol. 20, no. 4, pp. 045019–45034, 2011.
- [13] F. Lahajnar, R. Bernard, F. Pernuš, and S. Kovačič, "Machine vision system for inspecting electric plates," *Computers in Industry*, vol. 47, no. 1, pp. 113–122, 2002.
- [14] F. Juneho, K. Bouazza-Marouf, D. Kerr et al., "X-ray-based machine vision system for distal locking of intramedullary nails," *Proceedings of the Institution of Mechanical Engineers Part H Journal of Engineering in Medicine*, vol. 221, no. 4, pp. 365–375, 2007.
- [15] D. Feng, M. Feng, E. Ozer, and Y. Fukuda, "A vision-based sensor for noncontact structural displacement measurement," *Sensors*, vol. 15, no. 7, pp. 16557–16575, 2015.
- [16] C. Bernstone and A. Heyden, "Image analysis for monitoring of crack growth in hydropower concrete structures," *Measurement*, vol. 42, no. 6, pp. 878–893, 2009.
- [17] M. Malesa, D. Szczepanek, M. Kujawińska, A. Świercz, and P. Kołakowski, *Monitoring of Civil Engineering Structures using Digital Image Correlation Technique*, EDP Sciences, Les Ulis, France, 2010.
- [18] Z. Dai, F. Zhang, and H. Wang, "Robust Maximum Likelihood estimation by sparse bundle adjustment using the L1 norm," in *Proceedings of 2012 IEEE Conference on Computer Vision and Pattern Recognition*, pp. 1672–1679, Providence, RI, USA, June 2012.
- [19] Z. Dai, Y. Wu, F. Zhang, and H. Wang, "A novel fast method for l_1 infinity problems in multiview geometry," in *Proceedings of European Conference on Computer Vision*, pp. 116–129, October 2012.
- [20] A. J. Davison, I. D. Reid, N. D. Molton, and O. Stasse, "MonoSLAM: real-time single camera SLAM," *IEEE Transactions on Pattern Analysis and Machine Intelligence*, vol. 29, no. 6, pp. 1052–1067, 2007.
- [21] A. K. Chopra and F. Naeim, "Dynamics of structures—theory and applications to earthquake engineering, third edition," *Earthquake Spectra*, vol. 17, no. 3, pp. 549–550, 2001.
- [22] G. Chen, S. Chen, C. Qi et al., "Shaking table tests on a three-arch type subway station structure in a liquefiable soil," *Bulletin of Earthquake Engineering*, vol. 13, no. 6, pp. 1675–1701, 2014.